POLITECNICO DI MILANO

Master Degree in Nuclear Engineering

STICKING COEFFICIENTS FOR TECHNICAL MATERIALS IN VACUUM TECHNOLOGY

Relatore: Prof. Marco Beghi

Correlatore(i): Jose Antonio Ferreira Somoza

Mattia Ortino Matr. 820219

Submitted in partial fulfilment of the requirements
For the degree of Master of Science in Nuclear Engineering,
Politecnico di Milano, 2016

Geneva, Switzerland

Ai miei genitori,

Il faut risquer

H.Wieniawski

Acknowledgement

I would like to thank my supervisor J.A.Ferreira Somoza and my section leader at CERN Giuseppe Bregliozzi, who taught me a lot during my 14-months technical student program at CERN, in Geneva. The incredible passion and depth they put into their scientific work has been inspirational and fundamental.

Then, under the professional (and even the motivational) point of view, a special thanksgiving is for Chiara Pasquino, Roberto Kersevan and Yorick Delaup: their patience and assistance with the experimental set-up and the simulative work was impressive; Bernard Henrist for his useful electronic knowledge, Nicholas Zelko for the technical discussions in the lab 113 and Valentin Nistor for providing surface analysis measurements.

Finally, I would like to thank Marco Beghi, for having shown me the opportunity of this internship and to guided me during this path.

Abstract

This master thesis has been developed at CERN, European Centre for Nuclear Research, aiming to better measure the sticking factor of different molecules on the walls of the materials used in vacuum technology. First of all, the interaction between water molecules and stainless steel vacuum chambers has been studied. Water desorption is considered the main obstacle for a fast achievement of UHV (Ultra High Vacuum) pressures in unbaked systems. Using a new experimental set-up the quantities involved in the calculation of the sticking probability have been known and controlled: the quantity of gas injected, the temperature and the quantity of gas adsorbed with high time resolution to evaluate the dynamic phenomena of water absorption.

Furthermore, the procedure to calculate the sticking factor has been studied of different molecules (H_2, N_2 and CO) in vacuum chambers internally coated with a Non-Evaporable Getter (NEG) thin film.

These chambers are tested in the lab, before their installation. The aim of the work has been to upgrade the testing procedure avoiding the saturation of the vacuum chamber at the same time is being measured, particularly when measuring gases with high sticking factor like CO. Finally, a new acceptance test set-up has been evaluated by means of fast injections of gas, which should preserve from saturation and allows to measure the sticking factor at higher pressures.

Sommario

Il seguente lavoro di laurea è stato sviluppato al CERN, Centro Europeo per la Ricerca Nucleare, con l'obiettivo di comprendere al meglio alcuni aspetti del fenomeno di sticking tra molecole e pareti delle camere utilizzate nella tecnologia del vuoto. Per prima cosa, é stata studiata l'interazione tra molecole d'acqua e pareti metalliche delle camere. Proprio il desorbimento d'acqua, é considerato il maggior problema al raggiungimento delle condizoni di Ultra Alto Vuoto (UHV) nei sistema unbaked. Usando un nuovo set-up sperimentale, é stato possibile conoscere e controllare attivamente le quantitá in gioco nella valutazione della probabilitá di sticking, come la quantitá di gas iniettato, la temperatura e la quantitá di gas adsorbito. Inoltre, é stato testato un nuovo coating in ossido di cromo, cercando di valutare i possibili guadagni in termini di tempo di pump-down rispetto all'acciaio inossidabile.

La seconda parte del lavoro si é svolta invece sullo studio della procedura di test di particolari camere a vuoto, internamente rivestite con un thin-film "Non-Evaporable Getter"(NEG).

Queste camere, prima della loro installazione, vengono testate in laboratorio. Lo scopo di questo lavoro é stato quello di migliorare la procedura di test, tenendo in considerazione un fenomeno come la saturazione dei siti di adsorbimento della superficie NEG. Infine, é stato proposto un nuovo set-up per test di accettazione delle camere che, utilizzando iniezioni di gas veloci, consente di evitarne la saturazione e allo stesso tempo di riprodurre piu realisticamente le quantitá di gas presenti in acceleratore.

CHAPTER 1
INTRODUCTION TO CERN

This thesis is the outcome of research work carried out during one year spent at the European Organization for Nuclear Research (CERN) In Geneva, Switzerland.

This centre, founded on 29 September 1954 by 12 countries of the Western Europe, aimed to obtain the leadership in physics for Europe, since in those years the principal research centres were in the USA. Nowadays CERN is the largest particle physics laboratory in the world, including 21 member countries and collaborations with research groups from all over the world.

Figure 1: Third session of the provisional CERN council in Amsterdam on the 4th October 1952. At this session, Geneva was chosen as the site for the future laboratory (courtesy CERN).

The first CERN's accelerator, built in 1957, was the *600 MeV* Synchrocyclotron (SC), providing beams for the first particle and nuclear physics experiments. Today with LHC, the longest accelerator ever built with his 27 km of length (and with the perspective of

FCC, a future 100 km long one), a high level study of the constituents of matter is provided by means of the acceleration of the particles close to the speed of light and their consequent collision revealed by detectors. In this sense, the actual structure of the CERN accelerator complex is showed in Figure 2.

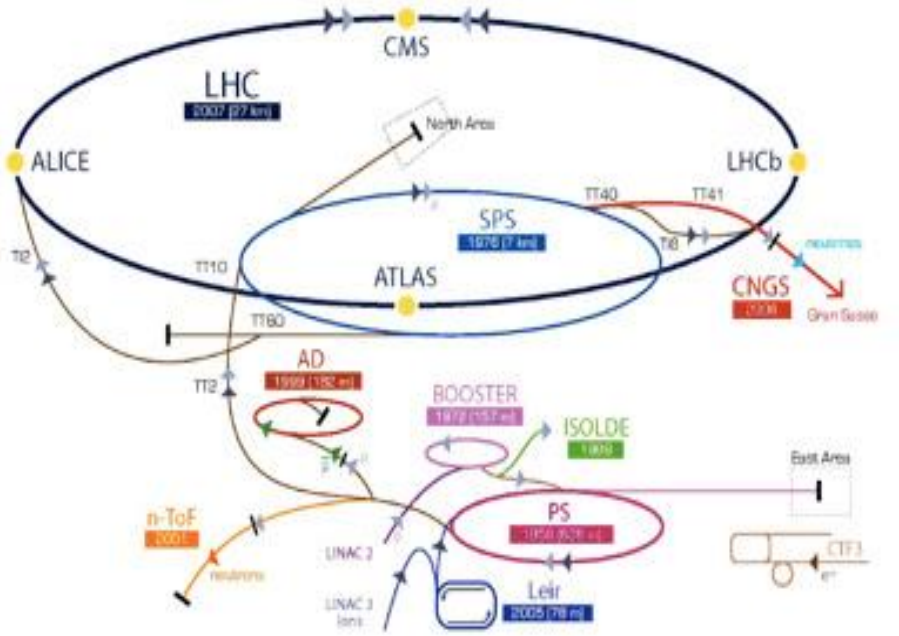

Figure 2: Scheme of CERN accelerators complex. (courtesy CERN)

Different steps of acceleration are provided depending on the type of accelerated particle (protons or heavy ions like lead or argon) and the destination (different experimental areas or interaction points of LHC). Protons are created in a linear accelerator, LINAC 2. They pass through BOOSTER, PS and SPS rings, where their velocity approaches more and more to the speed of light. Finally, two beams are injected into LHC, the Large Hadron Collider, and reach their maximum energy before colliding in the interaction points where the detectors are installed. The design energy of LHC is 7 TeV (per particle), with a luminosity (the ratio between the number of events per second N_{event} generated in the LHC collisions and the cross-section σ_{event} for the nuclear event under study) of $10^{34}\ cm^{-2}\ s^{-1}$.

1.1 Vacuum at CERN

At CERN different vacuum levels are found depending on the requirements of different installations, from low vacuum in some experimental areas to extreme high vacuum (XHV) in LEIR or in ELENA rings.

One of the most interesting vacuum challenge at CERN are the Long Straight Section (LSS) of LHC (Large Hadron Collider). As shown in Figure 3, there are eight LSS in LHC, dividing the ring into eight sectors with experimental and utility purposes.

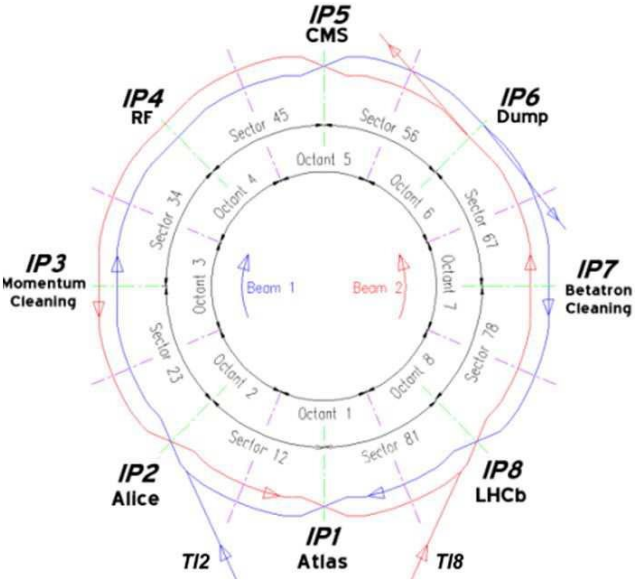

Figure 3: Schematic view of the LHC, showing the location of the eight Long Straight Sections

The most critical areas are the interaction points where the two beams collide. The pressure must be lower than $10^{-10} mbar$ and the detectors occupy most of the space available.

Almost all these chambers are internally $Ti - Zr - V$ coated, a Non Evaporable Getter alloy (NEG) which absorbs molecules after thermal activation (*bake-out*). These coatings were developed at CERN between 1995 and 2002. The use of NEG coatings transform the vacuum chamber from a gas source (outgassing) to a gas sink (pumping) with the collateral benefit of e-cloud mitigation because of its low secondary electron yield (SEY).

Linearly distributed ion pumps[1] and NEG strips[2] were used in the past for such applications.

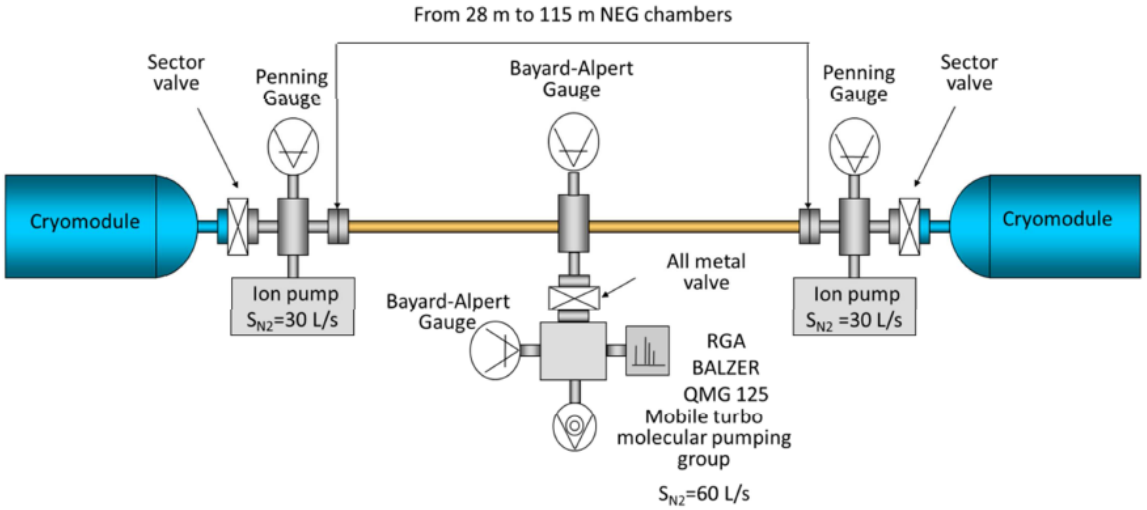

Figure 4: Schematic view of one typical sector of the LHC's Long Straight Sections

In every accelerator at CERN external pumping groups pumpdown from atmospheric until $10^{-5}\ mbar$; then the accelerator is ready to switch on its ion pumps or start a bakeout cycle depending on the required vacuum level. The entire process of pressure decrease (called pump-down) takes between 12 and 48 hours, depending on the outgassing of the components installed and available pumps on the vacuum sector.

The long pump-down is required because the time needed to remove the water absorbed on the surface. These molecules are adsorbed on the walls of vacuum chambers every time they are exposed to the atmosphere.

1.1.1 Costs linked to water desorption for CERN accelerator complex

The time required for pump-down to reach UHV has following costs:

- Non-exploitation costs. In 2012, the interventions took nearly 500 hours in total. In average, half of this time is lost in obtaining again low pressures in the line. The whole LHC accelerator complex, a 1.5 billion € machine is blocked 250 hours each year because of pump-down or bake-out.
- Intervention costs: costs linked to the equipment and manpower needed to reduce water outgassing. For example, nearly 20 sectors per year need to be baked for technical stops, representing a cost of 300'000 €/year.
- Design costs. In order to be able to undergo bake-outs, LHC vacuum chambers require a dedicated design. For example, the copper used for the 6 km room temperature beam lines, is doped with silver in order to obtain higher thermal conductivity, resulting 40% more expensive than usual OFHC (Oxygen free high thermal conductivity) copper[3].

Considering what is exposed above, it is clear how the absorption of water influences both LHC and the injectors availability.
For this reason, the understanding of the water absorption phenomena is important prior to test methods to minimize its effects.

CHAPTER 2
VACUUM TECHNOLOGY PRINCIPLES

Vacuum technology is widely used, not only on particle accelerator technology, but also on aerospace, food processing, fusion and medical sciences. At CERN accelerator complex the role of vacuum is to avoid interactions of the beam with the residual gas. This could lead to critical emittance changes on the beam, with particle losses from the beam and local thermal loads.

In vacuum systems, it is used to speak about vacuum in respect of lower pressure levels than that of the surrounding atmosphere. It is possible to define different vacuum ranges as shown in Table 2.1.

Definition	Pressure Boundaries [mbar]
Low Vacuum LV	$10^{3} - 1$
Medium Vacuum MV	$1 - 10^{-3}$
High Vacuum HV	$10^{-3} - 10^{-9}$
Ultra High Vacuum UHV	$10^{-9} - 10^{-12}$
Extreme Vacuum XHV	$< 10^{-12}$

Table 2.1 Degrees of vacuum and their pressure boundaries from Lafferty[4].

2.1 Basic notions

2.1.1 Ideal Gas Law

A rarefied gas which obeys to the *ideal gas state equation* can be defined as *ideal*.

$$pV = Nk_bT \qquad \text{Eq. 1}$$

or

$$p = nk_bT \qquad \text{Eq. 2}$$

where p, V and T are the gas pressure, volume and temperature, respectively; k_b is the Boltzmann constant ($1.3806 \cdot 10^{-23} JK^{-1}$); N is the total number of molecules in the gas and n is the gas particle density [m^{-3}]. Pressure-volume quantities – called as *Quantity of Gas* – are often expressed in terms of *number of molecules* dividing them by k_BT as given in the equation of state.

According to the International System of Units pressure is measure in Pascal (Pa), but very often is substituted by mbar, which is =100 Pa. Torricelli (=133,32 Pa) is also widely used, mostly in the USA.

	Pressure [Pa]	293 K [molecules cm^{-3}]	4 K [molecules cm^{-3}]
Atmospheric pressure at sea level	$1.013\ 10^5$	$2.5\ 10^{19}$	$1.7\ 10^{21}$
Typical plasma chambers	1	$2.5\ 10^{14}$	$1.7\ 10^{16}$
Linac 2 Cern pressure upper limit	10^{-5}	$2.5\ 10^{9}$	$1.7\ 10^{11}$
Lowest pressure ever measured at room temperature	10^{-12}	250	$1.7\ 10^{4}$

Table 2.2 Typical number density at room temperature and helium boiling point [5]

2.1.2 Gas Kinetics

Kinetic theory (1860) introduced a model which better described properties of a gas as temperature, pressure and volume due to the impact of the particles to the

surrounding walls. The Maxwell-Boltzmann model provides so a probabilistic distribution of the molecular speed magnitudes.

$$<v> = \sqrt{\frac{8k_bT}{\pi m}} = \sqrt{\frac{8RT}{\pi M}} \qquad \text{Eq. 3}$$

Where m is the mass of the molecule, M is the molar mass, R is the ideal gas constant and k_b the Boltzmann constant. Some typical values of <v> are shown[4] in Table 2.3

	H_2	CH_4	N_2	Ar
<v> at 293 K $[\frac{m}{s}]$	1761	622	470	394
<v> at 4.3 K $[\frac{m}{s}]$	213	75	57	48

Table 2.3 Mean speed at different T according to the Boltzmann distribution[5]

From Maxwell-Boltzmann theory is therefore possible to obtain the *molecular impingement rate* ϕ at which molecules collide with a unit surface area.
Assuming a uniform molecules density *n* all over the volume, it can be shown that:

$$\phi = \frac{1}{4} n<v> \quad \left[\frac{molecules}{unit\ area \cdot unit\ time}\right] \qquad \text{Eq. 4}$$

In vacuum technology, ϕ is usually expressed in $[\frac{mbar \cdot l}{cm^2 \cdot s}]$.
To have an idea of how different gasses impinge on surfaces, numerical values are shown in Table 2.4.

Gas	Pressure [mbar]	ϕ $[\frac{molecules}{unit\ area \cdot unit\ time}]$
N_2	10^{-3}	2.9×10^{17}
	10^{-8}	2.9×10^{12}
H_2	10^{-3}	1.1×10^{18}
	10^{-8}	1.1×10^{13}
	10^{-14}	1.1×10^{7}
H_2O	10^{-3}	3.6×10^{17}
	10^{-8}	3.6×10^{12}

Table 2.4 .: Impingement rate for common gases at room temperature at some selected pressures

Maxwell-Boltzmann bases the calculation on molecule-molecule and molecule-wall collision models, so giving information on the rate of the molecular collisions. In the first case, the main parameter is the average length of the molecular path between the points of consecutive collisions (the *mean free path* $<\lambda>$), which is inversely proportional to the number density $n = \frac{\mathrm{p}}{k_b T}$ and the collision cross section[4] σ_c, as given by Eq.2.5.

$$<\lambda> = \frac{1}{\sqrt{2}\ n\ \sigma_c} \qquad \text{Eq. 5}$$

For elastic collisions between rigid spheres, Eq 2.6.

$$<\lambda> = \frac{1}{\sqrt{2}\ n\ \delta^2} = \frac{k_b T}{\sqrt{2}\,\pi\ P\ \delta^2} \qquad \text{Eq. 6}$$

When the mean free path is of the order of typical dimensions of the vacuum vessel, for example the diameter of cylindrical beam pipes, molecular collisions with the wall

of the vacuum envelope start to become preponderant. For even longer <λ>, the gas dynamics is dominated by molecule-wall collitions; intermolecular interactions lose any effect on the gas displacement.

2.1.3 Knudsen number and gas flow

What we have expressed until now is translated in terms of numerical values by the *Knudsen number* K_n. It is defined as the ratio between the mean free path and a characteristic dimension of a vacuum system (D):

$$K_n = \frac{<\lambda>}{D} \qquad \text{Eq. 7}$$

Knudsen number identify so specific gas dynamic regimes, which are reported in Table 2.5

Kn range	Regime	Description
Kn > 0.5	Free molecular flow	Gas dynamic dominated
Kn < 0.01	Continuous (viscous) flow	Gas dynamic dominated
0.5 < Kn < 0.01	Transitional flow	Transition between molecular and viscous flow

Table 2.5: Gas dynamic regimes defined by the Knudsen number[5]

In LHC as also in all the injector chain at CERN, typical pipe diameters are in the order of 10 cm. Free molecular flow for pressure below $10^{-3} mbar$ is therefore obtained almost ever.

In the molecular flow is possible to define the gas flow rate, expressed in terms of pressure-volume (or also $PV_{troughput}$):

$$Q = P\dot{V} = P\frac{dV}{dt} \qquad \text{Eq. 8}$$

This quantity, of very wide use in vacuum technology, is proportional to the pressure difference between two points of the considered system.

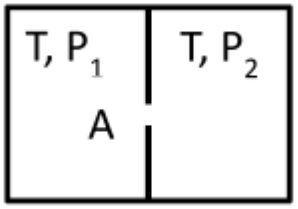

Figure 5: Schematic drawing of two volumes communicating through a thin and small wall slot.

Considering the system in Figure 5, the gas flow rate between the communicating volumes can be written as follow:

$$Q = C(P_1 - P_2) \qquad \text{Eq. 9}$$

The quantity C is called *conductance*, as we will see in the next paragraph.

2.1.4 Conductance in free molecular flow

The conductance C in free molecular regime does not depend on the pressure: it depends only on the geometry of the system and on the molecular speed inside it. Since Q is expressed in $[mbar \cdot l \cdot s^{-1}]$, the conductance take the form of a volumetric flow rate, thus $[l \cdot s^{-1}]$.

A way to define C is also using the definition of impingement rate described in eq.4. If we think indeed to the simple geometry in Figure 5 (a small orifice of surface A and infinitesimal thickness dividing two volumes of the same vacuum system in isothermal conditions), we can define the number of molecules of volume 1 which goes in to volume 2 as:

$$\phi_{1\to2} = \frac{1}{4} A n_1 \bar{v} \qquad \text{Eq. 10}$$

While from volume 2 to volume 1 is:

$$\phi_{2\to1} = \frac{1}{4} A n_2 \bar{v} \qquad \text{Eq. 11}$$

A *net* molecular flow is given by the difference of the two contributions:

$$\phi_{net} = \frac{1}{4} A \bar{v} (n_1 - n_2) \qquad \text{Eq. 12}$$

From eq. 2 ϕ_{net} is:

$$\phi_{net} = \frac{1}{4} \frac{\bar{v}}{k_B T} A (p_1 - p_2) \qquad \text{Eq. 13}$$

Now, simply multiplying the first and the last term of the quantity for $k_B T$ and expressing ϕ_{net} in terms of PV $[mbar\ l]$ we obtain:

$$Q = \frac{1}{4} \bar{v} A (p_1 - p_2) \qquad \text{Eq. 14}$$

This leads us to another definition of C, because this last with eq.**9** we obtain:

$$C = \frac{1}{4}\bar{v}A \propto \sqrt{\frac{T}{m}} \qquad \text{Eq. 15}$$

The conductance is therefore inversely proportional to the square root of the molecular mass of the species passing through. Furthermore, is possible to compare different conductance related to different gasses:

$$\frac{C_1}{C_2} = \sqrt{\frac{m_1}{m_2}} \qquad \text{Eq. 16}$$

It is everyday practice, in vacuum technology, to compare and calculate different conductance using ratios. As an example, $\boldsymbol{C_{H_2}} = \boldsymbol{C_{CO}} \cdot \sqrt{\frac{\mathbf{2}}{\mathbf{28}}} = C_{CO} \cdot 71.42 \cdot 10^{-3}$.

Table 2.6 gives some values of standard conductance related to the main gases present in typical accelerators vacuum systems.

	$\boldsymbol{H_2}$	$\boldsymbol{He}$	$\boldsymbol{CH_4}$	$\boldsymbol{H_2O}$	$\boldsymbol{N_2}$	$\boldsymbol{Ar}$
C at 293 K [$\boldsymbol{l/cm^2s}$]	44	31.1	15.5	14.7	11.75	9.85

Table 2.6: Unit surface area conductance for common gases species

Series and parallel connection of conductance

If several conductances are connected one on the other, it is possible to calculate quickly a total conductance. For a *series* of *i* conductances, the following relationship is valid:

$$\frac{1}{C_{TOT}} = \sum_i \frac{1}{C_i} \qquad \text{Eq. 17}$$

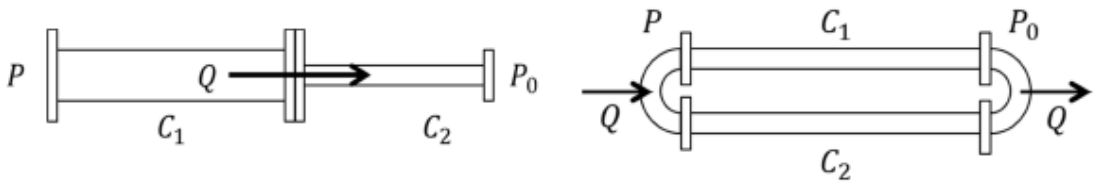

Figure 6: Series (left) and parallel (right) connection of conductances

In the same way it can be shown that for N components installed in *parallel* the total conductance is the sum of the conductance of all components:

$$C_{TOT} = \sum_i C_i \qquad \text{Eq. 18}$$

2.2 Pumping speed and pumping systems

2.2.1 Pumping speed

Another important parameter of vacuum technology is the pumping speed S, which is namely defined as the ratio between the gas flow entering the pump Q_p and the inlet pressure p:

$$S = \frac{Q_p}{P} \quad [\frac{l}{s}] \qquad \text{Eq. 19}$$

The pump throughput (Q_p) can be written as the gas flow ϕ through the cross section of the pump inlet (A_p) multiplied by the capture probability σ. This last is the probability for a molecule to be captured by the pump and to be removed from the vacuum system:

$$Q_p = \phi A_p \sigma = ¼\, A_p n \bar{v} \qquad \text{Eq. 20}$$

Considering equations 15 and 2, we obtain:

$$Q_p = C\, A_p \frac{p}{k_B T} \qquad \text{Eq. 21}$$

Converting finally the throughput in PV-units and applying the definition of pumping (eq. 19):

$$S = A_p C \sigma \qquad \text{Eq. 22}$$

This important equation, as we will see, is not only valid for S referring to *pumps* but also for *surfaces* which act as pumps, where the dimensionless value σ will take the form of a *sticking probability* on the surface itself.

It is clear as the maximum theoretical pumping speed of any pump is obtained with

$$\sigma = 1$$

and it is equal to the conductance of the pump inlet cross section.

Anyway, the values of pumping speed given by the pump suppliers become merely theoretical (S_0), because they refer only to the pump inlet. Indeed, what we have is a S_{eff}, an *effective pumping speed* which is acting directly in the vacuum vessel of interest. The effective pumping speed, which is lower than the nominal one, is calculated considering the gas flow from the vessel to the pump.

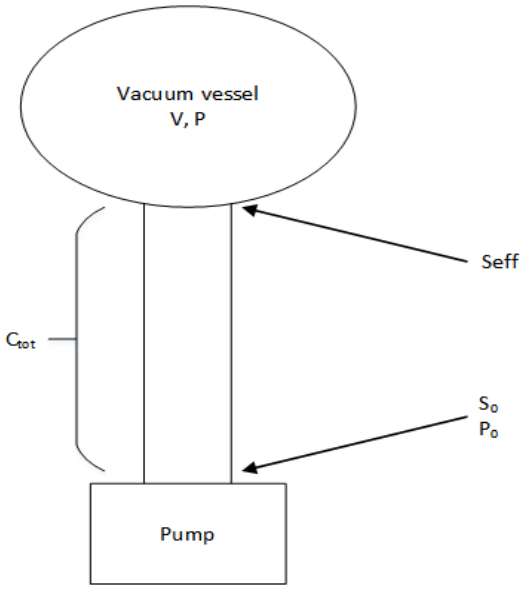

Figure 7: Difference between S_0 and S_{eff}

Taking into account Eq. 15 and 20 we have:

$$\frac{1}{S_{eff}} = \frac{1}{S_0} + \frac{1}{C_{tot}} \qquad \text{Eq. 23}$$

For very low conductance ($C \ll S_0$) $S_{eff=}\, C_{tot}$.

2.2.2 Types of pumps

Pumping speed is provided by different type of pumps, as well as by surfaces materials themselves. Depending on the physical principle performed, pumps could be classified as shown in Figure 8:

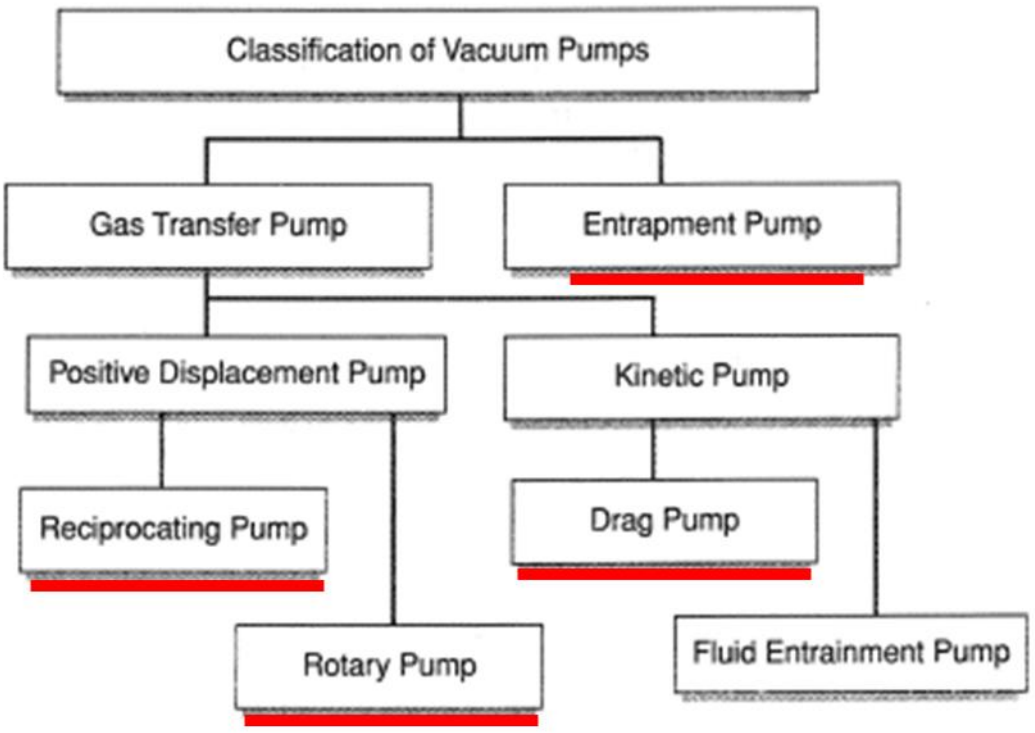

Figure 8: Classification of vacuum pumps. Underlined in red the ones which has been used in this thesis work [6]

In the family of the *rotary pumps* has been used oil sealed rotary pumps and dry pumps. These pumps provide a first step of pumping after the closure to the ambient air, reaching the maximum of $10^{-3}\ mbar$. For this reason, they are called *primary pumps.*

In the pump-down process, the lower vacuum level is achieved through *kinetic pumps.* In this family are widely used *turbo-molecular pumps.* These lasts are multi-stage pumps, in which the rotor is driven at high rotational speeds so that the peripheral speed of the blades is of the same order of magnitude of the thermal velocity $\bar{v}$ of the gas molecules to be pumped. A pumping stage is composed of a rotor, which transfers the momentum to the particles and a stator which function is to randomize the angular distribution of the velocities between a stage and the next one. The final pressure of these pumps is in the order of $10^{-9}\ mbar$. Figure 9 shows a section of a turbo-pump is shown in:

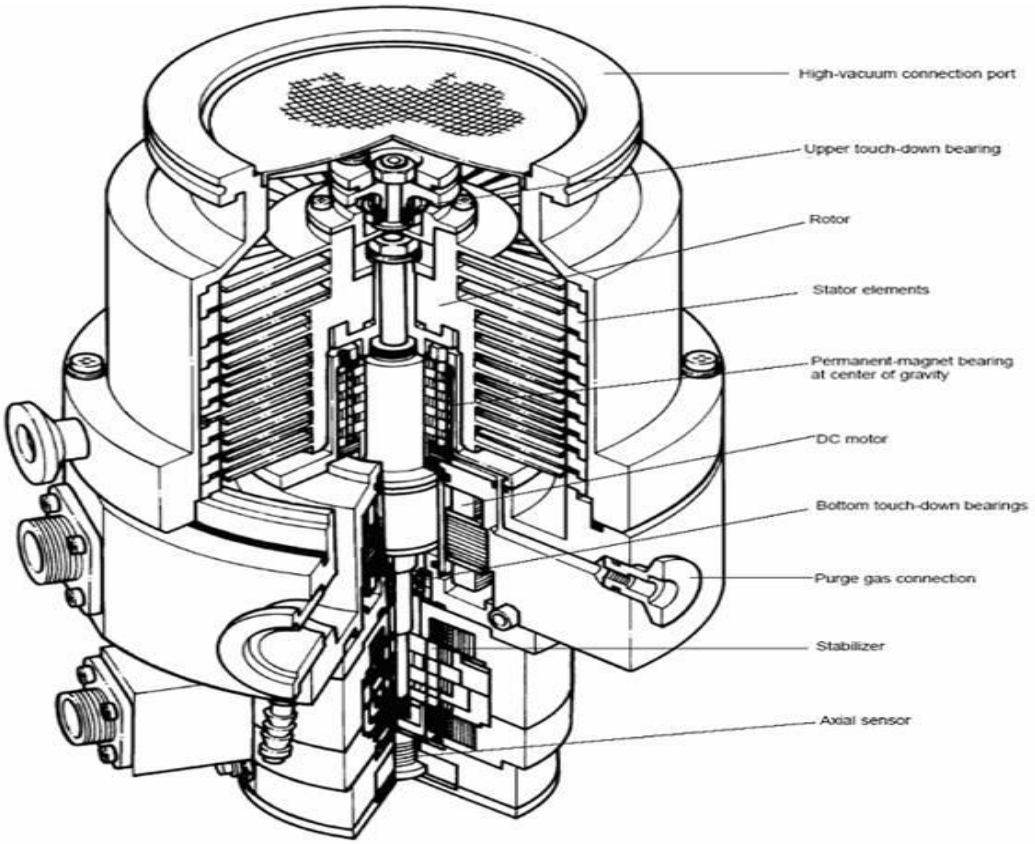

Achieving even lower pressure is then possible with another important group of pumps, which are the *entrapment pumps*. In these cases, the molecules remain inside the pump itself by bonds, without being ejected as in the other cases. In this family are widely used the *Sputter-ion pumps*, *Cryo-pumps* and *Getter pumps*. Only these last have been used during this work and the mechanism behind them will be described in CHAPTER 5.

2.3 Gas sources in Vacuum Systems

Different gas sources are present in every vacuum system, as it possible to see in Figure **10**: permeation, leaks, and internal gas sources are the principal causes.

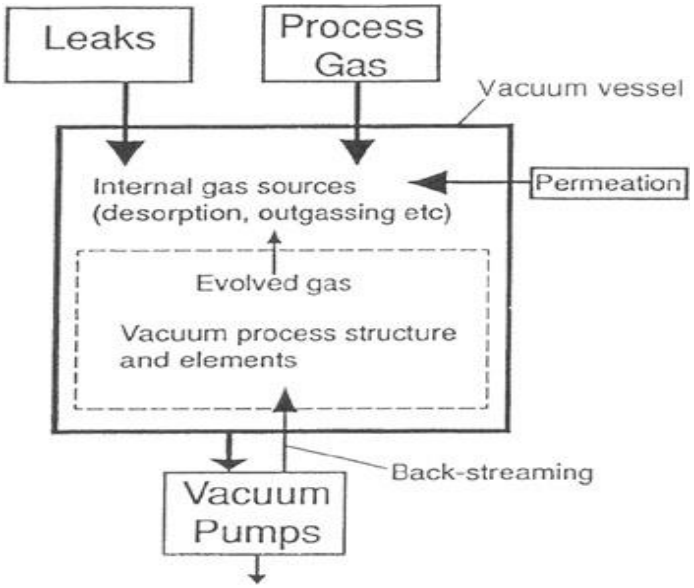

Figure 10: Gas sources in Vacuum Systems[8].

- Leaks: undesired flow entering in the boundary of a considered vacuum system. They can be due to fabrication defects, and mounting of components (welding, knifes of flanges, valves, etc.) or from cracking/scratching due to applied strains. They introduce inside the vacuum system a flow of undesired gas (not only external gasses like air, but also from other closed volumes of the same vacuum system), thus compromising the required vacuum conditions.

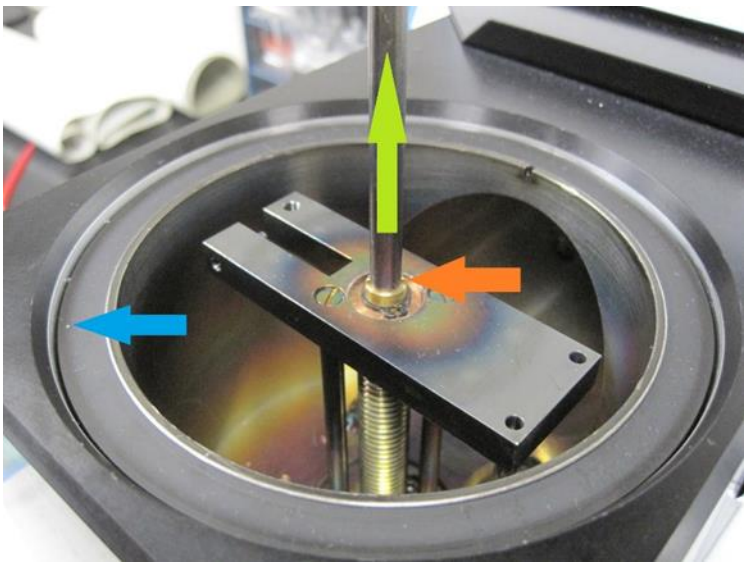

Figure 11: Defects responsible of possible leaks in a vacuum system

- Permeations: gas adsorbed at the outer wall is dissolved in the material, diffuses through it and desorbs from the inner wall, i.e. inside the vacuum system. Permeability depends directly on the type of gas, the type of material and strongly increases with the temperature. Considering its molecular small dimension, the highest permeability for a gas is observed with H_2[9].

Figure 12: Permeation of a polymeric spherical element inside a vacuum system

Permeation is an important limitation of polymers used as seals: atmospheric gas penetrates into the material and diffuses towards the vacuum system. The permeation flow may limit the ultimate water vapour pressure in vacuum systems and affect the sensitivity of helium leak-detection. As an example, the permeation flow of atmospheric water through a Viton O-ring, 5 mm cross section diameter, 6 cm torus diameter, is about 10^{-7} mbar·l·s^{-1}. The stationary condition (ultimate permeation) will be attained after about two months[5].

- Internal sources: release of molecules from materials, which represents in most of the cases, the dominant effect in the free molecular regime. These releases can be defined as:
  - *Outgassing*: spontaneous removal of gas due to thermal desoprtion of molecules.

  - *Degassing*: forced removal of gas due to specific phenomena, as heating at higher temperatures or bombarding the surface with particles (photons, electrons, ions).

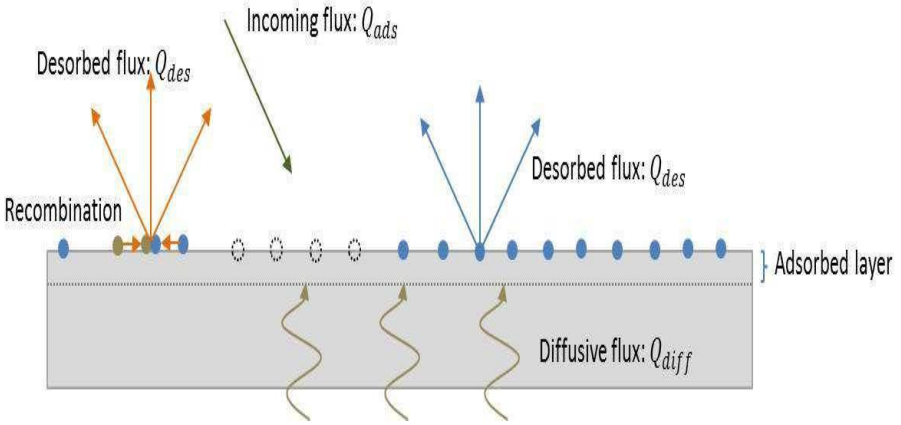

Figure 13: Internal gas sources for a general surface

2.3.1 Water outgassing in metals

The choice of the components in vacuum technology does not concern only the permeation and the thermo-mechanical characteristics of a material, but also its outgassing behaviour. As it is shown in Table 2.7, metals and polymers have different solubility and mobility.

Materials	Characteristics that determine outgassing
Polymers	Dissolve entire molecules, for example H_2O, O_2, CO_2,solvents, etc.
	The solubility in the bulk can be very high in particular for H_2O (up to a few weight percentage)
	The dissolved molecules have a relatively high mobility
Metals	Only single atoms are dissolved (H,O,C,S,etc.)
	The atom solubility is in general very low at room temperature (typically up to 10^3 at. ppm)
	Only H has a significant mobility at room temperature

Table 2.7 Relevant characteristics of polymers and metals for vacuum applications[5]

In Table 2.8 the rubber/polymeric values (Perbunan, Viton) are considerably higher than the metals. Therefore, vacuum technology is focused only on metallic components.

Material	$K\ (mbar\ l\ s^{-1}\ cm^{-2})$
Aluminium (fresh)	$9\ x\ 10^{-9}$
Aluminium (20h at 100°[C])	$5\ x\ 10^{-14}$
Stainless steel (304)	$2\ x\ 10^{-8}$
Stainless steel (304, electro polished)	$6\ x\ 10^{-9}$
Stainless steel (304, mechanically polished)	$2\ x\ 10^{-9}$
Stainless steel (304, electro polished, 30h at 250°[C])	$4\ x\ 10^{-12}$
Perbunan	$5\ x\ 10^{-6}$
Pyrex	$1\ x\ 10^{-8}$
Teflon	$8\ x\ 10^{-8}$
Viton A (fresh)	$2\ x\ 10^{-6}$

Table 2.8 Approximate outgassing rate K for several vacuum materials, after one hour in vacuum at room temperature[10]

After manufacturing and assembling, the surface of metals is covered by several contaminants (hydrocarbons, Cl compounds, silicone greases, etc.). Different surface treatments are available in order to remove specific set of contaminations – solvent and detergent cleaning, chemical pickling, acid etching, electro-polishing – which prepare the surfaces to the minimum level of contamination required by the final vacuum conditions. After thorough treatments, various experiments proves that water vapour dominates the outgassing process of metals in vacuum[11 5 12]. Every time a vacuum system is opened to ambient air with its attendant humidity, the internal surfaces become covered with layers upon layers of water molecules. Consider that air at $25^0[C]$ and 50% of relative humidity contains ≈ 15.99 [mbar] of water vapor[13]. Moreover, we note at this point that H_2O- outgassing is not only generated by molecules previously adsorbed, but also by the reaction of iron oxides in the case of stainless steel[14]

$$Fe_xO_y + 2H \rightarrow Fe + H_2O$$

The outgassing rate from the chamber walls at room temperature, is expressed by an empirical equation for smooth metals:

$$Q_{H2O} \approx \frac{3 * 10^{-9}}{t[h]} [\frac{mbar\ l}{s\ cm^2}]$$ Eq. 24

This behaviour, valid for all metals used until now in vacuum systems, is indeed a big limit in terms of *pumping time* and therefore for the achievements of UHV or XHV conditions. It's easy to see that a reduction by a factor 10 is obtainable only by increasing the pumping time by a factor of 10

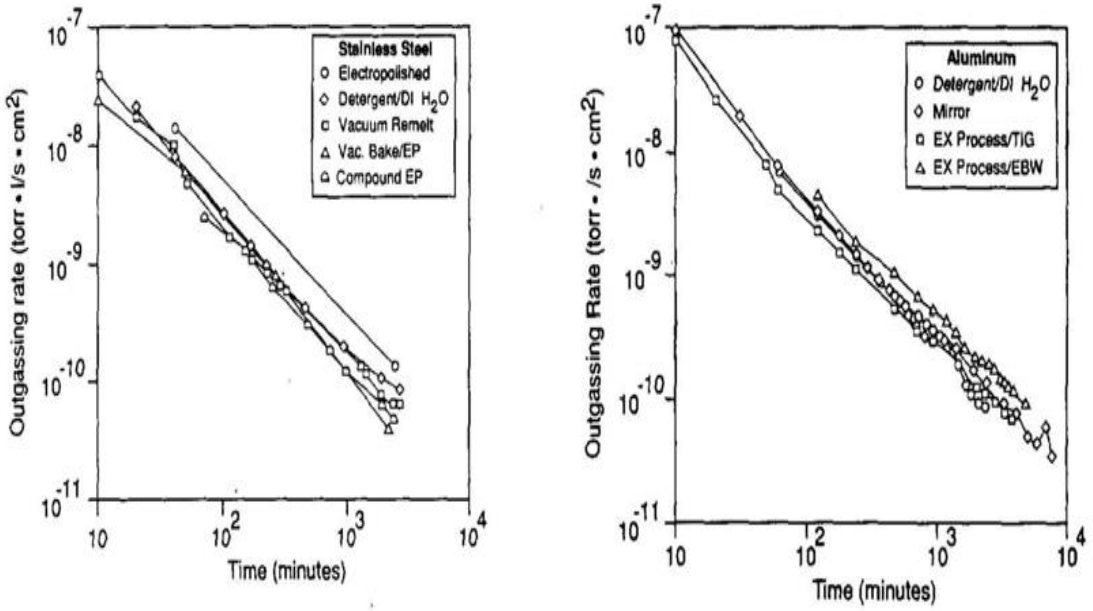

Figure 14: Water vapour outgassing rate of stainless steel and aluminium after four different treatments as measured by Dylla [15]

Still not fully understood, the relationship between H_2O molecules and metal surfaces is such that *the more is removed the harder is to remove.* The molecules spend an average time on the surface before being desorbed which is called mean sojourn time τ. This term is dependant on the superficial temperature and on the molecule binding energy E [4] [16]:

$$\tau = \tau_0 e^{E/RT} \qquad \text{Eq. 25}$$

where τ_0 is the oscillation period of vibration of an adsorbed molecule, of the order od $10^{-13}[s]$. It's easy to notice how is possible to speed up the evacuation in vacuum technology: increasing the system temperature from one side or finding materials which offer lower E_b on the other side. An overview of the typical sojourn times in vacuum system as a function of the binding energy is presented in Table 2.9.

Binding Energy E_b [kcal/mole]	Mean sojourn time τ
10	2.6 μs
15	13 ms
20	66 s
22	33 min
23	3.1 h
24	17 h
25	92 h

Table 2.9 Mean sojourn time for different energies E_b, τ_0=$10^{-13}[s]$, T=295 [K]

At room temperature, water binding energies vary between 15 kcal/mole and 25 kcal/mole (62-100 kJ/mole)[17], which means starting from the weak Van der Waals mutual attraction bond to the chemical bonds. The mean sojourn times are therefore between some minutes and several hours.

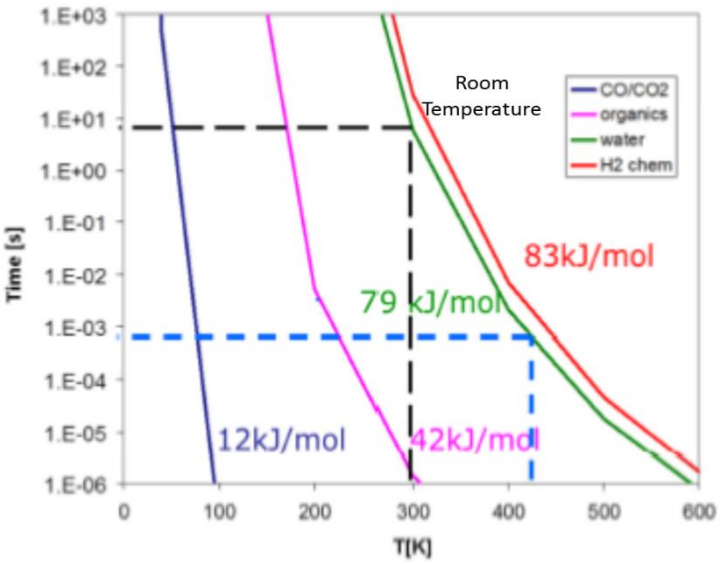

Figure 15: Mean sojourn time as a function of temperature for different gases-surface interactions involving different binding energies

In vacuum technology, this problem is faced acting on the system temperature in two different ways:

- Bake-out: an heating in situ process during the pump-down time. It is effective if it is carried out for at least 12h at temperatures higher than 120^{o} [C]. Following the eq. 2.8, τ goes down due to the higher thermal energy transferred to the molecules. Hence, these last are desorbed and pumped out: a lower final pressure is obtained (Figure 16).

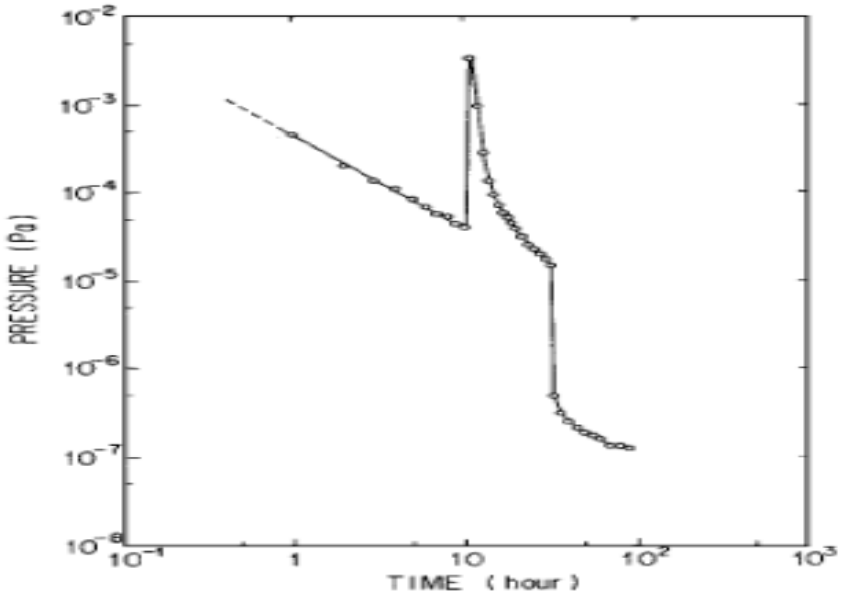

Figure 16: Pressure evolution in a metallic vacuum system. The pressure peak corresponds to the beginning of the bake-out. The pressure drop follows the system cooling to room temperature involving different binding energies [5]

- Cryo-pumping: a permanent cooling of the system under cryogenic temperatures during operation. Here the molecule is not desorbed as before with the bake-out process but is *'frozen'* on the surface, which will avoid it to go in suspension during the UHV operations. A lower pressure is quickly achieved.

2.3.2 The pump down process

The pressure decrease profile from ambient exposure to UHV pressures is called *pump-down curve.* After each exposition air of a vacuum system, every pump down cycle will go through two overlapping stages. Firstly there is the atmospheric gas pumping, where the gases making up the air mixture in the system's volume will be pumped away. Then, the H_2O molecules desorbing from the internal surfaces must be pumped away.

Once the pressure is in the $10^{-6}\ mbar$ range, the desorbing water makes up over 99% of the total gas load. If, for example, you turn on a residual gas analyser (RGA) in the high $10^{-7}\ mbar$ range during a pump-down from air, the O_2 and N_2 will drop off-scale almost immediately while the water vapour peak will be fixed. Alternatively, if you pump a system down to its ultimate pressure of, say $10^{-9}\ mbar$ or $10^{-10}\ mbar$, and then backfill it to atmospheric pressure with dry N_2, it will pump back down to its ultimate pressure again in minutes instead of hours. This is explained by the fact that the pump-down rate is not controlled by the amount of water vapour within the chamber but by *its desorption rate* from the internal surfaces[11].

In any vacuum system, the mass balance equation can always be set as:

$$\frac{\mathrm{V}}{k_B T}\frac{\mathrm{dp}}{\mathrm{dt}} + \frac{\mathrm{S}}{k_B T}p + \frac{dN_a}{dt} = 0 \qquad \text{Eq. 26}$$

where p is the pressure in the gas phase in mbar, S the pumping speed, N_a the number of adsorbed molecules, $\frac{\mathrm{V}}{k_B T}\frac{\mathrm{dp}}{\mathrm{dt}}$ the dynamic change of number of molecules in the gas

phase (from the condensed one) and $\frac{S}{k_B T} p$ is the gas phase flow leaving the system, pumped out by the pumping system. The third term $(\frac{dN_a}{dt})$ can be defined as the net flow to the surface from the gas phase[17]:

$$\frac{dN_a}{dt} = Q_{ads} - Q_{des} \qquad \text{Eq. 27}$$

where $Q_{ads} and\ Q_{des}$ represent the flow of molecules respectively adsorbed and desorbed by the surface exposed to vacuum. As we said, at the beginning of the pump-down the main contribution to the pumped flux is given by the atmospheric gases present in the volume. In this situation, the influence of the desorbed flux is negligible[4]. The mass balance becomes:

$$V\frac{dp}{dt} + Sp = 0 \qquad \text{Eq. 28}$$

The solution of this differential equation gives an exponential decay seen in the first part of the pump-down curve in :

$$p = p_0 e^{\frac{-t}{\tau_p}} \qquad \text{Eq. 29}$$

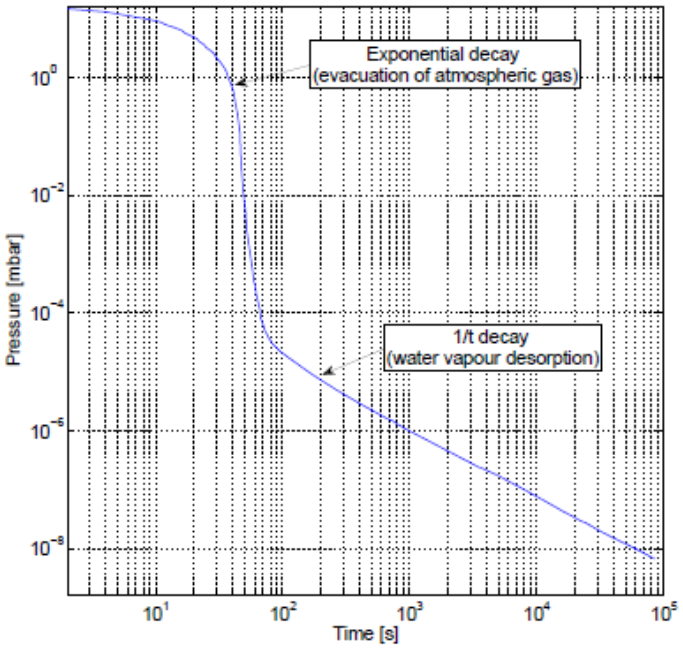

Figure 17: Pump down for a SS 316L chamber at 293 K

where $\tau_p = \frac{V}{S}$ is the characteristic pumping time.

As is possible to see, the second part of the trend is dominate by water vapour degassing, with the classical $1/t$ (in double log scale) behaviour.

This behaviour is describable as a *quasi-static solution* of the eq. considering the adsorption/desorption process fully reversible. This is possible when the gas and surface phases reach the equilibrium in a characteristic time short if compared to the time of an observable pressure change[17]**.**

In other words:

$$\left|\frac{1}{p}\frac{dp}{dt}\right| \ll s\frac{A}{V}\cdot\frac{\bar{v}}{4} \qquad \text{Eq. 30}$$

(where s is the sticking probability and $\bar{v}$ is the average molecular velocity). Kanazawa[18] has shown that provided the rate of change of pressure obeys this last inequality that a quasi-static solution is capable of following the pressure change. Using i.e. $\bar{v} = 5.94 \cdot 10^4 \frac{cm}{s}$, with a typical chamber of SPS or PS accelerators of $V = 16.7\ l$ and an internal surface area $A = 4.75 \cdot 10^3 cm^2$,for water at 300 K we find that:

$$\left|\frac{1}{p}\frac{dp}{dt}\right| \ll s\ 4.2\ \cdot 10^3[\frac{1}{s}] \qquad \text{Eq. 31}$$

When $p = 10^{-8} Torr$ (with $s = 10^{-1}$) $\frac{dp}{dt} \ll 4.2 \cdot 10^{-6}\frac{Torr}{s}$.

When $p = 10^{-4} Torr$ (with $s = 10^{-3}$) $\frac{dp}{dt} \ll 4.2 \cdot 10^{-4}\frac{Torr}{s}$.

During the pump-down of a typical vacuum system the rate of change of pressure is well below these limits and thus the quasi-static solution is applicable. At the beginning of the pump down, when observable changes in pressure occur in seconds, molecules with E≈15 $\frac{kcal}{mole}$ are desorbed. At the end of the process, when measurable

changes in pressure occurs in hours, molecules with E≈22÷ 23 $\frac{kcal}{mole}$ are desorbed ($\tau = 30\,\mathrm{min} \div 3$ hours, see Tab.2.7): sojourn times of molecules are lower than the time it takes for observable changes in pressure.

The study of the sojourn time and the comprehension of the sticking probability related to different surfaces will be widely treated during this thesis work.

2.4 Vacuum Instrumentation

Pressure measurement is at the basics of vacuum technology. Since is impossible to cover with one instrument the entire range of measure, is necessary to use different sensors, often with different working principles.

Depending on method to measure the pressure, is possible to classify the instruments in two categories:

- Direct pressure measurements instruments ;
- Indirect pressure measurements instruments.

In the first case, pressure is directly measured as a force F exerted on a surface A.

Common manometers are devices typically used for direct pressure measurements. More specific ones are the *diaphragm vacuum gauges,* in which a deformation of a sensitive element due to an applied force is involved: the resulting reflection is estimated mechanically or electrically (piezo-diaphragm gauges)

This process does not depend on the nature of the analysed gas or gas mixture; at low pressure (less than 1 mbar) however, the exerted forces are negligible, thus the performance of direct measurements becomes very difficult or even impossible due to the infinitesimal masses involved. In this situation, which is common concerning to applications in high and ultra-high vacuum, indirect methods are required.

Indirect measurements monitor either particle number density or a gas property which depends on it, taking into account that pressure is proportional to particle number density at constant temperature. These methods depend on the gas type because the physical properties which are measured (e.g. thermal transfer and ionisation capacity) are functions of both pressure and molecular weight.

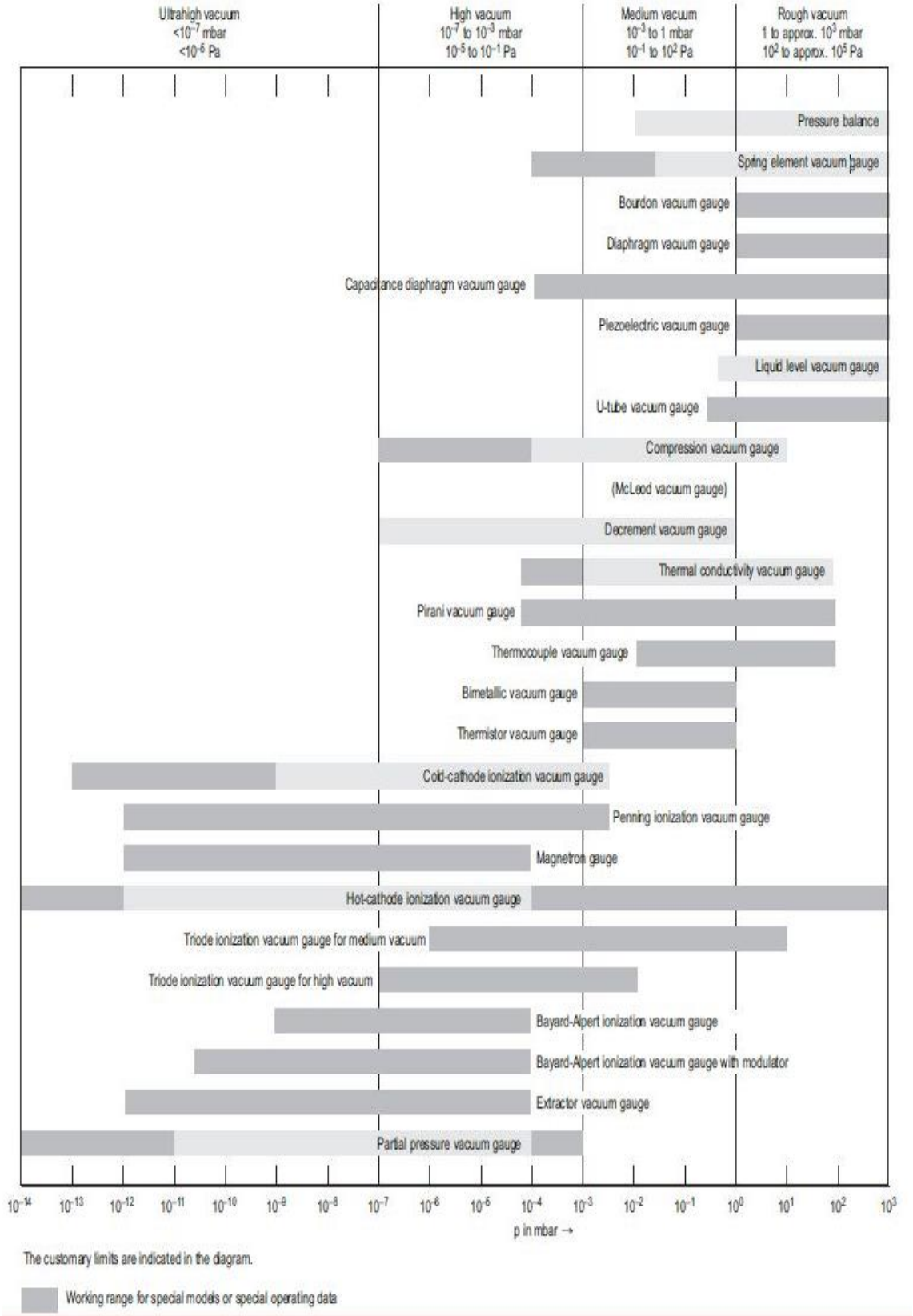

Figure 18: Measurement ranges of common vacuum gauges[19]

2.5 Software

Experimental data related to vacuum systems need to be predicted and sometimes *benchmarked* by simulations, provided nowadays by several software. Vacuum systems are usually expensive to prototype. Therefore, an increased use of simulations in the design process can result in substantial cost savings.

Quantity as conductance, capture probability, time-dependent pressure evolution or sticking factors are mainly calculated by Test-Particle Monte Carlo methods (TMPC). The system is first modelled in three dimensions (with another editor software) and then, once imported, TMPC code generates molecules at the entrance of the component itself, pointing in "random extracted" angles according to the chosen distribution. When the molecule leaves the wall, the most important thing is *his direction (*no matter what happen inside the chamber, in molecular flow we already said that collisions between molecules can be neglected) because the program will follow the molecular trace until it reaches the "exit from the system" (which means exit from the component, trapping on a pump, sticking on a surface). Many simulated trajectories are needed to reduce the statistical scattering.

2.5.1 MOLFLOW+

The reference TMPC software at CERN is MOLFLOW+[20]**.** This tool is able to import 3D drawings of vacuum components, create a map of *facets* (similar to finite element mesh) and generate fluxes of molecules on the surface of interest. The program can also simulate the presence of different pumping systems, either localized (sputter-ion pumps) or distributed (NEG coatings). NEG sticking factor, entering molecular flow, outgassing from a surface, temperature and molecular mass are among the parameters that can be set before starting the simulation. Is able moreover to evaluate the tightness of the component imported, showing the leaks related to its potential assembly and materials. A powerful time-dependent tool is finally provided.

Figure 19 and Figure 20 show an example of output provided by MOLFLOW+ on an imported geometry:

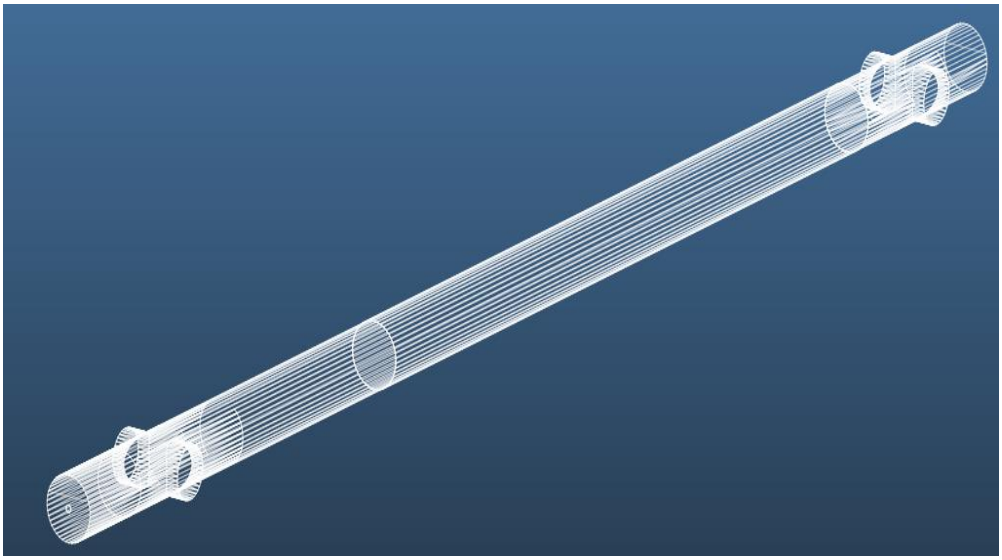

Figure 19: Creation of facets on a 1590 mm NEG-coated LHC chamber by MOLFLOW+

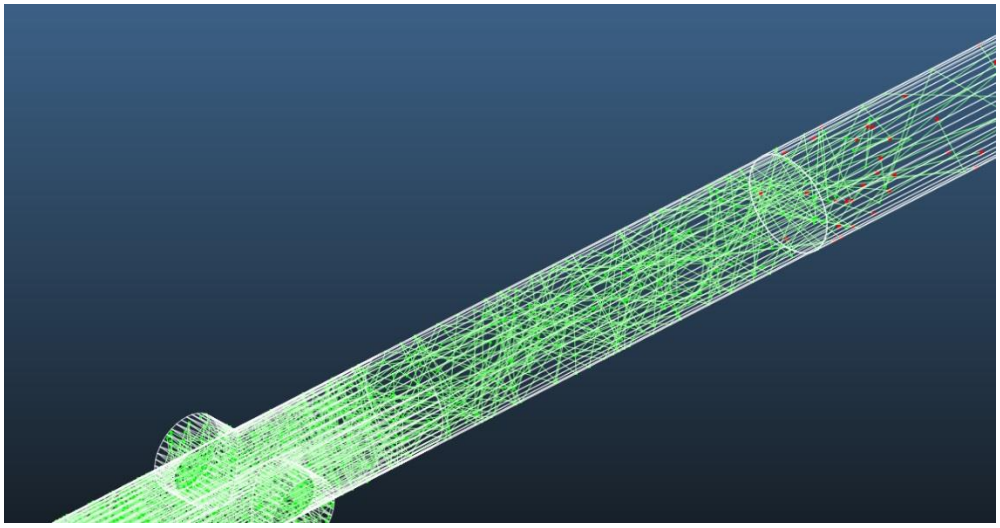

Figure 20: Molecular tracks (in green) generated by MOLFLOW+ code and hits on the chamber walls (in red)

Using MOLFLOW+, one of the most important parameter is the choice of the *particle reflection model* to be used. There are two types of reflection models: stochastic and deterministic. The stochastic model describes a *diffuse reflection*, such as the cosine law of reflection, where gas molecules striking the wall are re-emitted in a probabilistic way irrespective of their incident conditions. Here the probability *ds* that a molecule leaves the surface in the solid angle $d\omega$ forming an angle θ with the normal to the surface is:

$$ds = \frac{d\omega}{\pi} cos\ \theta \qquad \text{Eq. 32}$$

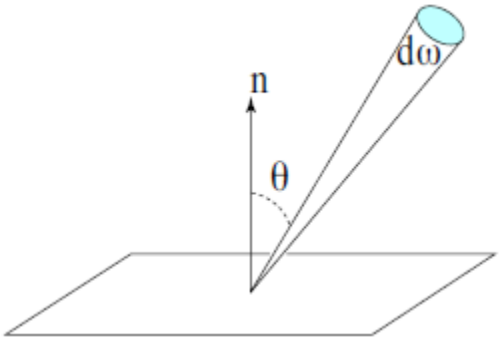

Figure 21: dω is the solid angle in the expression of the cosine law. The distribution of scattered velocities is independent of the incidence angle.

The deterministic model describes a beam reflection, such as the *specular reflection*. Here the path of each molecule is uniquely determined by its initial condition.

The diffusive mode solves the *Clausing's integral equation*, which gives us the transmission probability for cylindrical chambers. For a cylindrical tube of length L (all lengths here are normalized in term of the tube radius; that is r = 1) and axials coordinates x and y, the Clausing's integral is given by eq.:

$$y(x) = y_0(x) + \int_0^L K(x, x')y(x')\,dx' \qquad \text{Eq. 33}$$

where

$$y_0(x) = \frac{1}{2}\left\{\frac{x^2 + 2}{\sqrt{x^2 + 4}} - x\right\} \qquad \text{Eq. 34}$$

And

$$K(x,x') = \frac{1}{2}\left\{1 - |x - x'| \frac{6 + (x - x')^2}{[4 + (x - x')^2]^{\frac{3}{2}}}\right\} \qquad \text{Eq. 35}$$

The transmission probability W(L) expressed as an integral on y(x):

$$W(L) = \frac{1}{L}\int_0^L \left(x^2 + 2 - x\sqrt{x^2 + 4}\right) y(x)\, dx \qquad \text{Eq. 36}$$

This is a Fredholm equation of the second type, and its accurate numerical solution is feasible using MOLFLOW+.

2.5.2 COMSOL

COMSOL Multiphysics is a finite-element-analysis simulation software used for various physics and engineering applications, especially when is needed to couple different physics phenomena with a useful multi-physics interface. It is able to import 3D geometries as (and better) than MOLFLOW+ and permits also to design simple geometries with his own editor.

For vacuum systems purposes is available the *Free Molecular Flow* package*,* based on a finite element solver, different from the TMPC of MOLFLOW+ or the finite volume method (FVM) used by Ansys®. Figure 22 shows how the analysis are performed by COMSOL *Fast Angular Coefficient Method.* This tool enables to run quick parametric studies of chamber geometries and physical properties of the mesh:

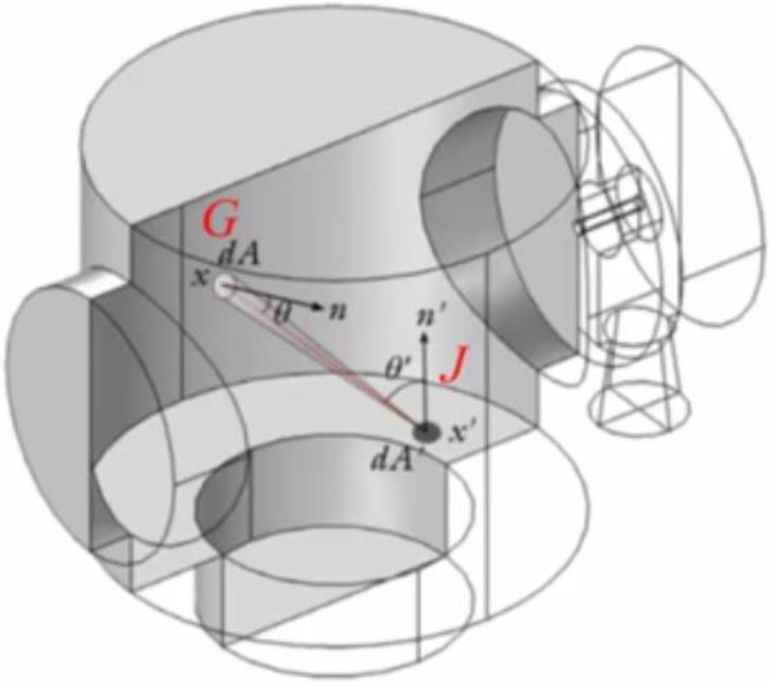

Figure 22: Angular Coefficient Method in Comsol

The number of molecules emitted from x' that reach x depends on:

- The angular distribution of emission at x'
- The distance between x and x'
- The angle between the surface normal and the line joining x and x'

To compute the total number of molecules arriving at x, a surface integration must be performed over all the surfaces in the line of sight of x.

The great advantage showed by COMSOL in respect of MOLFLOW+ was to permit and calculate dynamic changing in the physical characteristics of the mesh during a time-dependent simulation, as we will see on CHAPTER 4.

CHAPTER 3
THE STICKING PHENOMENON

3.1 Sticking of molecules

The phenomenon of the sticking is widely present in vacuum technology. Impinging molecules naturally stick on the surfaces, with a certain probability, providing delays in the pumping time. Some other times instead, this phenomenon can be specifically adopted as a trapping solution, so having benefit from it.
Concerning the spontaneous and most of the time undesired one, it is easy to think about molecules such as H_2O and CO, the first with almost the same behavior on every metal and the second just on specific technical ones, as we will see. For this reason, sticking is the main problem when the goal is to achieve UHV/XHV conditions. In this chapter there will be shown the models and working principles behind various sticking molecules-to-wall phenomena and different materials adopted to solve or even benefit from that processes.

In surface physics, the *sticking coefficient s* is the term used to describe the ratio of the adsorbate atoms which "stick" on the surface to the total number of those that impinge upon the surface itself.

$$0 < s < 1 \qquad \text{Eq. 37}$$

Considering an *adatom,* which can be thought to be as the opposite of a surface vacancy[21], is possible to define a probability to be adsorbed on the surface (P_a), a probability to migrate to another site on the surface (P_m) and one to be desorbed from the surface and to return to the gas phase (P_d). For an empty site (θ=0) the sum of these three options is unity.

$$P_a + P_m + P_d = 1 \quad \text{Eq. 38}$$

For a site already occupied by an adatom (θ>0), there is no probability of adsorbing, thus:

$$P'_m + P'_d = 1 \quad \text{Eq. 39}$$

For the first site visited, the P of migrating overall is the P of migrating if the site is filled plus the P of migrating if the site is empty. The same is true for the P of desorption. The P of adsorption, however, does not exist for an already filled site.

$$P_{m1} = P_m(1-\theta) + P'_m(\theta) \quad \text{Eq. 40}$$

$$P_{d1} = P_d(1-\theta) + P'_d(\theta) \quad \text{Eq. 41}$$

$$P_{a1} = P_m(1-\theta) \quad \text{Eq. 42}$$

It is possible to extend these considerations also to the second site, considering that the P to migrate from it is the one from the first site and then from the second site:

$$P_{m2} = P_{m1} + P_{m1} = P_{m1}^2 \quad \text{Eq. 43}$$

Thus, considering that the sticking probability is the total sum of direct adsorption on the first site plus all the other adsorption probabilities after migrating from the other sites, we can write:

$$s = P_a(1-\theta) + P_{m1}P_a(1-\theta) + P_{m1}^2P_a(1-\theta) \ldots \quad \text{Eq. 44}$$

$$s = P_a(1-\theta) + \sum_{n=0}^{\infty} P_{m1}^{n} \qquad \text{Eq. 45}$$

Sticking coefficients are therefore an important part of every adsorption model as directly proportional to the pumping speed, as we will see in the next sections of this chapter.

3.2 Water adsorption model

As it was shown in section 2.3, water desorption is the dominant outgassing phenomenon for metals in vacuum technology. Looking to Figure 13, one would wonder if the process is dominate by the Q_{diff} (Diffusive flux: H_2O coming from the bulk is leading the phenomenon) or by the Q_{des} (Desorbed flux: the rate of adsorption is the prevailing process). Different scientists are lined up with the first theory (Li and Dylla) and others with the second one (Redhead, Kanazawa, Horikoshi).

Concerning this master thesis work, it was decided to follow the adsorption isotherm models (indeed neglecting the possible contribution of water diffusion) because of their good agreement with the experimental data and for that their great development in literature[18] [17] [22].

An *adsorption isotherm* is the amount of adsorbate on the adsorbent as a function of its pressure (if gas) or concentration (if liquid)[23]. In other words, a function that describe the equilibrium between adsorbed and gas phases at a constant pressure[17]. For this kind of studies, the only influent parameters are the coverage factor θ and the distribution of binding energies $\rho(E_b)$.

The *adorption isotherm model* is based on the following hypothesis and definitions:

- The surface is seen as an ensemble of N_{sites} sites. Each site is considered filled with only one molecule, without dissociation as shown by Kanazawa. The ratio of the number of filled sites N_a to the total number of available sites N_{sites} is called surface coverage θ:

$$\theta = \frac{N_a}{N_{sites}} = \frac{n_a}{n_{sites}} \qquad \text{Eq. 46}$$

Here $\boldsymbol{n_a}$ is no more the number of site but the *density* of filled sites, whereas $\boldsymbol{n_{sites}}$ represents the surface density of the total available sites.

- The surface has a sticking probability $\boldsymbol{s}$ (i.e. the probability that an impinging molecule is captured by a site) equal and constant for all water sites [22]

- The quasi-static solution and the reversibility condition are fulfilled as we have seen in 2.3.1

This last satisfied condition implies the principal consequence at the basis of the model, that is the possibility to express the surface coverage as a *function of pressure:*

$$\theta = \frac{N_a}{N_m} = \frac{n_a}{n_m} = f(p, T) \qquad \text{Eq. 47}$$

This is indeed the *Henry's law* ,where m indicates the coverage correspondent to a *monolayer.* A monolayer refers to a single, closely packed layer of atoms or molecules[24]. Even if the precise value corresponding to a water monolayer density on metals is still not precise and univocally determined, for this master thesis purposes it has been used :

$$1ML = 6 \cdot 10^{15} \left[\frac{molecules}{cm^2}\right] \qquad \text{Eq. 48}$$

Substituting eq. **47** in eq. **26** we obtain:

$$\frac{1}{p}\frac{dp}{dt}\left(1+\frac{N_m k_B T}{V}\frac{1}{p}\frac{d\theta}{dt}\right)=-\frac{1}{\tau_p} \qquad \text{Eq. 49}$$

Where τ_p is the characteristic pumping time as we have seen in 2.3.2.

Thus, in isothermal conditions, since:

$$\frac{1}{p}\frac{dp}{dt}\left(\frac{d\theta}{dp}\right)=\frac{1}{p}\frac{d\theta}{dt} \qquad \text{Eq. 50}$$

We can write a first important equation for variable pressures:

$$\frac{1}{p}\frac{dp}{dt}\left(1+\frac{N_m k_B T}{V}\frac{d\theta}{dp}\right)=-\frac{1}{\tau_p} \qquad \text{Eq. 51}$$

And adding the possibility to have variable temperatures:

$$\frac{1}{p}\frac{dp}{dt}\left(1+\frac{N_m k_B T}{V}\frac{d\theta}{dp}\right)+\frac{1}{p}\frac{dT}{dt}\left(1+\frac{N_m k_B T}{V}\frac{d\theta}{dT}\right)=-\frac{1}{\tau_p} \qquad \text{Eq. 52}$$

Which means:

$$\frac{dp}{dt}=-\frac{p+\frac{1}{p}\frac{dT}{dt}\left(1+\frac{N_m k_B T}{V}\frac{d\theta}{dT}\right)}{\tau_p\left(1+\frac{N_m k_B T}{V}\frac{d\theta}{dp}\right)} \qquad \text{Eq. 53}$$

Which is finally the most general form for this pump down model.

From this last, specific solutions for pressure evolution can be extracted when the right isotherm expression θ(p,T) and the temperature evolution $\frac{dT}{dt}$ are weell known. The next section will be focused on the different types of isotherms to be adopted, respectively with their influences on the pump-down models.

3.3 Choice of the isotherm

As we have said, an adsorption isotherm is a function which use the θ in respect of a certain $\rho(E_b)$. This function has to be substituted then in eqz. 53 and compared with the experimental data.

The principal types of adsorption isotherms are listed in Table 3.1

Isotherm name	Energy Distribution	Behaviour
Langmuir	$E_d = E$	Constant energy for every coverage
Freundlich	$E_d = -E' ln\theta$	Logarithmic dependence on coverage
Horikoshi-Temkin	$E_d = E_0(1 - \alpha\theta)$	Linear dependence on coverage
Sips	$E_d = -E' ln\theta$ $(Finite\ Area)$	Logarithmic dependence on coverage but finite energy boundaries

Table 3.1: Principal adsorption isotherms with their respective energy distribution.

Each distribution of energies considered leads to a coverage function, which is calculable starting from the Langmuir isotherm (the simplest case of single adsorption energy E distribution):

$$\theta(p) = \int \rho(E)\, \theta_L(p, E) dE \qquad \text{Eq. 54}$$

In Figure 23 is possible to better understand how the binding energy ($\boldsymbol{E_d}$ or $\boldsymbol{E_b}$) of each molecule varies with the coverage for each isotherm. Moreover, is shown how the distribution of energy varies depending of the different slope of each distribution:

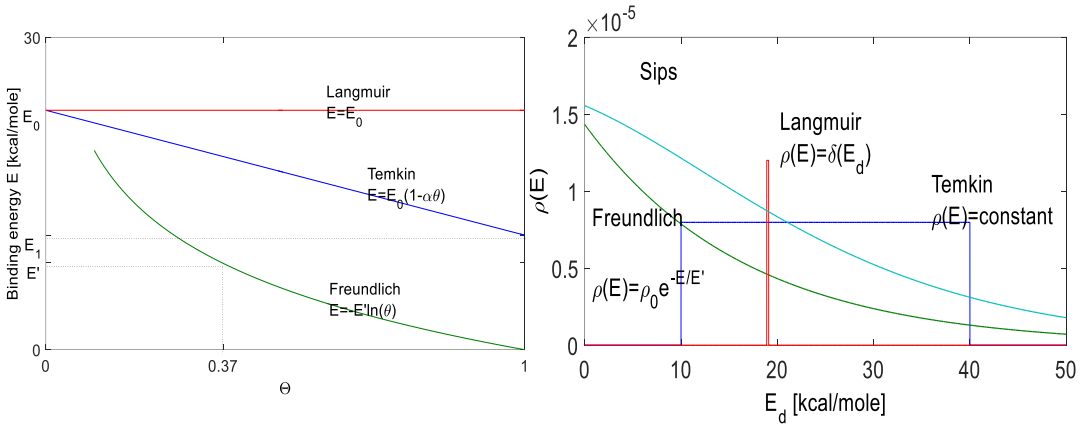

Figure 23: Diagrams of binding energy E_d vs coverage θ (left), and density of adsorption sites ρ vs binding energy, for the four considered isotherms[17]

3.3.1 Langmuir isotherm

The Langmuir isotherm is the simplest between the ones enunciated above. The rate of adsorption is proportional to the number of empty sites, and the rate of desorption is proportional to the number of filled sites. The binding energy E_d is assumed constant for any coverage[25]

The desorbed flux can be expresses as:

$$Q_{des} = \frac{\theta n_m}{\tau} \qquad \text{Eq. 55}$$

And the adsorbed one can be obtained as:

$$Q_{ads} = (1-\theta) s_0 p v \qquad \text{Eq. 56}$$

With s_0 the *sticking probability* for an empty site. As we have said in section 3.2, an adsorption isotherm is an equilibrium function, so at the equilibrium, where:

$$Q_{ads} - Q_{des} = 0$$

So,

$$\frac{\theta n_m}{\tau} - (1 - \theta) s_0 p v = 0 \qquad \text{Eq. 57}$$

Thus is obtained the expression for the Langmuir isotherm:

$$\theta_L = \frac{ap}{1 + ap} \qquad \text{Eq. 58}$$

Where the parameter a is [25] [17] :

$$a = \frac{s_0 \tau_0 v}{n_m} e^{\frac{E_d}{RT}} \qquad \text{Eq. 59}$$

Finally, applying eq. 58 to eq. 51 is possible to calculate the pump-down of a surface obeying this Langmuir isotherm law. In Figure 24 is shown an example of these calculations output: different binding energies lead to different slope of the curves.

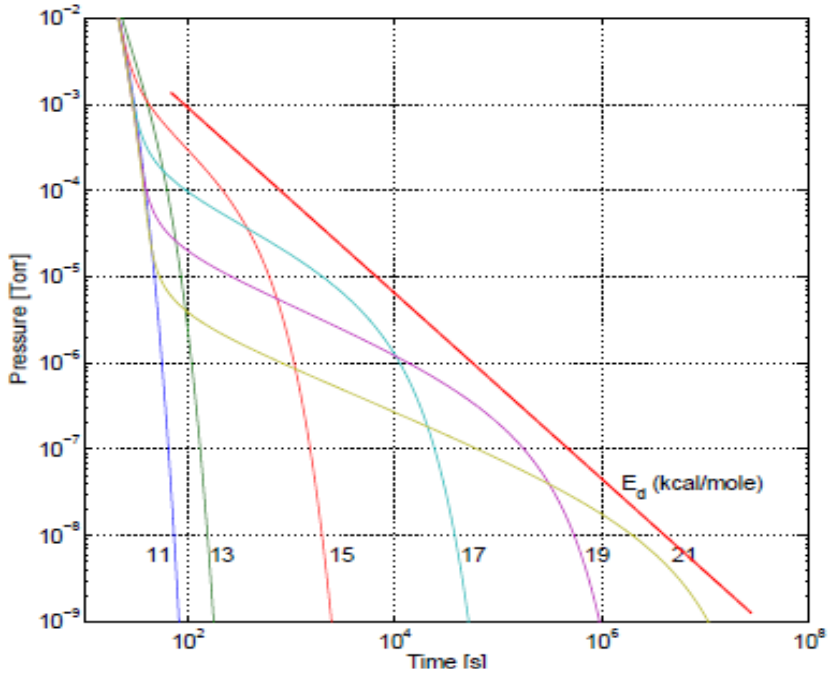

Figure 24: Pump-down curves for a vacuum system with reversibly adsorbed layer obeying to Langmuir adsorption for different adsorption/desorption energies (11 to 21 kcal/mole)[17]. Other parameters: $n_m = 3 \cdot 10^{15}\ [\frac{molecules}{cm^2}]$, $\tau_0 = 10^{-13}\ [s]$, $s_0 = 1$, $A = 4740[cm^2]$, V $= 16.7[l]$, pumping speed for nitrogen $S = 4.7\ [\frac{l}{s}]$ and $T = 295\ [K]$

The convolution of these curves for different values of E_d approximates, as it is underlined in red, a straight line with slope -1. This observation is the chain between the theoretical models and the everyday experience in metal materials in vacuum: it shows that $1/t$ behavior can be simulated by taking into account the whole spectrum of binding energies provided between H_2O and metals.

3.3.2 Horikoshi-Temkin isotherm

Horikoshi-Temkin isotherm is, after the Langmuiran, one of the earliest reported isotherms proposed[26]: he noted experimentally that heats of adsorption would more often decrease than increase with increasing coverage. For this reason, this model assumes that the heat of adsorption decreases linearly with increasing coverage:

$$E_d = E_0(1 - \alpha\theta) \qquad \text{Eq. 60}$$

where α is a constant for a given adsorbate and adsorbent at a particular T.

Or, speaking about energy distribution:

$$\begin{cases} 0 & if\ E_1 < E\ \ and\ E > E_0 \\ \dfrac{1}{E_0 - E_1} & if\ \ E_1 <\ E < E_0 \end{cases} \qquad \text{Eq. 61}$$

Where E_1 is the heat of adsorption at $\theta = 1$ and E_0 is the heat of adsorption at $\theta = 0$. The isotherm function may be derived directly from the Langmuir isotherm using eq.54 . Indeed, imaging a non-uniform surface, if we divide it into a number of uniform elements di with a $constant$ heat of adsorption, each element will obey to the Langmuiran isotherm. Thus:

$$\theta(p) = \int_{E_1}^{E_0} \frac{1}{E_0 - E_1} \frac{p \frac{s_0 \tau_0 \nu}{n_m} e^{\frac{E_d}{RT}}}{1 + p \frac{s_0 \tau_0 \nu}{n_m} e^{\frac{E_d}{RT}}} dE$$

Which leads to:

$$\theta_T = \frac{RT}{E_0 - E_1} \ln\left(\frac{1 + \frac{p}{p_*} e^{\frac{E_0}{RT}}}{1 + \frac{p}{p_*} e^{\frac{E_1}{RT}}} \right) \qquad \text{Eq. 62}$$

Where $p_* = e^{\frac{E_d}{RT}} / a$.

As is possible to verify, the more complex form of this isotherm in respect of the Langmuir one (three main parameters -E_1, E_0 and n_m- instead of two) will equally give a $1/t$ behavior once substituted in eq. 51. Here is possible to notice that energy

boundaries change can give big variations on the pump-down curve, in particular increasing/decreasing E_0 as is underlined in Figure 25:

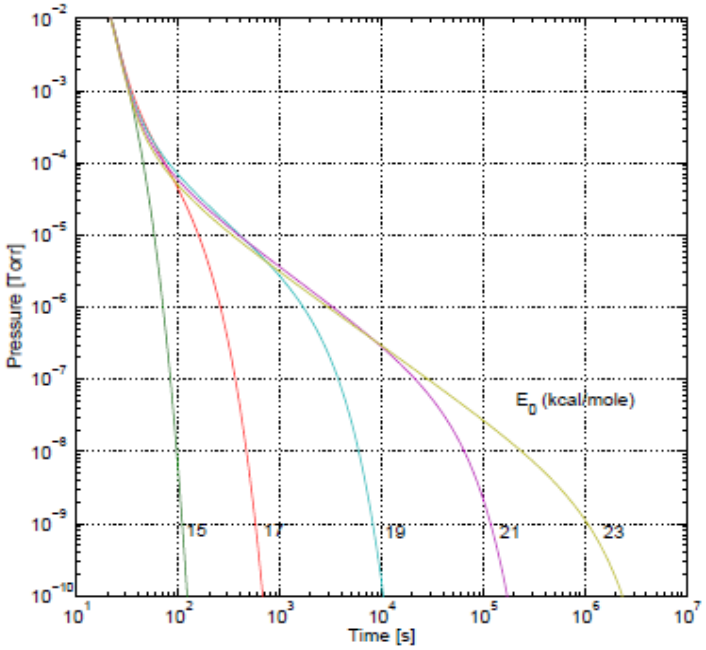

Figure 25: Variation of pump-down curve following the change of E_0 energy. Data for calculations[17]: $n_m = 2 \cdot 10^{16}[\frac{molecules}{cm^2}]$, $E_1 = 10.6\ [\frac{kcal}{mol}]$, $\tau_0 = 10^{-13}\ [s]$, $s_0 = 1$, $A = 4740\ [cm^2]$, $V = 16.7\ [l]$, $S = 4.7\ [\frac{l}{s}]$.

Concerning a possible Δn_m, the influence on the pump-down curve are showed in Figure 26:

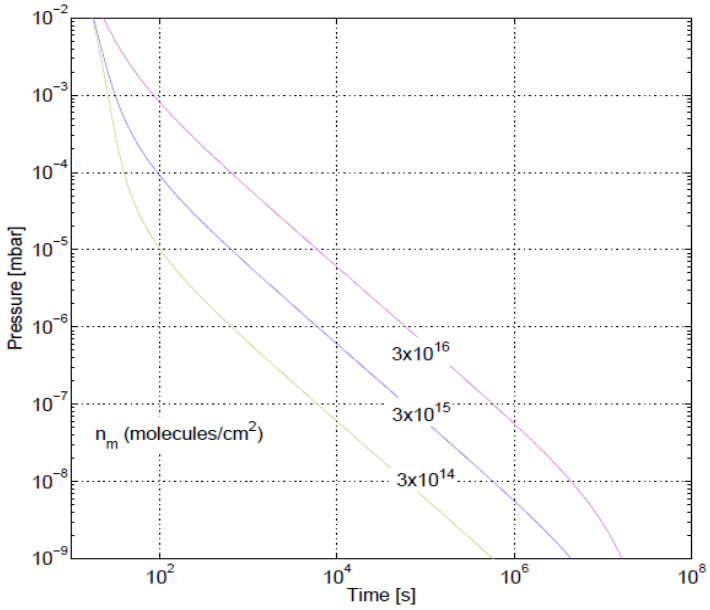

Figure 26: Variation of pump-down curve following the change of n_m. Data for calculations are the same of Figure 25

3.3.3 Freundlich isotherm

As the Temkin isotherm, also the Freundlich isotherm can be derived from the Langmuir one as on a heterogeneous surface (also here each uniform element di has a constant heat of adsorption). Here is assumed a binding energy which varies logarithmically with the coverage[17] as:

$$E_d = -E' ln\theta \qquad \text{Eq. 63}$$

Or, speaking about energy distribution:

$$\rho(E) = ke^{-kE} \qquad \text{Eq. 64}$$

where E' is the adsorption energy for $\theta = 0.37$ and $k = 1/E'$.

Using again eq. 54, we have

$$\theta(p) = \int ke^{kE} \frac{p\frac{s_0\tau_0 v}{n_m}e^{\frac{E_d}{RT}}}{1 + p\frac{s_0\tau_0 v}{n_m}e^{\frac{E_d}{RT}}} dE$$

Thus, after few calculations, it gives:

$$\theta_F = \frac{\pi kRT}{sin\,\pi kRT}\left(\frac{p}{p_*}\right)^{e^{\frac{RT}{E'}}} \cong \left(\frac{p}{p_*}\right)^{e^{\frac{RT}{E'}}} \qquad \text{Eq. 65}$$

where, as before, $p_* = e^{\frac{E_d}{RT}}/a$.

It's important to notice the great limits of the Freundlich isotherm: this last is unrealistic for coverages equal to 1 or 0. Looking indeed to Figure 23, it's possible to see how the Freundlich isotherm gives E_d=0 for $\theta = 1$ and $E_d \to \infty$ for $\theta = 0$. For

this reason, modelling with Freundlich isotherm makes sense only for a limited range of coverages.

The most important parameters in this isotherm are E_0, n_m, s_0, τ_0 . Differently from the Temkin isotherm, their variations (except for the density of sites) have a very little influence on the pump-down curve as is possible to notice in Figure 27. This example shows energy reference variations between $50\ [\frac{kcal}{mole}]$ (very strong bonds) and $10\ [\frac{kcal}{mole}]$ (nearly water condensation energy).

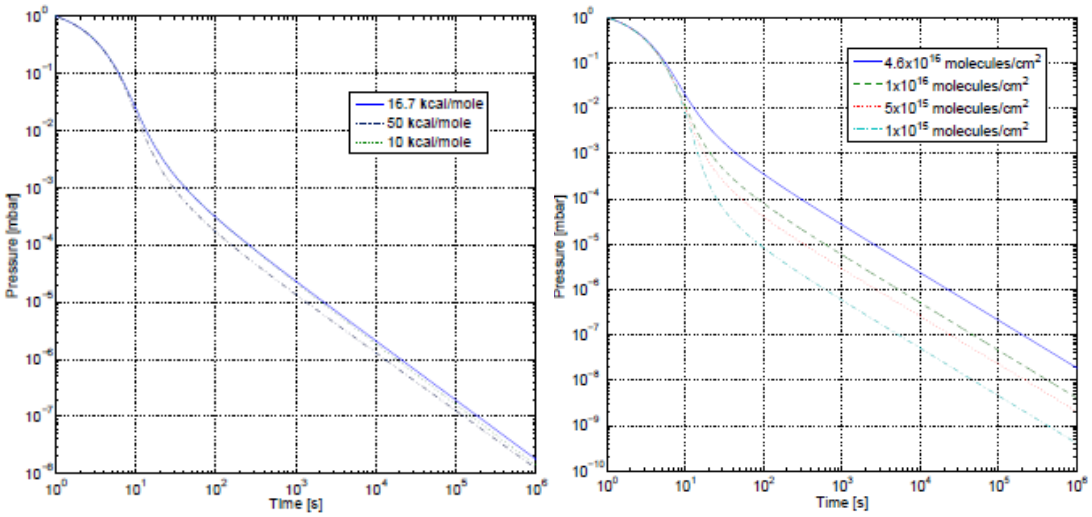

Figure 27: Variation of pump-down curve following the change of E'(on the left) and n_m(on the right). Data for calculations: $n_m = 4.6 \cdot 10^{16}[\frac{molecules}{cm^2}]$, $\tau_0 = 5 \cdot 10^{-11}\ [s]$, $s_0 = 1$, $A = 2600[cm^2]$, $V = 5.1\ [l]$, $S = 3.3\ [\frac{l}{s}]$, $T = 295[K]$

3.3.4 Sips isotherm

Sips isotherm is an adjustment of the Freundlich one toward a feasible complete range of E_d. Since Freundlich isotherm area below its energy distribution is infinite, Sips thought to combine this last with a Langmuir isotherm[27] [28], obtaining:

$$\theta_S = \frac{K_s p^{\beta}}{1 + K_s p^{\beta}} \qquad \text{Eq. 66}$$

where

$$K_s = \frac{s_0 \tau_0 v}{n_m} e^{\frac{RT}{E'}} = \left(\frac{1}{p_*}\right)^{\frac{RT}{E'}} \text{ and } \beta = \frac{RT}{E'}$$

Sips isotherm has the same main parameters of the Freundlich isotherm, which are indeed E' and n_m. Thus, it's easy to imagine the same influence of them on the pump-down curve, with an expected slope affected more by Δn_m than $\Delta E'$. Finally, the two isotherms behaviour tends to coincide for very low pressures (Figure 28)

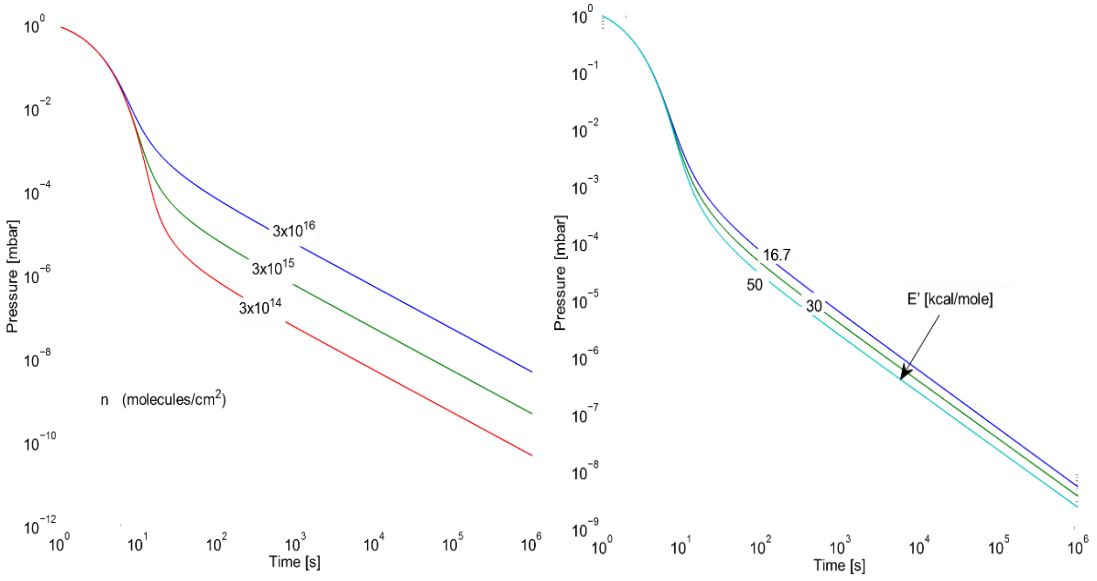

Figure 28: : Variation of pump-down curve following the change of E'(on the left) and n_m(on the right). Data for calculations: $n_m = 4.6 \cdot 10^{16}[\frac{molecules}{cm^2}]$, $\tau_0 = 5 \cdot 10^{-11}\ [s]$, $s_0 = 1$, $A = 2600[cm^2]$, $V = 5.1\ [l]$, $S = 3.3\ [\frac{l}{s}]$, $T = 295[K]$

3.4 Sticking of molecules on getter materials

Getter materials are actually the best solution to reach UHV conditions, transforming the wall of a vacuum system from a source of gas into a pumping surface. Getters are materials capable of chemically adsorbing gas molecules, the same process which occurs with adsorption of H_2O on metals the room temperature. In Figure 29 is showed the Lennard-Jones potential for the chemical and physical adsorption: chemisorption occurs in getter materials, implying formation of strong covalent, ionic or metallic bonds between gas molecules and the adsorbing surface, with binding energies much higher than 11 kcal/mol (energies comparable to the adsorption of water on metallic surfaces).

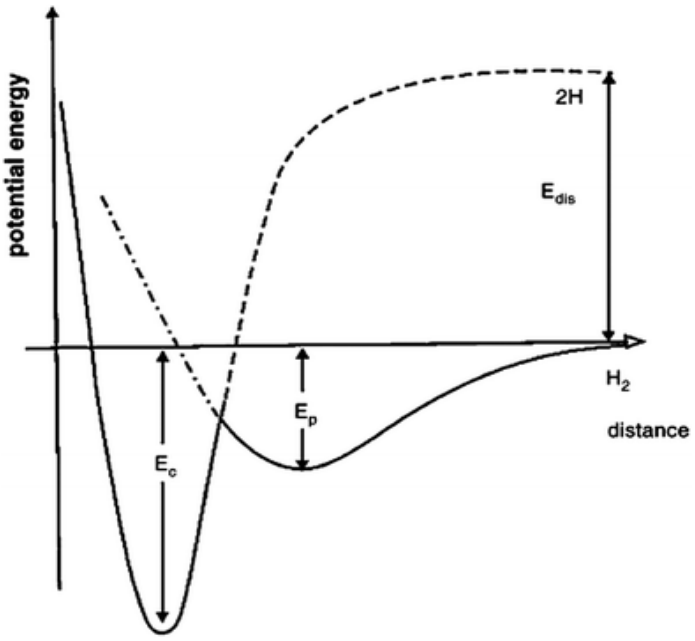

Figure 29: Lennard-Jones potential energy diagram for the adsorption of a molecular or dissociated generic species. The deeper well is related to the chemisorption phenomenon, the one interested by the getter physics.

A limit of this technology is to not form chemical bonding with noble gases, which are inert and therefore impossible to pump by the surface. Furthermore, such coatings provide a negligible pumping speed also for hydrocarbons, which are usually present in vacuum systems (particularly CH_4), due to their high dissociation energies at metal surfaces. However, heavy hydrocarbons can be adsorbed at the surface of a getter at room temperature by physisorption[4].

A getter surface is characterized by its sticking probability σ, namely the capture probability per molecular impingement. Recalling eq. 22:

$$S = A_p \, C \, \sigma$$

, the pumping speed of a getter material will be:

$$S = A_{getter} \, C \, \sigma \qquad \text{Eq. 67}$$

where A_{getter} is the geometric surface area of the getter material and σ depends on different variables, above all the nature the nature of the gas: the sticking probabilities of homonuclear diatomic molecules are in general lower than that of molecules composed of dissimilar atoms. The values of σ for common gas species in vacuum systems may be ordered in a growing series as follows:

$$N2 < H2 < O2 < H2O < CO < CO2$$

Moreover, $\sigma \propto \theta$: as the gas surface coverage increases, the sticking probability decreases (*saturation*). Therefore at the end the pumping becomes negligible when the surface is fully covered by gas molecules.

Finally, the surface roughness has also a strong impact on σ: a molecule will do several collisions on a rough surface, as an indirect increasing of the geometric surface area[5].

Getter materials can be of two types, according to the method followed to achieve activation:

- *evaporable getters* are obtained by under-vacuum sublimation and deposition of a fresh getter film on a metallic surface;

- the active surface of a *non-evaporable getter* (NEG) is obtained by thermal diffusion of the surface oxide layer, which contains absorbed gas molecules, into the bulk of the material itself.

At CERN, concerning the LHC project, this advantage has been obtained by ex situ sputter-coating the inner surface of vacuum chambers with non-evaporable getter films. By heating in vacuum (activation), the native oxide layer of such a film is dissolved into the bulk (thus "cleaning" the surface) allowing chemisorption of most of the gases present in vacuum systems at room temperature (Figure 30).

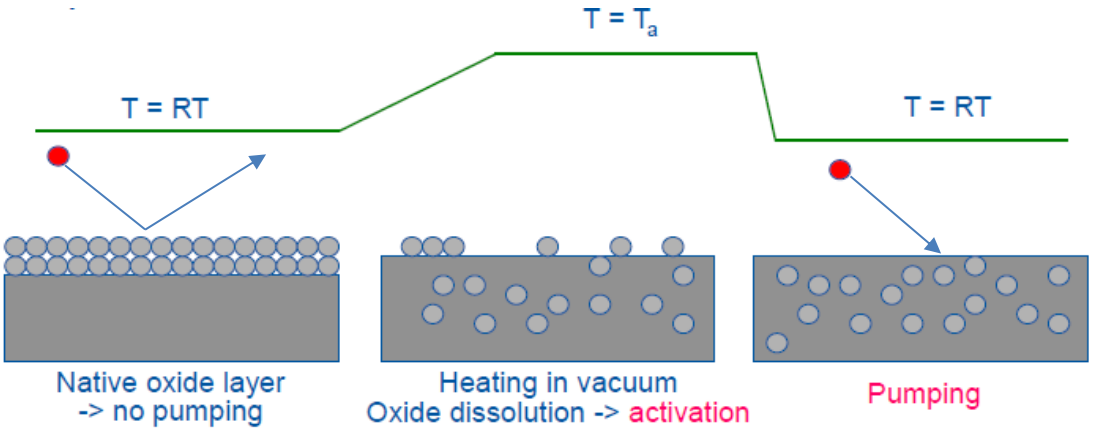

Figure 30: Activation and pumping process behind the working principle of a NEG surface. RT is the room temperature and T_a is the *activation temperature.*

3.4.1 Choice of the materials

The choice of the material to be used in order to provide a feasible NEG coating inside the vacuum chamber doesn't depend only on the chemical properties of his alloy components. There other important parameters to keep an eye on[29]:

- The activation temperature of the coating must be lower than the maximum temperature allowed for UHV vacuum chambers as reported in Table 3.2

Material	Maximum working T $[C]$
Stainless steel	400
Copper alloy	250
Alluminium alloy	200

Table 3.2: Maximum working temperatures for vacuum technology adopted materials.

- The oxygen solubility limit : the dissolution of O_2 is possible at such temperatures firstlyif the transfer of oxygen in the solid solution is thermodinamically possible

- The oxygen diffusivity in the film: dissolution of the aforementioned O_2 is definetively possible if the diffusion rate in the film is sufficiently fast.

With respect to the thermodynamic characteristic, the elements of the fourth group (Ti, Zr, Hf) were taken into account, since they show an exceptionally high ability to dissolve oxygen attaining values of concentrations up to 30 at.% (in the other chemical groups the solubility limit drops to values well below 1 at.%). Moreover, an enhanced diffusion can be achieved in the elements of the fourth group by adding other elements that either enlarge the lattice space (increased bulk diffusivity)[30] or reduce the grain size and, as a result, increase the transport of oxygen through the grain boundaries. This last approach was successfully verified for $Ti- Zr- V$ alloys. The activation of these films can be obtained by heating at 180° [C] for 24 h, which renders $Ti- Zr- V$ films compatible with all the substrate materials used in vacuum technology[31].

Figure 31[32] shows how measurements of the ultimate pressure and of the variation of the H_2 sticking coefficient confirmed this thesis,:

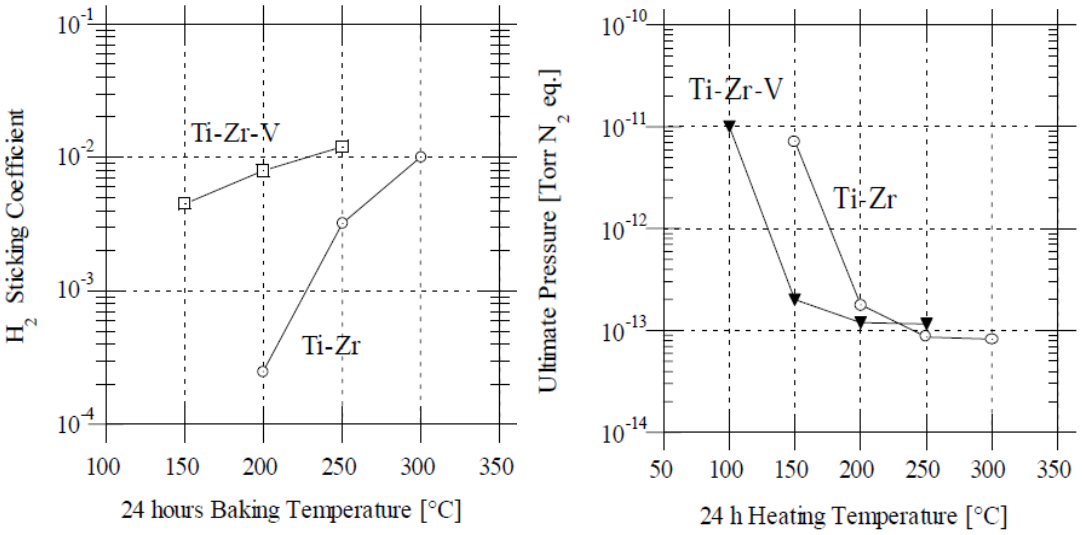

Figure 31: Variation of the H2 sticking coefficient for TiZr and TiZrV coated chambers as a function of baking temperature (left) and ultimate pressures without intermediate air venting (right), on chambers coated with TiZr and TiZrV. Characteristics: chamber length 2 m, diameter 10 cm, applied pumping speed 25 l/s for H_2.

3.4.2 Production of NEG coating

$Ti-Zr-V$ films are produced by magnetron sputtering and most of the know-how in the coating process comes from the experience acquired with thin-film Nb coating for superconducting RF cavities[33] [34]. The large domain of compositions where the dissolution is facilitated allows the production of simple and quite inexpensive cathodes for the coating of vacuum chambers: the three elemental wires are intertwisted to form a braid which is positioned along the tube axis for the coating process.

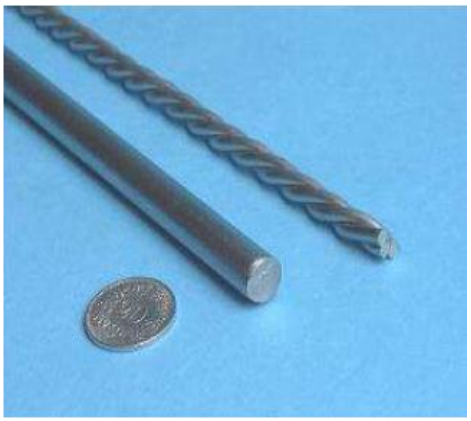

Figure 32: Twisted metallic wires (on the right) used as cathode in the NEG deposition process.

In this configuration the actual composition is $Ti\ 30-Zr\ 30-V\ 40$ at.% for 3 mm diameter wires. A key point for the success of this operation is the chemical treatment of the substrate materials before coating; in particular for the case of extruded copper tubes the cortical layer (about 50 Am) has to be chemically removed. An inadequate surface treatment leads to NEG film deterioration and, in the worst case, peel-off[29].

The dedicated facility at CERN consists of three cylindrical magnetron sputtering systems that allow coating vacuum chambers with a maximum length of about 7.5 m and maximum diameter of about 60 cm. Each unit consists of a vacuum pumping system, a manifold, a base support and a vertical solenoid as it possible to see in Figure 33:

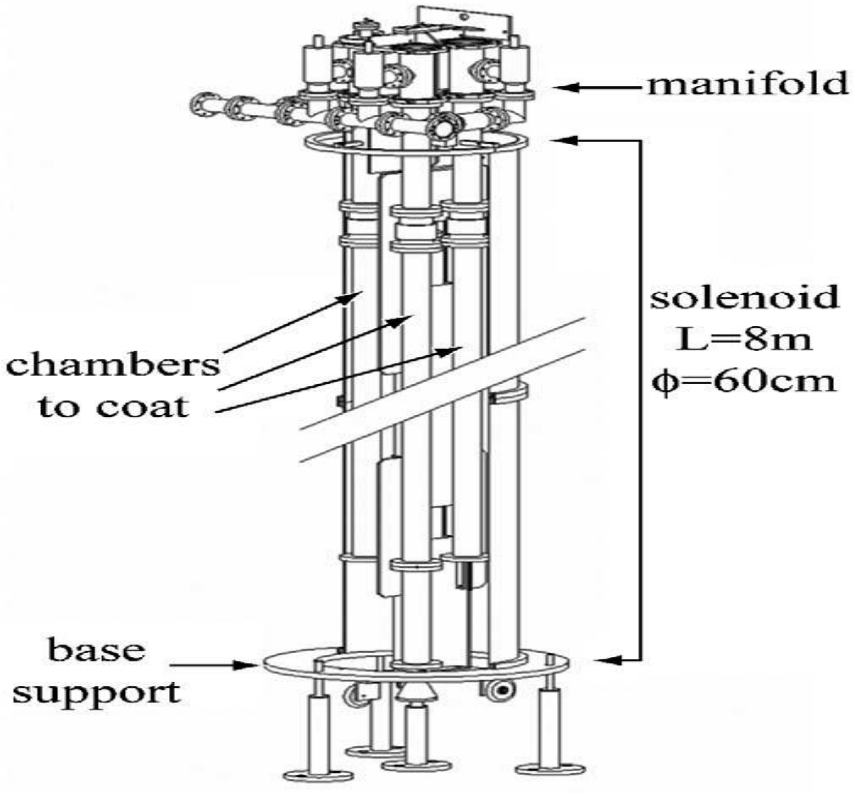

Figure 33: Drawing of the set-up used for the coating of the LHC-LSS vacuum chambers. Three such units are available at CERN [29]

In the simplest geometrical configuration, the three-wire cathode is inserted in the chamber and aligned along the pipe main axis. For more complicate structure, more than one cathode is necessary to guarantee uniform film thickness. The vacuum pumping system, equipped with a turbo-molecular pumping unit, cold cathode gauges and a RGA, is installed on a platform located at the top of the solenoid and is connected to the manifold by a bellow. The chambers are baked at 200^{o}C overnight before coating. During the coating process the chamber's temperature is kept at 100^{o}C. The discharge gas is Kr, which is injected at a pressure of about $10^{-2}\ Torr$. After coating, the chambers are dry air vented, dismounted from the cradle, pumped, filled with dry nitrogen at 1.2 bar and finally tightly stored.

CHAPTER 4

MEASUREMENTS AND RESULTS ON WATER STICKING COEFFICIENT

The experimental activity was conducted to the achievements of the following goal:

Calculate the Sticking Probability for water on unbaked metal chambers

The central point of the experiments consists in the choice of providing *water injections from outside* instead of recording pump down data after exposing the chamber to air. Isolating the chamber from the pumping group, is possible to observe only the pumping effect provided by the adsorption of H_2O on the surfaces. This not simple purpose, combined with the control of the tiny quantities of water injected, enabled in principle to extract true sticking factor data from the pressure evolution.

Assuming only an adsorbent behaviour in the first instants after the introduction of H_2O inside the test chamber, there were collected data of sticking probability in respect of quantity of gas injected (Q_{inj}), equilibrium pressures (p_{eq}) and chamber temperatures.

Finally it was made a comparison between the results and the analytical model, following the principles we have seen in section 3.2.

4.1 Set-up and choice of components

In order to reach this objective, the set-up has to fulfil the following requirements:

- Known the volume and surface of the experimental set-up;
- No other particle sink in the system than the walls (pumps, penning gauges, getter materials);
- Stable and reproducible system temperature;
- Fast data acquisition set-up;

Figure 34 presents an overview of the first assembly of the system:

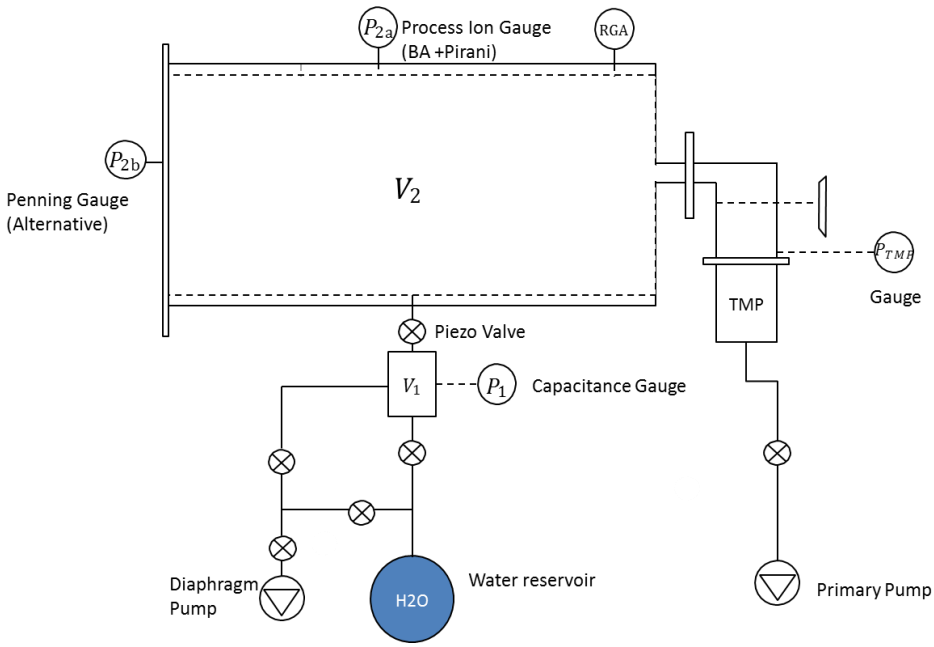

Figure 34: Schematic of the system installed in the lab.113 at CERN.

As it is possible to see in Figure 34, the test bench is divided in two “isolated” parts, the injection system and chamber in which was observed the water behaviour on the walls once injected. The characteristics of the system are reported in Table 4.1.

Characteristic of the system	Value
V_1	0.6 [L]
V_2	1st experiment = 20,3[L] 2nd experiment = 13.7[L]
$P_{V1} \quad inj$	32÷45 [mbar] (depending slightly on the Temperature of the ambient)
$P_{V2} \ after\ bakeout$	$5 * 10^{-10} \div 5 * 10^{-9}$(depending on the Temperature of the system)
T_{V1}	25°÷31° [C] (ΔT_{amb} during the months)
T_{V2}	$T_{amb} \ \div 100^0[C]$
A_{V2}	1st experiment = 5861[cm^2] 2nd experiment = 5957.25[cm^2]
$Capacitance\ gauge\ range$	$0 \div 1000\ [mbar]$
$Process\ ion\ gauge\ range$	$5 * 10^{-5}\ [mbar] \div 1\ [mbar]$
$S_{max}\ Diaphragm\ Pump$	$1\ [\frac{l}{s}]$

Table 4.1: Principal characteristics of the experimental test bench

A key role was played by the *piezo-electric valve* -PLV-1000®, Oxford Instruments- (**Errore. L'origine riferimento non è stata trovata.**), which was the link between the injection line and the test chamber. The valve is manufactured using only metallic components and the actuation is provided by means of an internal piezoelectric crystal stack: the application of an applied potential (ΔV) causes the expansion of crystals (*inverse piezo-electric effect*[35]), raising the central pull rod. This last is connected to a ceramic plunger, sealed (at $\Delta V = 0$) to the valve seat by a high tension spring. Thus, when a voltage is applied this plunger will raise, allowing the gas to flow through.

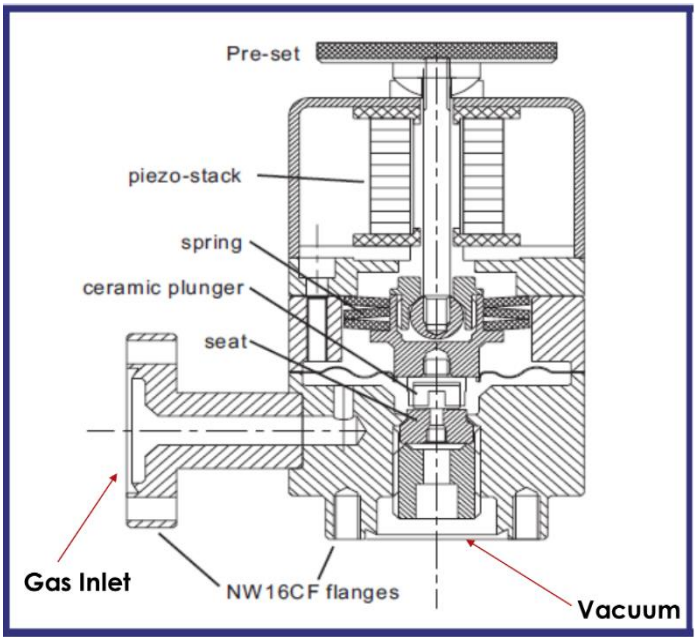

Figure 35: Schematic of the PLV-1000 piezo electric valve internal section

Using such a valve enabled to inject between $5 \cdot 10^{-7} \div 5 \cdot 10^{-2}\ mbar \cdot l$ of water vapour in short pulses (100÷1000 ms).

The length and the shape of the pulses are provided by means of a dedicated electronic set-up. Connecting a pulse generator to the piezo-valve controller is possible to send 0-1000 [V] pulses of the selected width, manually triggering the signal from the pulse generator.

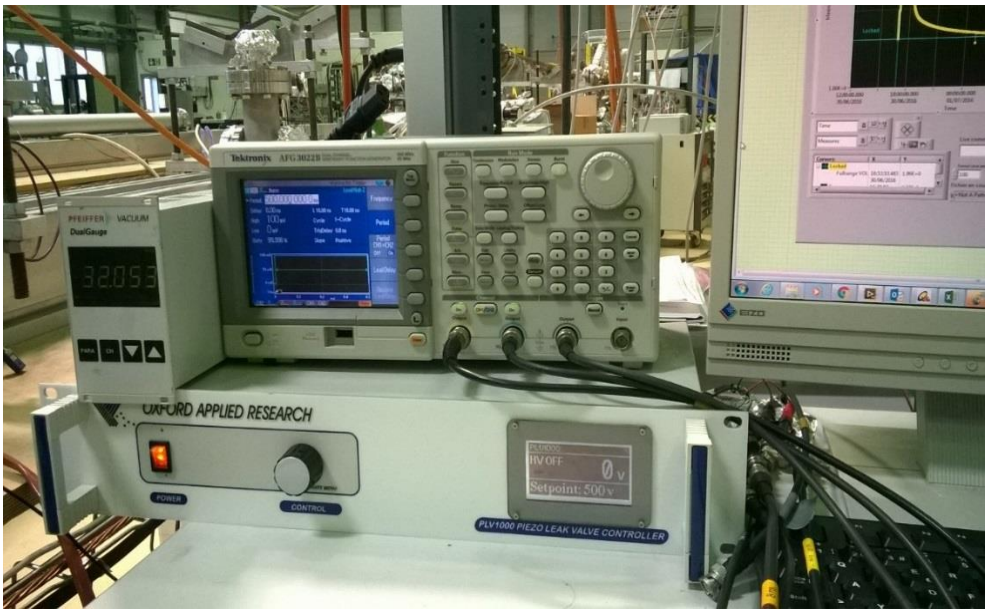

Figure 36: Control electronics apparatus

The operation of the valve has been characterized, finding a set of conditions which had the best reproducibility (in terms of quantity of gas injected) at the lowest time of injection. Different combinations of $applied\ voltage\ [V]/\ pulse\ width[ms]/\ pulse\ shape/\ setting\ torque\ [cNm]$ were tested, calculating the standard deviation of repetitive pulses. The optimum was found for square pulses of 400-500 $[ms]$ and $500\text{-}1000[V]$ of amplitude.

Finally, a fast 0-10[V] data acquisition, directly connected with the process-ion gauge controller has been used. The signals were sent to a DAQ USB module (USB-6128®, National Instruments) and processed by a dedicated LabView® program, being able to collect data up to 40 Hz.
Managing with applied voltage, initial torque of the valve and time/shape of pulses, it was possible to inject reproducible and measurable quantities of water vapour.

4.2 Injection system and purity of water

The water injection has followed this procedure:

- Use of demineralized water;
- Pump the reservoir until reaching the equilibrium between liquid and vapour phase: this will remove the other dissolve gases on the water;
- Fill the control volume with the vapour inside the water circuit just pumped;
- Empty the control volume until the final diaphragm pump pressure ($1mbar$);
- Repeat the process several times (flushing of the injection line);
- Check the purity of the water with the RGA.

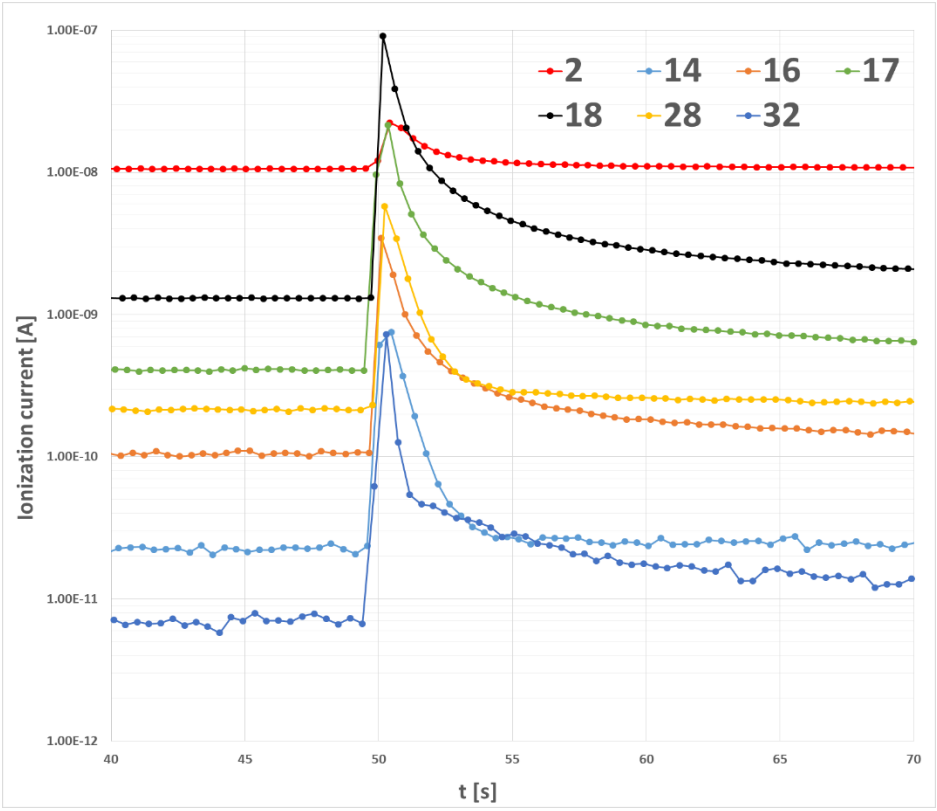

Figure 37: RGA analysis of water injection purity.

This procedure allowed to obtain 91÷94% purity of water. Figure 37 shows the evolution of different masses during one water injection (t=50 ms). The impurity gases (mainly N_2 and O_2) do not contribute to the dynamic behaviour and only introduce an offset to the equilibrium pressure.

4.3 Bake-out and water injections at room temperature

After assembly, the system has been equipped with thermal jackets, collars and resistance-strips surrounded by glass-fibre thermal insulator. Finally, thermocouples were connected in order to control the temperature.

As explained in 2.3.1, the bake-out consists of heating the vacuum chamber for a certain time in order to degas the adsorbed water.

Everything was connected to a mobile cabinet, which gave power and control the heating of each different part of the system. Figure 38 shows the bake-out equipment:

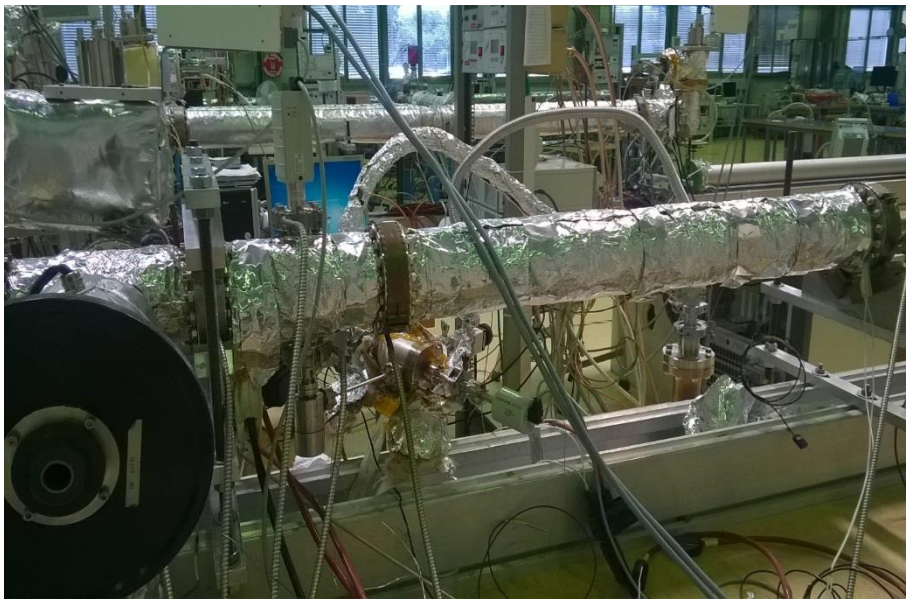

Figure 38: Bake-out equipped V_2 system.

Once verified the purity of the water, the following steps were performed:

1. Initial pump-down of V_2 until reaching $p_{V2} \approx 10^{-7}$ mbar;
2. Bake-out of the system at 150°C for 24 hours;
3. Cool down to T_{amb};
4. Closure of the pumping system valve, switch off penning gauge and injection of water vapour at a fixed temperature;
5. Pump-down of V_2 again until $p_{V2} < 10^{-7}$ mbar;
6. Bake out and repeat the process using another fixed temperature for V_2 ($30^{o}<T<100^{o}C$).

Heating at 120° C is considered enough to remove the molecules from the walls, so when the system is cooled down at room temperature, the chamber pressure is considered limited by hydrogen outgassing. To ensure repetitive initial conditions

before each measurement the system was baked at 150°C @24h. An example is shown in Figure 39.

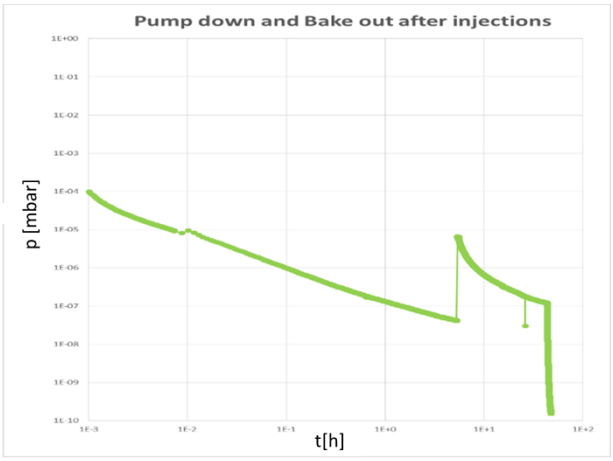

Figure 39: Bake-out at 150°C in V_2 chamber.

The valve used for the injections had a leak depending on the torque applied to the valve. These leak was considered during the injections: considering $35 < Tq < 55\ cNm$, the average leak was = $5 \cdot 10^{-9}\ \frac{mbar\ l}{s}$. This leak rate is negligible compared to the pressure reached already at the first injection. No drift is observed on the pressure once reached the equilibrium despite this leak on the duration of the experiment. Figure 40 shows the pressure evolution of injections performed at T_{amb}.

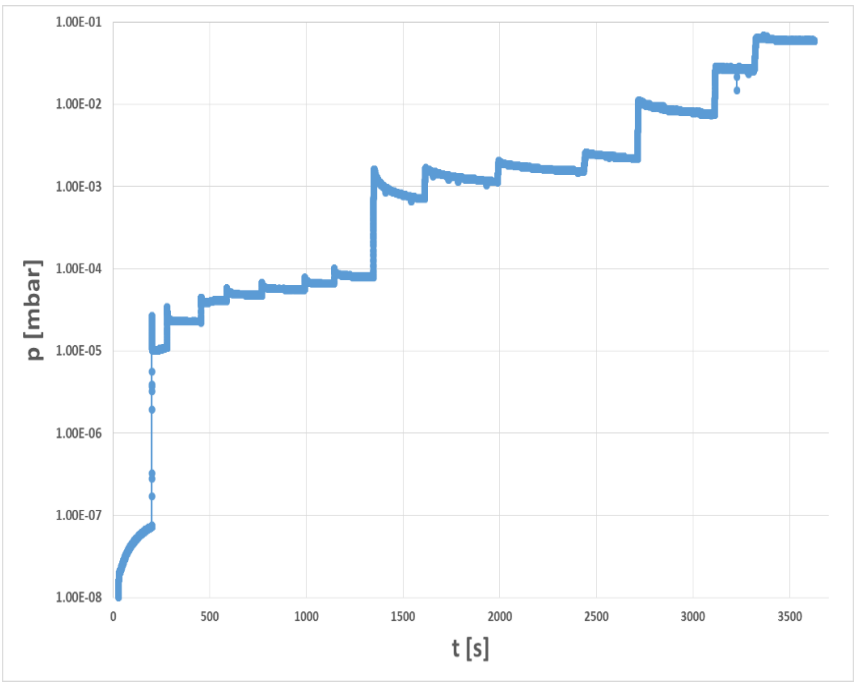

Figure 40: Pressure evolution for T_{amb} (27° C) water injections.

Just after the end of the water injection, pressure drops due to the pumping of the walls of the system. In absence of other pump the stainless steel walls are the only possible sink for the water molecules.

The pressure trend fits two different exponentials. The first is an exponential decay assuming negligible desorption from the vacuum chamber. The equilibrium is completely displaced to the gas phase. Under these assumptions the characteristic time of the exponential is the ratio of the pumping speed of the walls over the volume of the vacuum chamber. The second trend is instead as a sum of adsorption and desorption, reaching finally the equilibrium pressure.

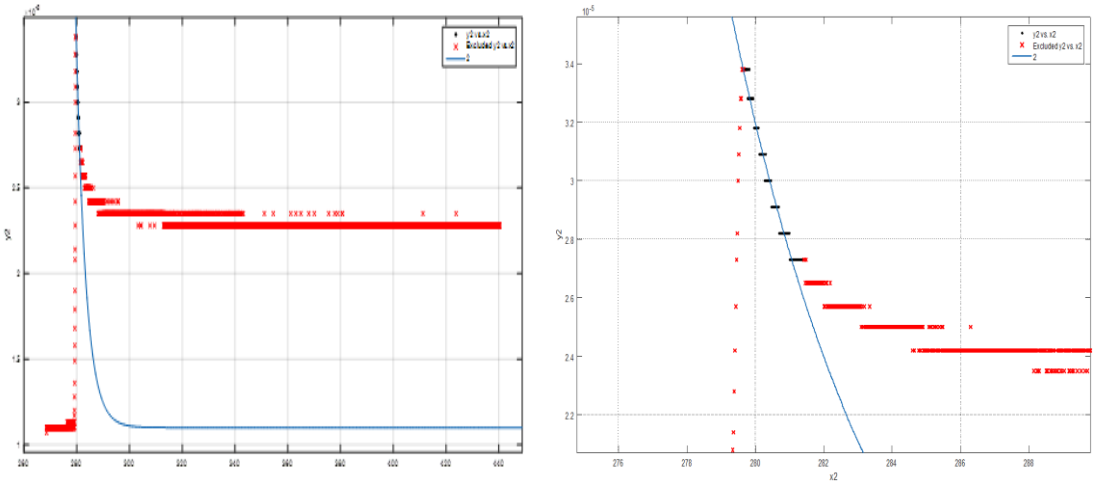

Figure 41: Single pulse analysis in Matlab ®. On the right is shown the fitting focused on the first 2 seconds after the 500ms injection.

Each pulse is fitted with an exponential:

$$p(t) = p_0 e^{(-t/\tau_p)} \qquad \text{Eq. 68}$$

And τ_p is the same pumping characteristic time seen in eq.29

Now, since:

$$S = \mathrm{V}/\tau_p$$

And, as shown in eq. 22:

$$S = \frac{1}{4}\bar{v} \cdot A_{metal\ surface} \cdot \mathrm{s} \qquad \text{Eq. 69}$$

Hence the sticking coefficient:

$$\mathrm{s} = \frac{4\mathrm{V}}{\bar{v} \cdot A_{metal\ surface} \cdot \tau_p} \qquad \text{Eq. 70}$$

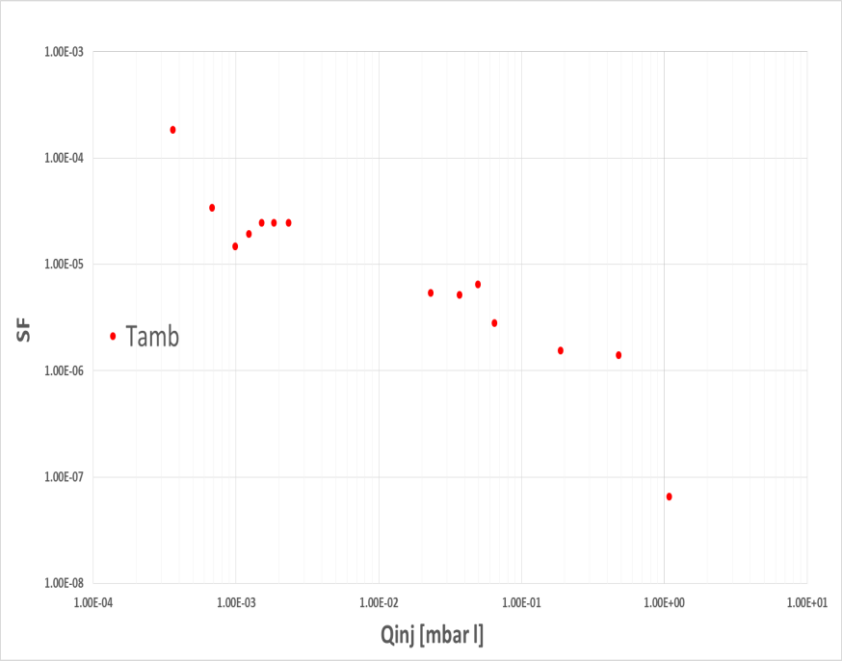

Figure 42: Sticking coefficient in respect of the equilibrium pressure inside V_1 at room temperature

Sticking factor of water at different coverage (room temperature) were calculated (see Table 4.2).

τ [s]	Volume [m^3]	S [m^3/s]	S [l/s]	Surface [m^2]	T [K]	Molecule Mass [kg]	SF
0.83682	1.37E-02	1.63E-02	16.33	0.595725	300	0.018	1.84E-04
4.545455		3.01E-03	3.01				3.40E-05
10.52632		1.30E-03	1.30				1.47E-05
8		1.71E-03	1.71				1.93E-05
6.25		2.19E-03	2.19				2.47E-05
6.25		2.19E-03	2.19				2.47E-05
6.25		2.19E-03	2.19				2.47E-05
28.62869		4.77E-04	0.48				5.39E-06
29.77963		4.59E-04	0.46				5.18E-06
23.9521		5.70E-04	0.57				6.45E-06
55.21811		2.47E-04	0.25				2.80E-06
100		1.37E-04	0.14				1.54E-06
110.2657		1.24E-04	0.12				1.40E-06
2360.718		5.79E-06	0.01				6.54E-08

Table 4.2: Calculations of SF and variables involved in $\boldsymbol{T_{amb}}$ water injections analysis.

The quantity of gas adsorbed Q_{ads} has been calculated as showed in equation 71 :

$$Q_{ads} = \left(p_{\max inj} - p_{equil}\right) \cdot V_2 \qquad \text{Eq. 71}$$

4.4 Water injections at different temperatures

The installed bake-out equipment allowed warming the system to a fixed temperature during the measurement. Since the room temperature was not controlled in measurement lab, this contributed to be sure of the V_2 temperature and to evaluate any possible relation with the temperature itself.

Using again the same eq. 70, the sticking probability at different temperatures is shown on Figure 43.

For the first injections there are no evident differences between different temperatures and even the SF has an almost flat trend, varying between 10^{-4} *and* 10^{-5}. Going forward, is possible to notice the aforementioned collapse in correspondence of the monolayer coverage.

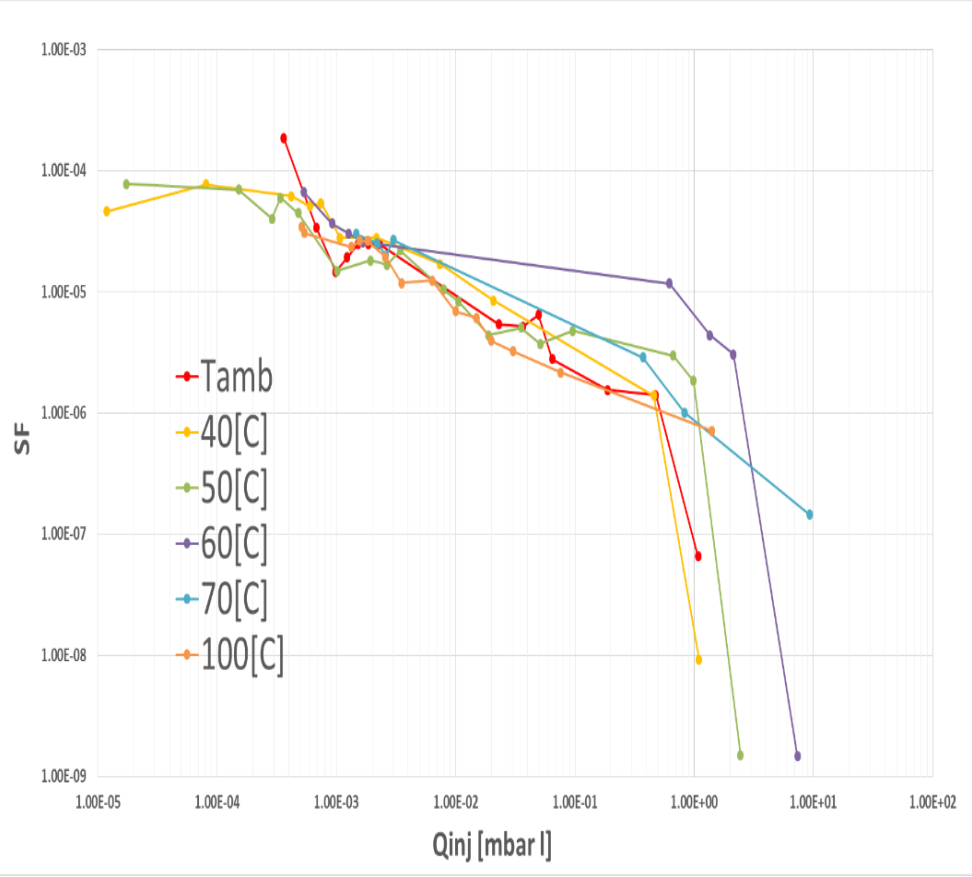

Figure 43: $P_{equilibrium}$ vs. Quantity of gas injected in $V1$.

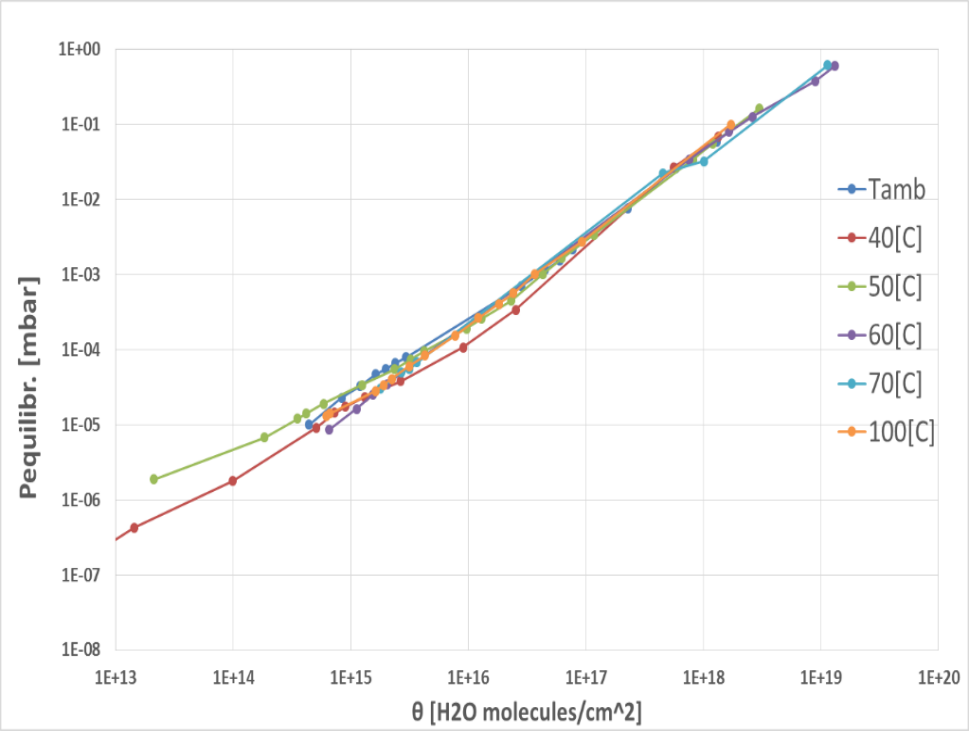

Figure 44: Adsorption isotherms for H_2O on 316 stainless steel.

Another important result of these experimental campaigns is the measurement, at constant temperatures, of the vapour equilibrium pressure (Figure 44) as a function of the surface coverage.

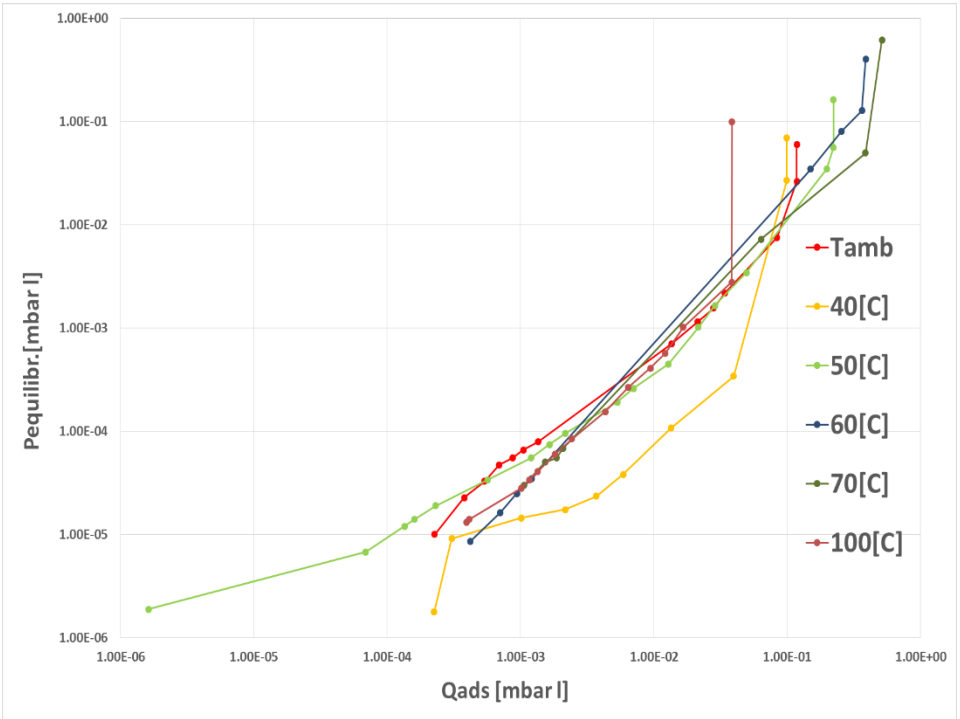

Figure 45: Equilibrium pressure vs quantity of water adsorbed by stainless steel surface.

As we have seen in section 3.3, these represent the *adsorption isotherms.* The adsorption isotherm is function of the molecular species, the temperature of the surface, the nature of the surface and the gas composition. In Figure 43 and in Figure 44 is possible to notice almost no differences for different temperatures for $p < p_{sat}$.

4.4.1 Test injections with Neon

To exclude the pressure evolution was an artefact on the experimental set-up one test injecting Ne with the same procedure has been carried out. Noble gasses are inert, so the sticking probability is zero at room temperature: a pressure decrease after the fast injections is not expected as in the case of water.

At a temperature of 40°C, Ne 99% has been injected. Figure 46 and Figure 47 show the results:

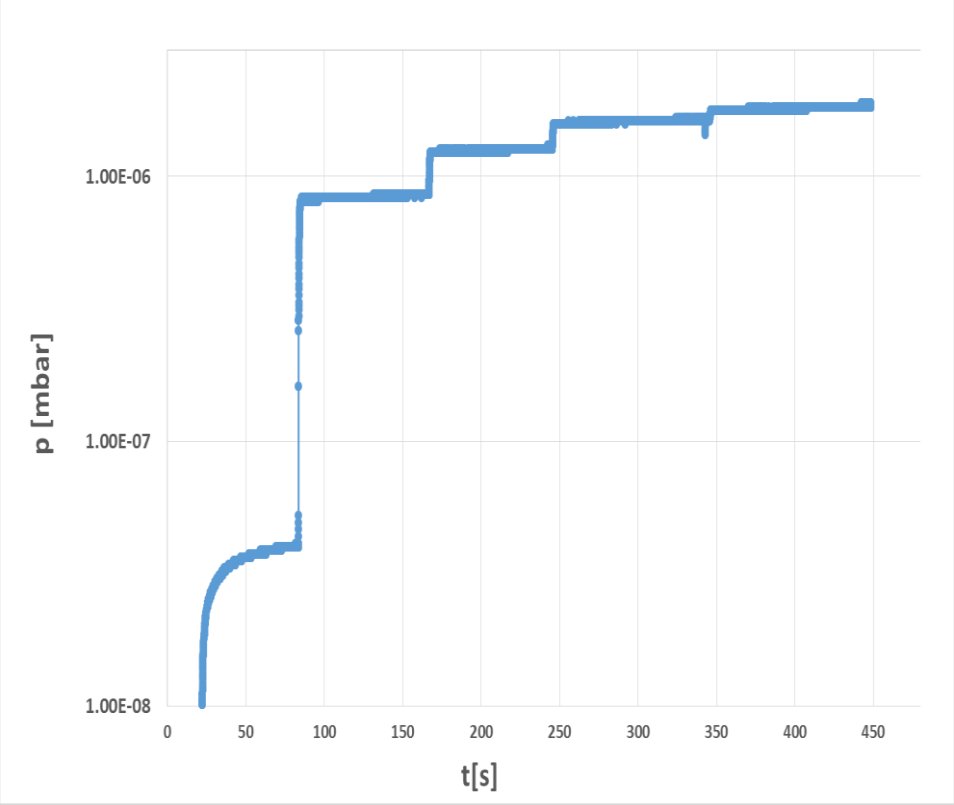

Figure 46: Neon injections at $T_{V_2} = 40$°C

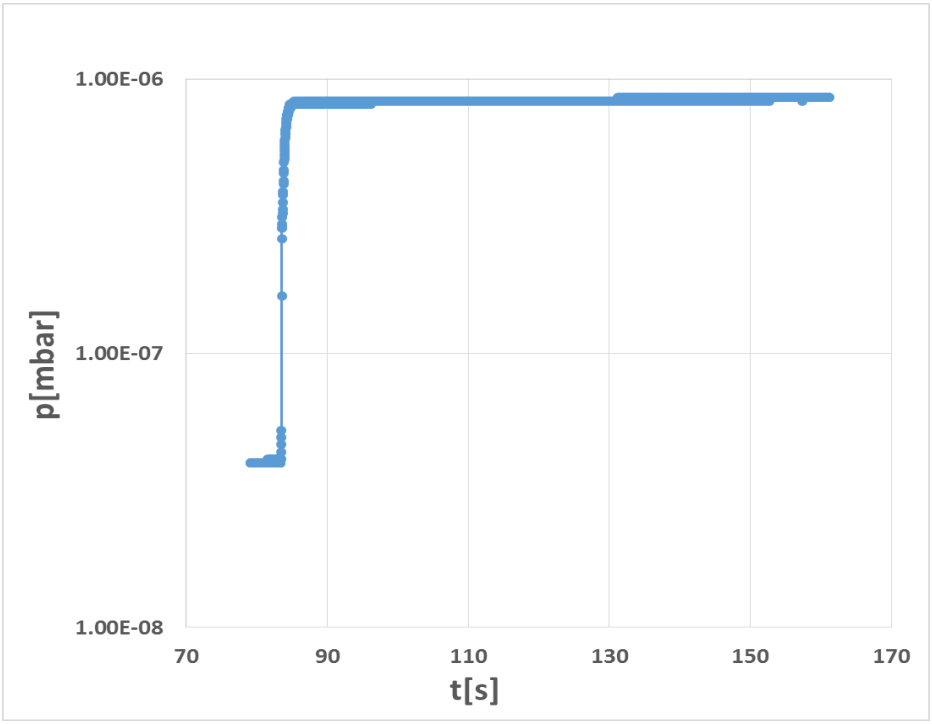

Figure 47: Neon injection single pulse analysis

During Ne injections the pressure is stable just after the closure of the fast valve, without any observed transitory. This evidence excluded any possible artefacts of the set-up leading to fake results.

CHAPTER 5
NON EVAPORABLE GETTERS (NEG)
ACCEPTANCE TEST IMPROVEMENT

As already pointed out in CHAPTER 3, NEG coatings are widely used in accelerator technology. Like any other components to be installed in a vacuum system, these NEG coated chambers need to be tested before installation.
For this reason there are been developed procedures to accept this chamber which involve different steps to be followed in the lab. The reference lab at CERN is building 113.

5.1 Procedure for the acceptance of NEG vacuum chambers

The system used for the tests of NEG coated beam pipes should have the following components (see Figure 48):

- NEG chamber;
- Fischer-Mommsen type Dome[36](with ionization gauges for pressure measurements SVT_i and a known conductance);
- Injection line for H_2, N_2 and CO at SVT_1 side
- SVT_3 gauge at the end of the pipe;
- Turbo molecular pumping group and roughing pumping station;
- Residual gas analyser (RGA) at SVT_2 side.

The dome is pumped using a turbopump. An ion pump during the injection tests would show a variable pumping speed and selective pumping for different gases. A sublimation pump, during the injection tests would be a selective pump and during the degassing process could produce a high concentration H_2 that could easily diffuse inside the NEG coating. For all these reasons the use of ion pumps and/or sublimation pumps should be avoided at any stage[37]. Figure 48 shows a schematic of the test bench. For the realization of this thesis it was included on this test bench a second RGA (RGA_2) ant the end of the beam pipe.

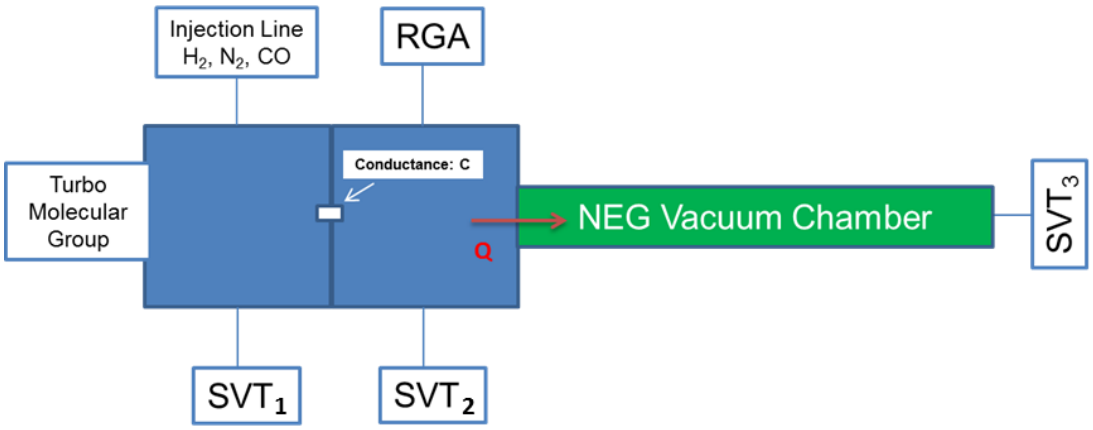

Figure 48: Experimental test bench configuration and components.

RGA_2 allows us to analyse the partial pressure of the gas coming at the end of the system allowing better evaluations of the performances of the NEG coating.

After fitting the NEG chamber to the measuring dome 24 hours of pump down and leak detection, the system should be baked. This bake-out is used to evacuate the H_2O molecules and activate the getter. Figure 49 shows an example of pressure decrease after reaching the activation temperature, 180˚÷200˚[C]. Then, the performance of the NEG coating should be verified after at least 24h at room temperature.

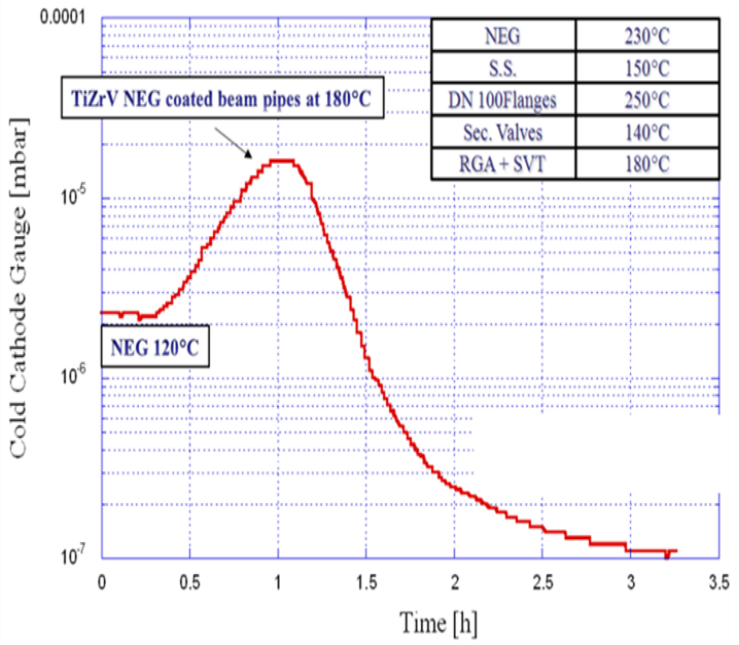

Figure 49: Pressure decrease after NEG activation.

The measurement is carried out injecting H_2, N_2 and CO. This order is important to avoid the saturation of the coating. The injections are performed used a variable leak manual valve. Typical pressures during injection are $\approx 1 \cdot 10^{-7}$ mbar for H_2 and $\approx 5 \cdot 10^{-9}$ mbar for N_2 and for the CO measured both at SVT_2. An example of a H_2 injection on a NEG chamber is shown in Figure 50. The ratio between SVT_2 and SVT_3 is known as transmision ratio and gives an indication of the activation of the NEG coating.

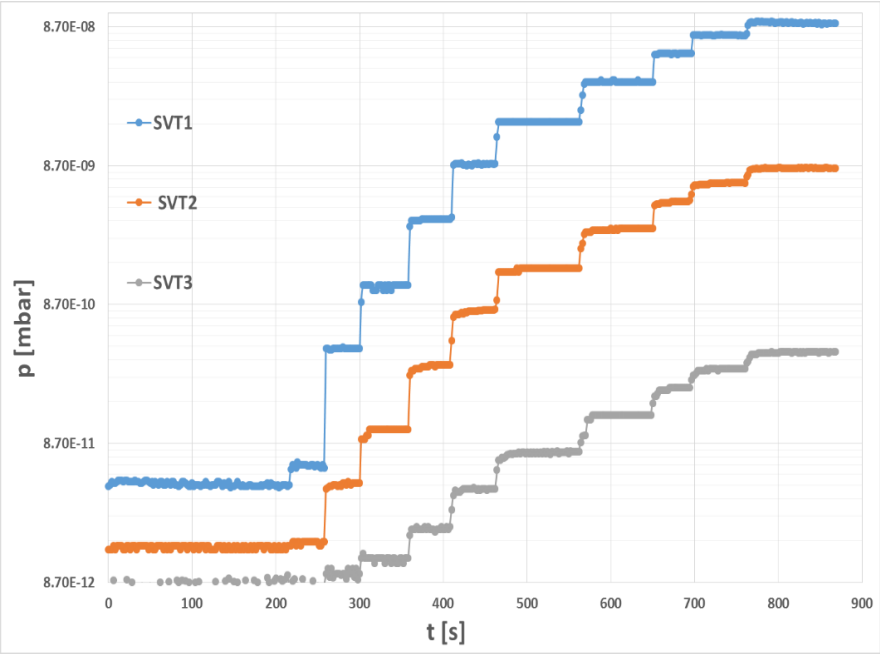

Figure 50: *Pressure steps during a H_2 injection. The three lines refer to the three SVTs mounted on the system*

The parameters that should be determined during these injections are:

a) *Cleanliness* and non-contamination of the NEG beam pipe by taking a final scan of the system with the RGA.

b) *Pumping speed* of the aperture of the tube. Using following formula:

$$S_{NEG\ aperture} = \frac{\mathrm{Q}}{\Delta P_{SVT2}} = \mathrm{C} \cdot \left(\frac{\Delta P_{SVT2}}{\Delta P_{SVT1}} - 1\right) \qquad \text{Eq. 72}$$

c) *Transmission* ratio (TR) given by the ratio of SVT_2 and SVT_3

$$Transm = \frac{\Delta P_{SVT2}}{\Delta P_{SVT3}} \qquad \text{Eq. 73}$$

d) *Sticking coefficient* derived from a TMPC simulation that correlates the sticking with the transmission ratio (Figure 51).

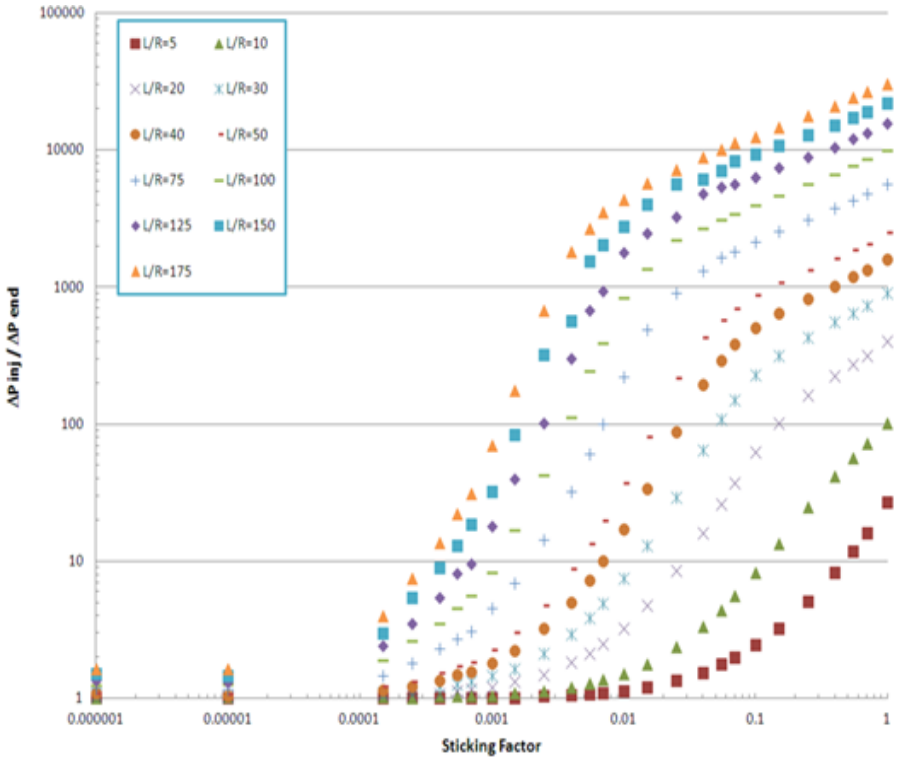

Figure 51: ***Sticking coefficient as a function of the transmission ratio for different dimension of the NEG vacuum chambers. R= radius – L=Length*****. This is the reference chart for NEG acceptance tests at CERN**

This last graph results to be a user-friendly tool: using the TR calculated experimentally, the sticking coefficient for the specific gas injected is extracted on the respective x-axis coordinate.

e) *Ultimate pressure* in the SVT_3 after 24 hours of cooling down and after having performed a modulation of 20 minutes.

At the end all the informations are collected in a final report.

5.2 Procedure upgrade: measurements and results

5.2.1 Experimental set-up and first measurements

The experimental set-up is shown in Figure 52.

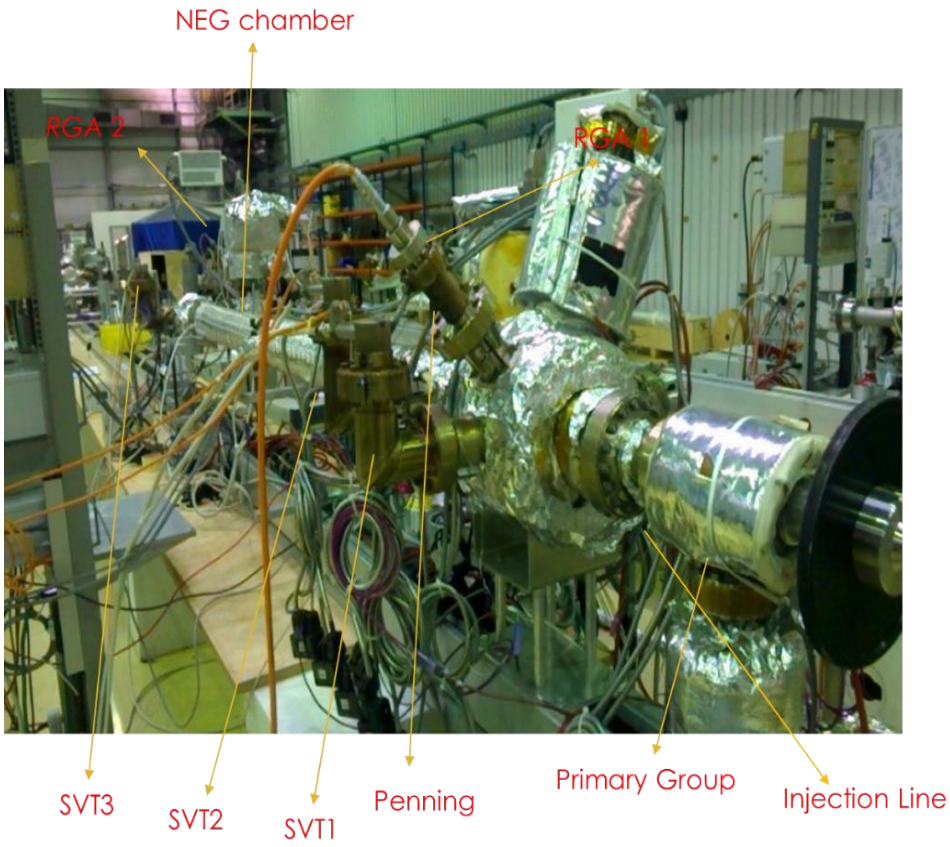

Figure 52: NEG acceptance test 1st experimental test bench in lab. 113 at CERN.

As described on the procedure, a 24h pump-down and a bake out cycle with NEG activation have been carried out. Figure 53 shows the results.

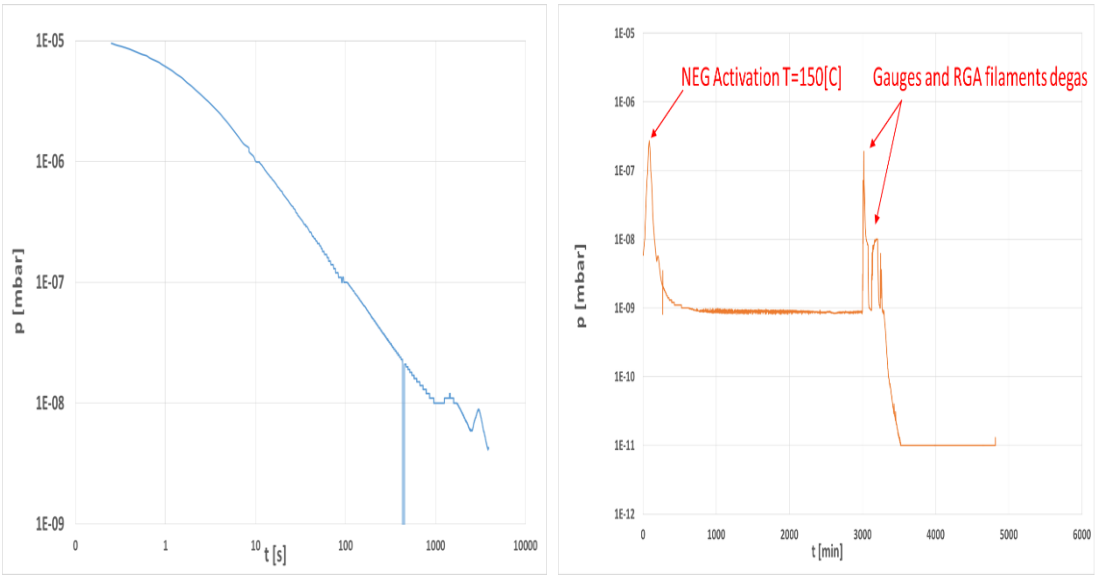

Figure 53:Pump down and Bake-out cycle curve on a 1560mm length NEG chamber system.

After the bake-out the gas injection were carried out. In Figure 54 is shown an N_2 injection, followed by an RGA analysis.

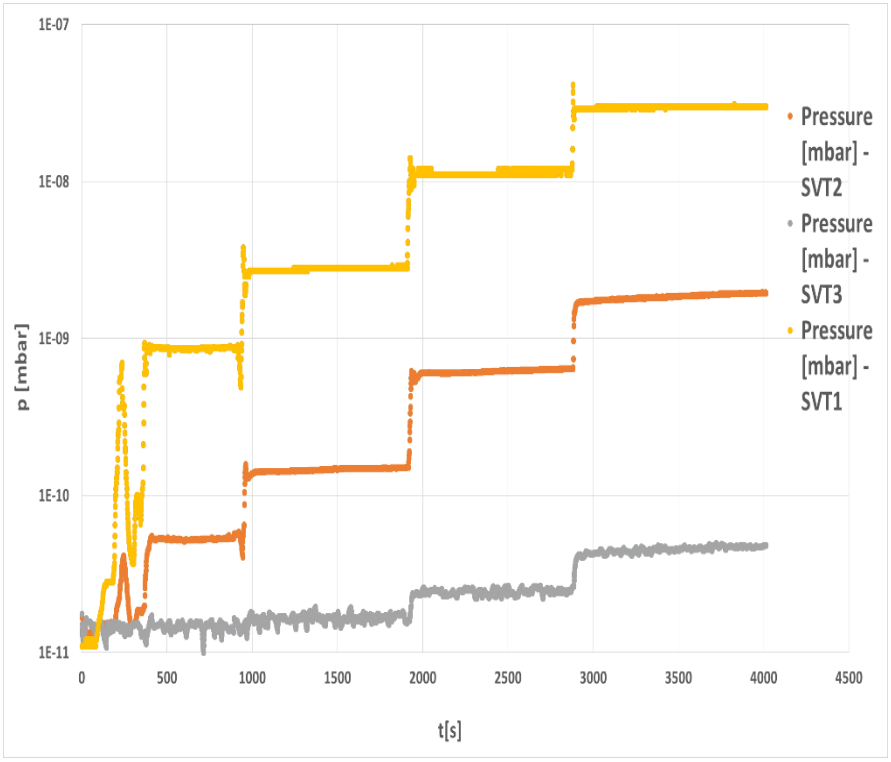

Figure 54: N_2 injection steps

Figure 55 shows the gas composition measured on RGA_1 and RGA_2 during the injection. It's clearly visible that a $p_{end\ injection} \approx 10^{-9}\ mbar$ at the end of the chamber allow us to well see the N_2 as the dominant gas, so that to determine his SF.

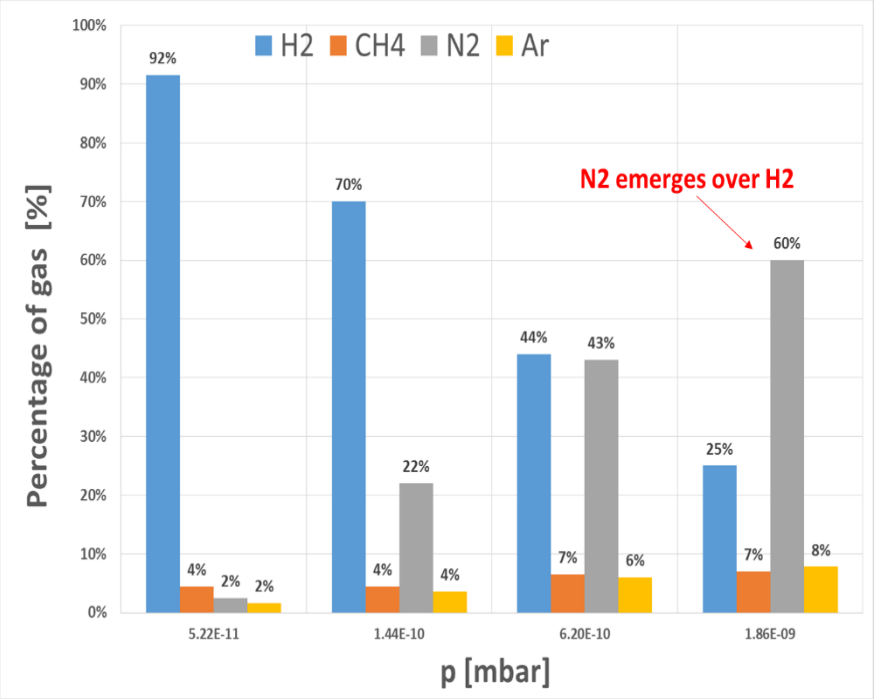

Figure 55: Gas % vs. injected pressure at the NEG entrance RGA analysis for N_2 injection.

During the CO injection it was necessary to increase the pressure at the entrance of the NEG chamber at least to $10^{-7}\ mbar$ in order to evaluate a TR ratio.

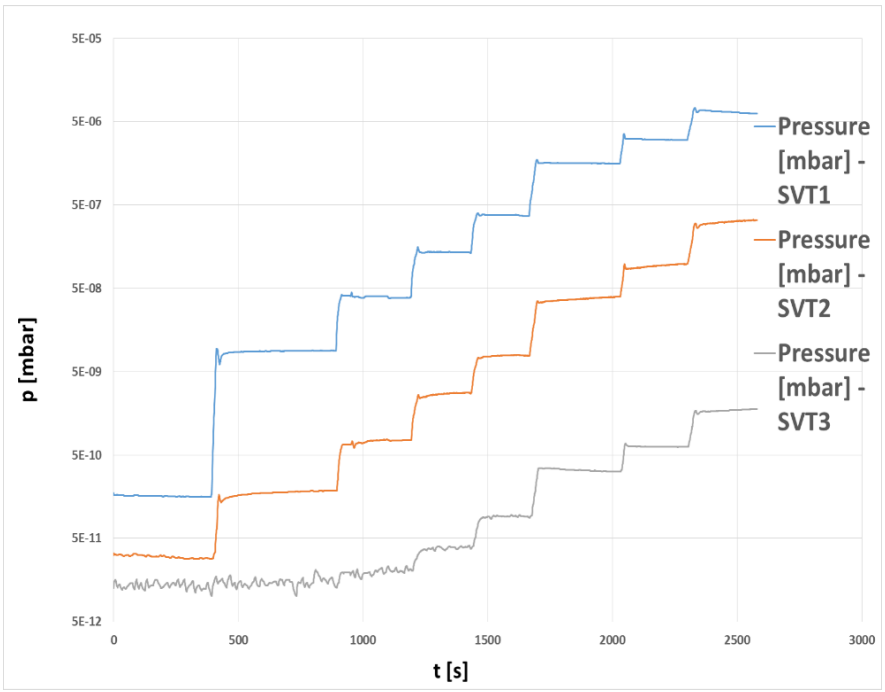

Figure 56: CO injection steps.

This high pressure is required to get enough CO at the end of the vacuum chamber, because of the high sticking factor of CO.

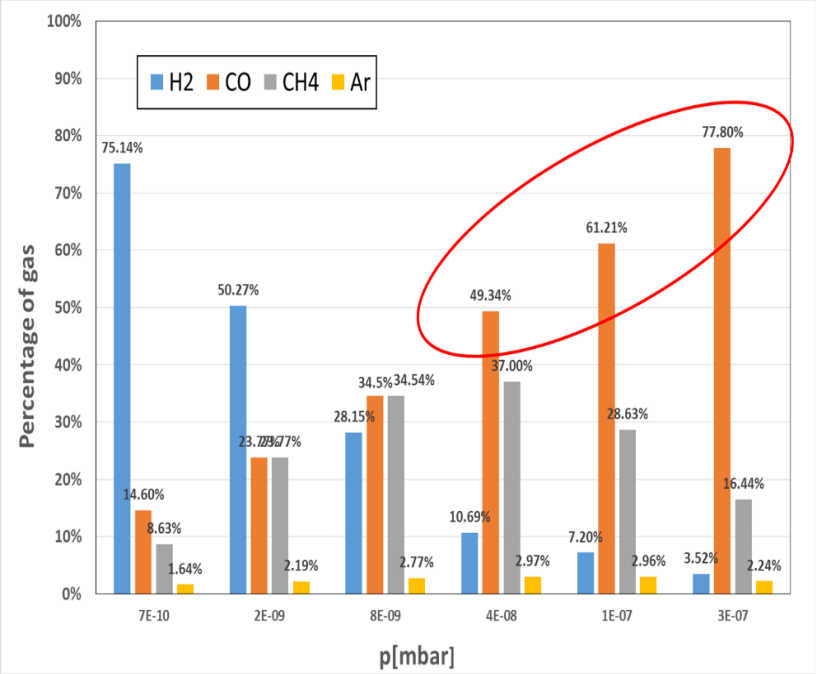

Figure 57: Gas % vs. injected pressure at the NEG entrance RGA analysis for CO injection.

The final results of the three injections are presented in Table 5.1.

Gas	$S_{NEG\ ap.}$ [l/s]	TR
H_2	200	30
N_2	124	70
CO	308	282

Table 5.1: Values of pumping speed (S) and transmission ratio(TR) carried out after injections.

Using the transmission data for the three gasses it is possible to obtain the SF as indicated in Figure 58.

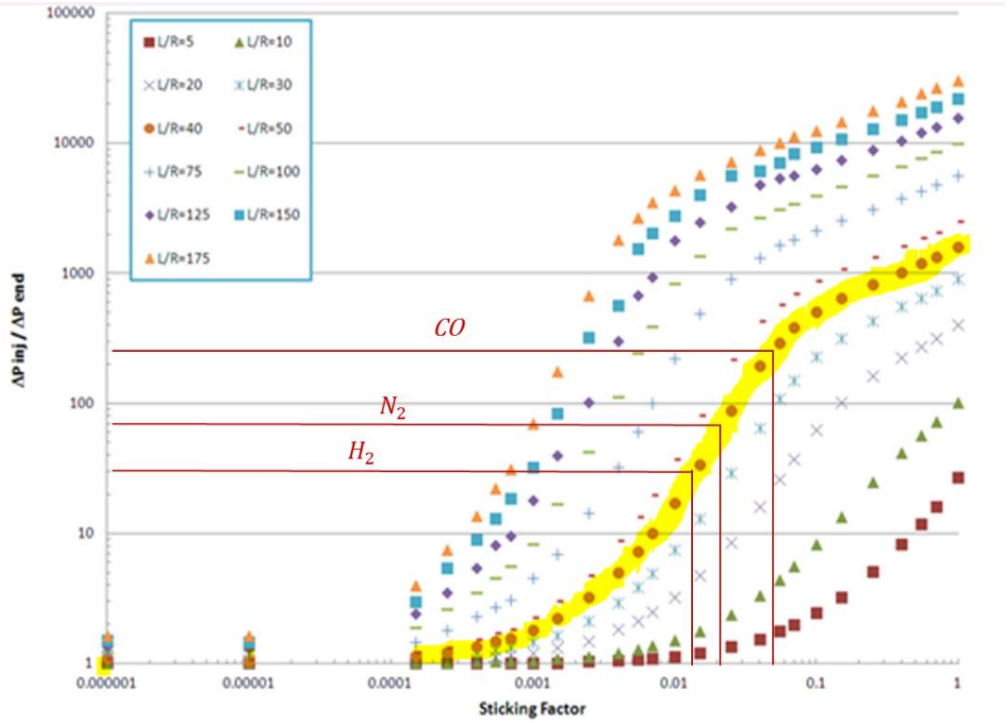

Figure 58: Experimental results after injections analysis for the L/R=40 NEG chamber.

By means of the aforementioned chart, we calculate SF≈ 0.02 for H_2, SF≈0.03 for N_2 and SF≈0.055 for CO.

According to what is found in literature[38], the sticking probabilities for NEG coatings are:

H_2	1x10-3 < SF(H_2)<5x10^{-2}
N_2	SF(N_2) >1.5x10^{-2}
CO	SF(CO) > 7x10^{-2}

Table 5.2: Sticking probability accepted for acceptance criteria at CERN.

The SF of CO is lower than expected. At his first analysis the chamber seems to be not sufficiently performing and thus to be discarded. Before any further analysis it is important to highlight some aspect of the test bench and simulations:

- Hot cathode gauges and RGAs are devices foreseen to work at pressure below $5 \cdot 10^{-8}$mbar. Whereas, injecting CO in the $1 \cdot 10^{-7} \div 1 \cdot 10^{-6}\ mbar$ range, could introduce side effects and damage the device (see section 2.4)

- The amounts of gas injected are not the "true" gas loads present in LHC. The higher outgassing rate in LHC is in the *collimators,* where we have $\approx \mathbf{1} \cdot \mathbf{10^{-8}} \boldsymbol{mbar\ l/s}$ [39] , whereas the acceptance test amounts to $\approx \mathbf{5} \cdot \mathbf{10^{-5}} \boldsymbol{mbar\ l/s}$: the coverage factors θ reached in lab tests are indeed achieved in years of machine work in LHC.
- Simulations performed in order to carry out the TR vs SF charts are strongly dependant both on the boundary conditions of the chamber and the choice of the *reflection model* used to simulate the molecular flow.
- Dynamic saturation effects on the NEG during the injection are not taken into account.

5.2.2 Simulations: choice of the model and boundary conditions

As we saw in section 2.5.1, using MOLFLOW+ one of the most important parameter is the choice of the *particle reflection model* to be used.

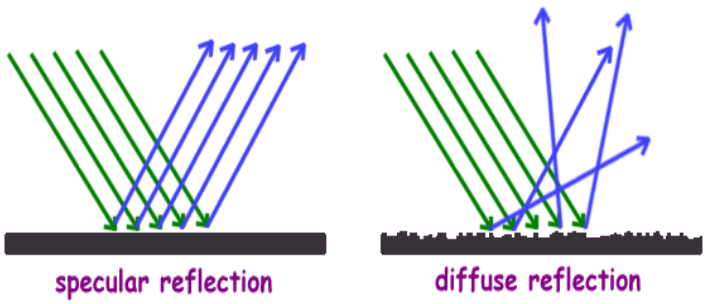

Figure 59: Reflection models behaviour comparison.

There have been performed several simulations in order compare both reflection models, between the diffusive and the specular one. This different behaviour has been explained in section 2.5.1 .

Selecting one of the two different models results change, giving different TRs due to different probabilities of the molecules to go forward or backward.

Figure 60 shows the gap between the two trends: this is due to the opportunity to have a component of the momentum in the backward direction in the diffusive

reflection. In this case, there will be more molecules recorded at the entrance of the chamber than in the specular case, thus a higher TR ratio (Figure 59).

The more convergent scenario seemed to be the diffusive one: for this reason, the rest of calculation in this chapter will be based on the assumption of this model

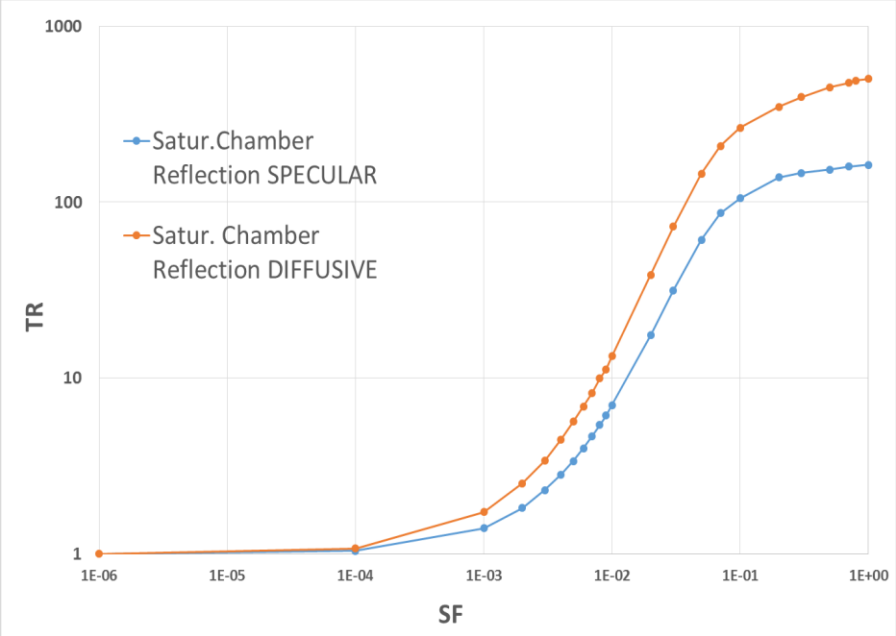

Figure 60: Differences on the TR calculation between diffusive and reflective models in a saturated NEG chamber.

Concerning the boundary conditions, there is also a big change in the evaluation of the sticking probability performances of the NEG. The procedure considered at CERN took in account a "semi-open system", which means considering a *completely adsorbent* facet at the beginning and a *completely reflective* one at the end of the cylindrical NEG chamber as we are talking about (Figure 61).

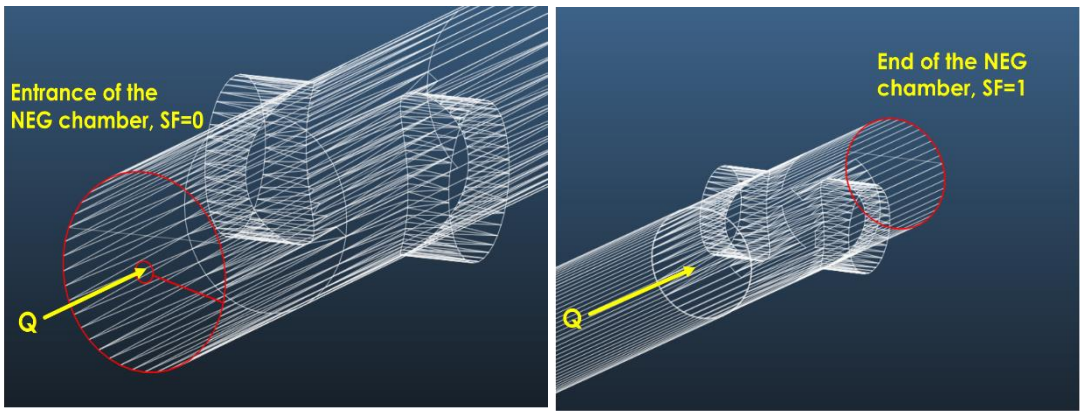

Figure 61: Boundary conditions in MOLFLOW+ simulation of the 1590[mm] length NEG test

This situation is not the most correct. A SF=1 at the end would be more possible in the accelerator operational case, where gas load particles are following their paths without encountering caps as the terminal flange of the experimental bench in the lab. In the scenario in which we are moving, the most correct boundary condition is to consider a SF=0 at the end of the chamber, since all of the arriving particles are back-scattered. Concerning instead the entrance putting 0 or 1 for the SF is, as is possible to appreciate in Figure 62, basically the same. The orifice of the entrance is so small that there is a poor possibility for the particles to scatter on the walls and to be then re-adsorbed back in the orifice.

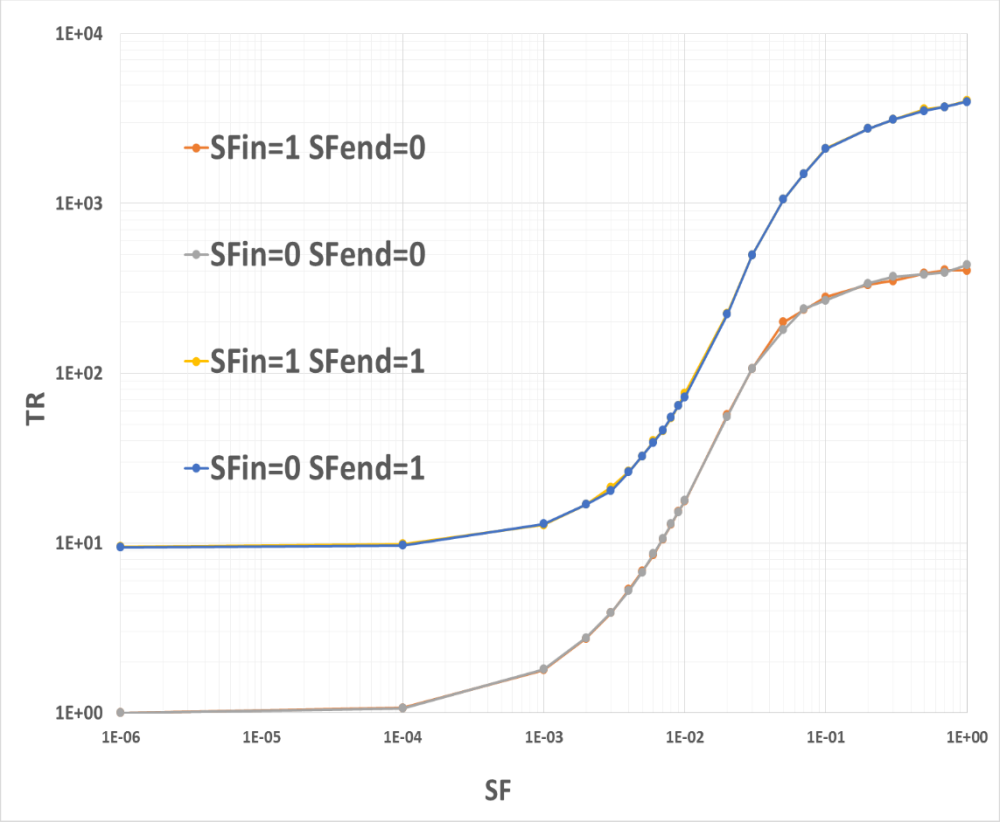

Figure 62: Differences on the TR calculation between various boundary conditions combinations. The L/R ratio is 40 per each simulation.

For these reasons, it has been chosen to use the SFin=1 / SFend=0 boundaries scenario for all the rest of simulations performed. In Figure 63 there is another overview of how is possible to control each parameter on the interesting facets in

MOLFLOW: pressure profiles, number of hits, possible leaks, adsorbent/desorbent properties of the facets.

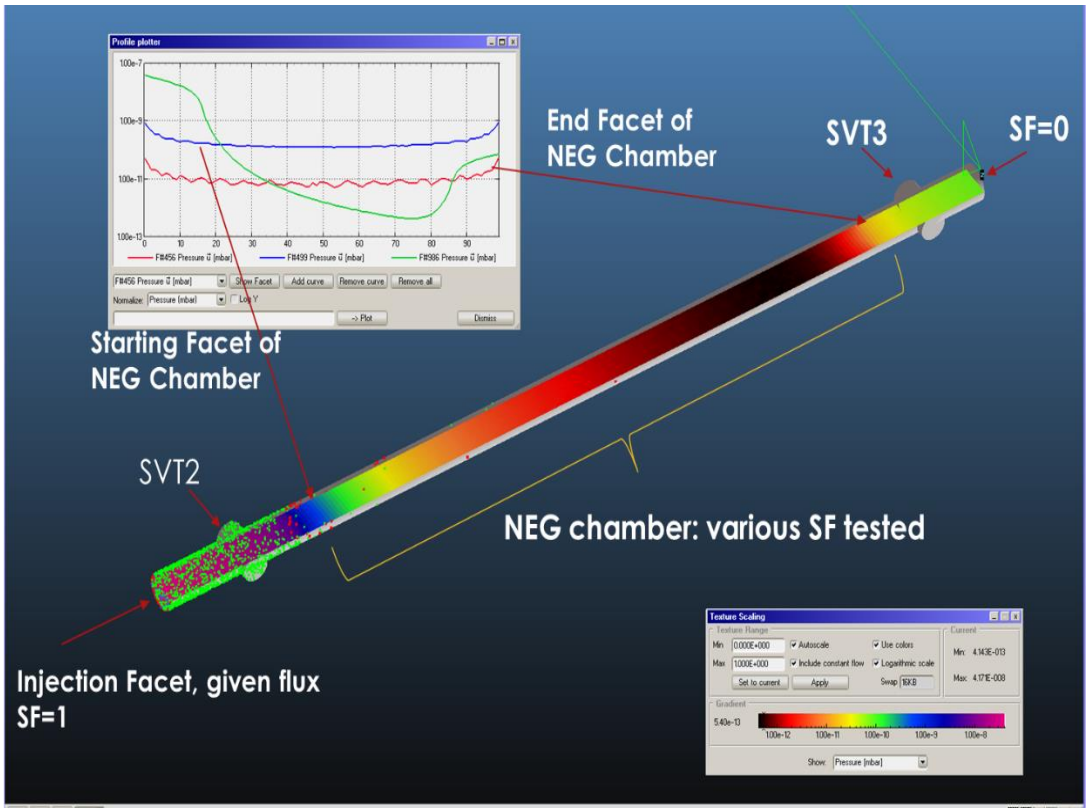

Figure 63: MOLFLOW+ running simulation of the 1590[mm] NEG chamber for different SF tested.

5.2.3 NEG chamber dynamic saturation

As it was mentioned, one of the most difficult phenomena to understand and simulate behind these experiments is the dynamical changing of the NEG adsorption properties *during* the injections. Is important to know that the NEG surface adsorbent capacity for CO is [29]:

- Smooth surface : $8 \cdot 10^{14}\ [\frac{molecules}{cm^2}]$
- Rough surface : $8 \cdot 10^{15}\ [\frac{molecules}{cm^2}]$

Thus, considering that during the CO injection about ≈ $6 \cdot 10^{17}$ $molecules$ of CO were injected, that results on a smooth surface about ≈ 1000 cm^2 of NEG surface saturated by CO molecules. This means ≈ 400 mm length of a cylindrical NEG coated chamber with a diameter of 80 mm.

It is no possible to simulate dynamic physical changes of the mesh elements in MOLFLOW, it has been used COMSOL® to reproduce this behaviour. Figure 64 shows the mesh used for the COMSOL simulation: in the coated part about 1 $cm^2/element$ distribution of the facets was built, so as to control "element per element" the number of the adsorbed molecules.

Figure 64: Mesh composition in COMSOL dynamic saturation simulations. It is possible to notice the difference between the square-mapped meshing on the NEG surface and the not structured triangular one on the remaining parts.

To simulate the transition from a certain sticking factor to zero when the NEG coating is saturated it was necessary to prepare a model with smooth transition and derivative. This was useful to have a fast convergence.

Equation 74 shows the model and Figure 65 shows the trend of saturation model:

$$\mathrm{SF} = SFco * \frac{1 - tanh\left(\alpha * \frac{(Mol.\ ads\ - NEG\ capacity)}{NEG\ capacity}\right)}{2} \qquad \text{Eq. 74}$$

where $SFco$ is the typical SF assumed for CO on NEG surfaces $\geq 7 \cdot 10^{-2}$, $Mol\ ads$ are the moles adsorbed on the single NEG mesh element $\left[\frac{mol}{cm^2}\right]$ and the $NEGcapacity$ is the adsorbent capacity seen before for smooth surfaces expressed in $\left[\frac{mol}{cm^2}\right]$. Finally, α is a *tuning parameter,* which defines the slope of the decrease to 0.

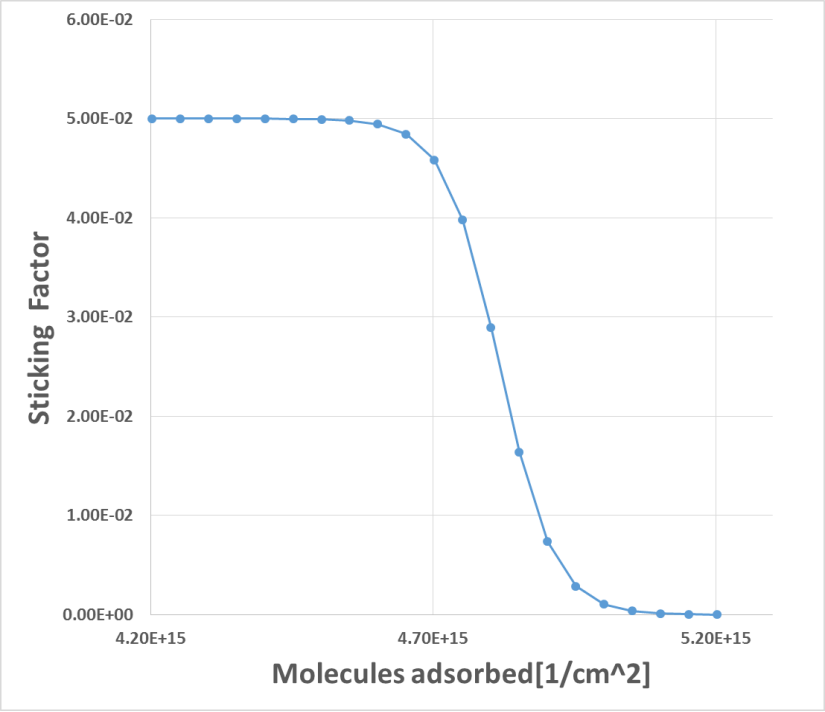

Figure 65: Sticking factor vs. adsorbed molecules per unit surface. This model was used to simulate the loss of adsorption capacity of the NEG empty site.

Using this function, simulations output reached convergence without numerical oscillations. Saturation behaves as a wave that propagates along the chamber as shown in Figure 66 and Figure 67.

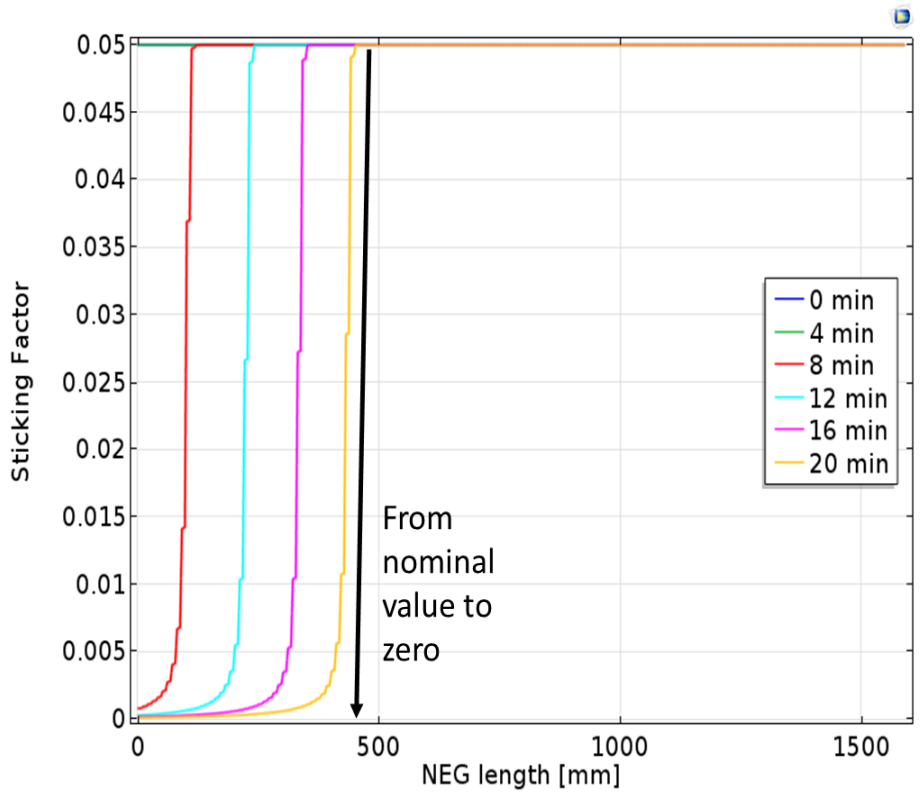

Figure 66: SF evolution during saturation waves. A 20 minutes simulation reproduce exactly the experimental conditions in terms of quantity of gas injected.

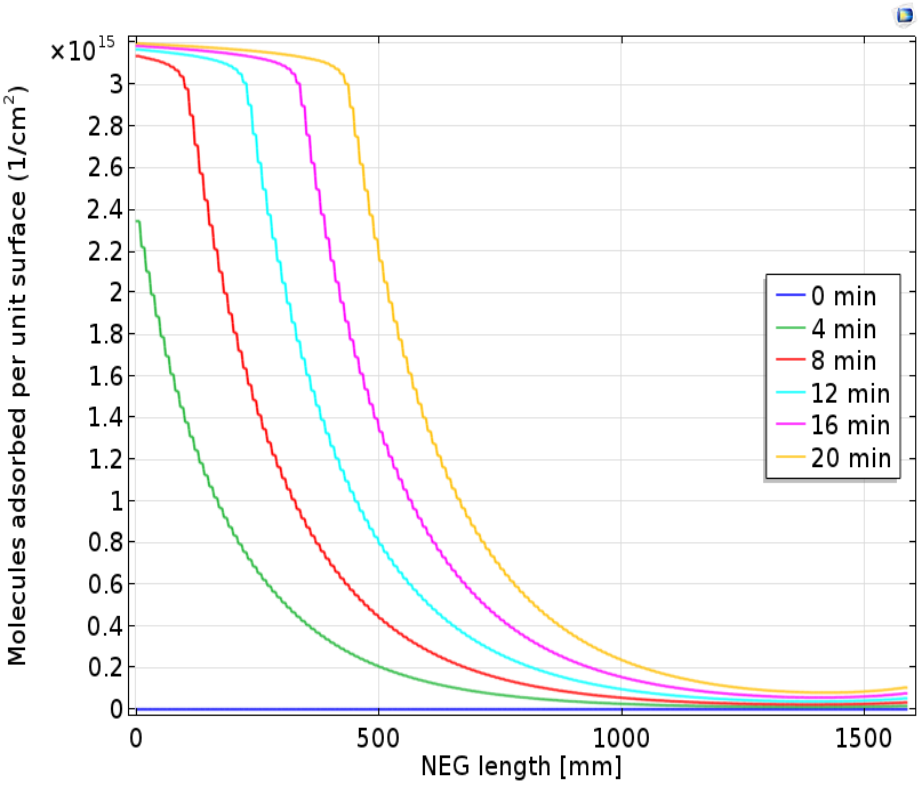

Figure 67: Quantity of adsorbed molecules/cm^2 evolution during saturation waves.

The effective reduction of the L_{NEG} to a $L_{eff\ NEG}$ leads to a modification of the TR ratio trend which now has, for the experiments conducted, the yellow shape showed in Figure 68.

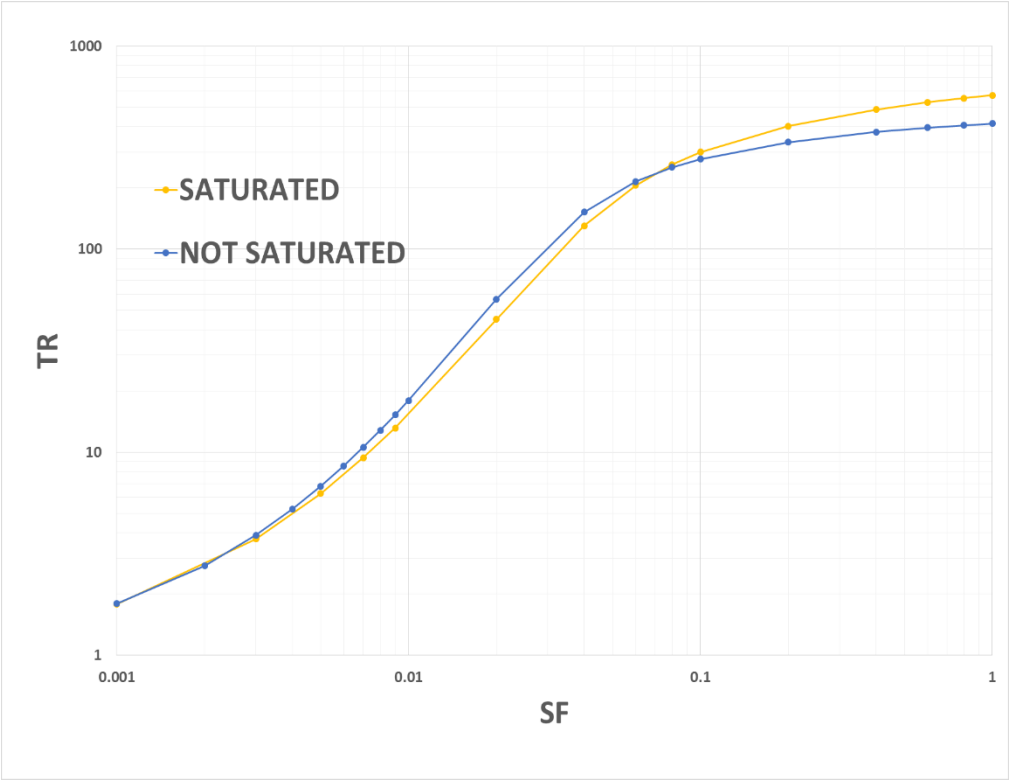

Figure 68: Transmission Ratio comparison between saturated and not saturated L/R=40 NEG chamber (both $SF_{aperture}$=0 and SF_{end}=).

Analysing Figure 68,is possible to notice how trends are crossing at a certain point. After that point, the saturated chamber has a higher TR ratio of the unsaturated one, which seems not correct: a drop of NEG performance should lead to a higher recording of hits at the end of the chamber.

What is happening is counter intuitive: due to the diffusive behaviour of the scattering we mentioned in section 5.2.2, once NEG properties fall down and all the molecules are scattered, there are indeed molecules which have a higher probability to be recorded in the backward direction than in the forward one. The latter, continuing to proceed ahead will encounter the remaining NEG active surface, with

have a certain probability to be adsorbed; the ones instead backscattered will be recorded by the SVT_2 at the entrance of the NEG chamber.

In this scenario, there is an effective increase of the TR. At a certain point, the saturation effect dominates the remaining NEG surface capacity to trap molecules. This behaviour has been simulated, and has been observed experimentally (Figure 69).

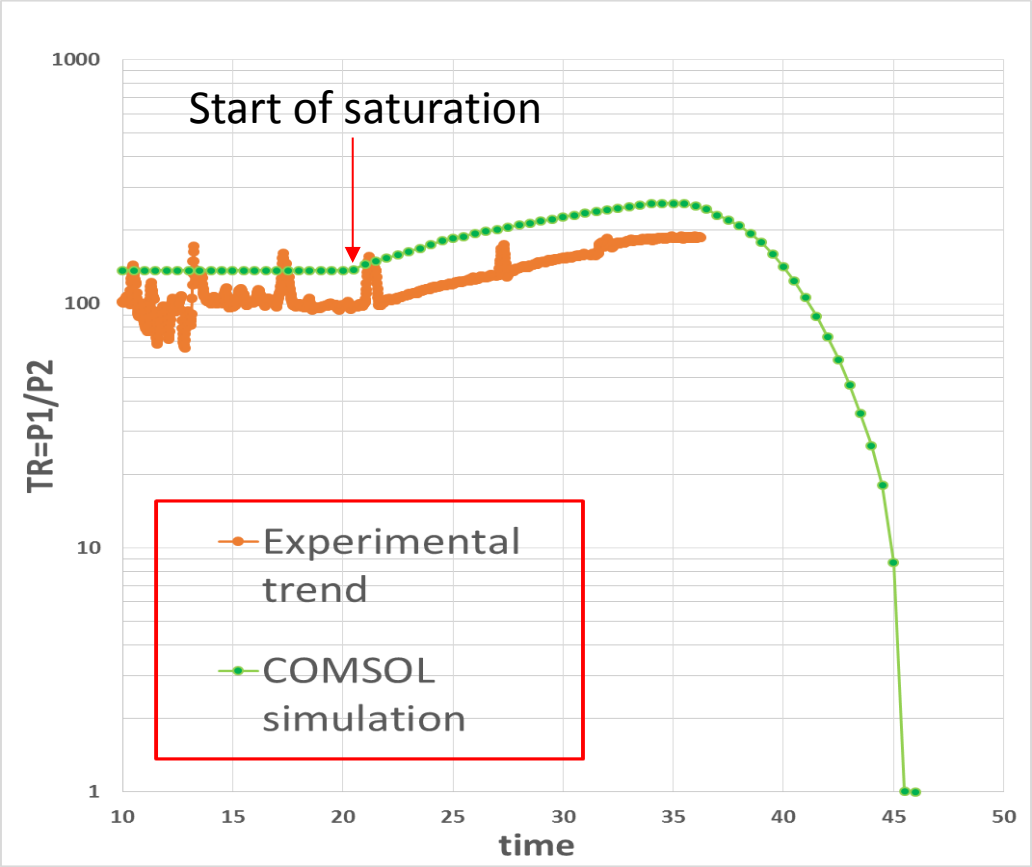

Figure 69: Evolution of the transmission ratio increasing the quantity of gas injected. Saturation begins around 20 [min] and the TR start to increase. Around 34 [min] TR starts to decrease as expected.

In this graph is possible to appreciate how both in experiment and simulation the TR increases until reaching a maximum, corresponding to a flux injected, after which is starting to decrease. The offset between both trends is the initial amount of adsorbed gas -$n_{ads}(t=0)$- used in COMSOL, which is unknown and therefore just a scale factor.

The final output of the work was to present and introduce new TR ratios trends to be used in future acceptance tests. Figure 70 shows the difference between the old chart (on top) and new one (right down):

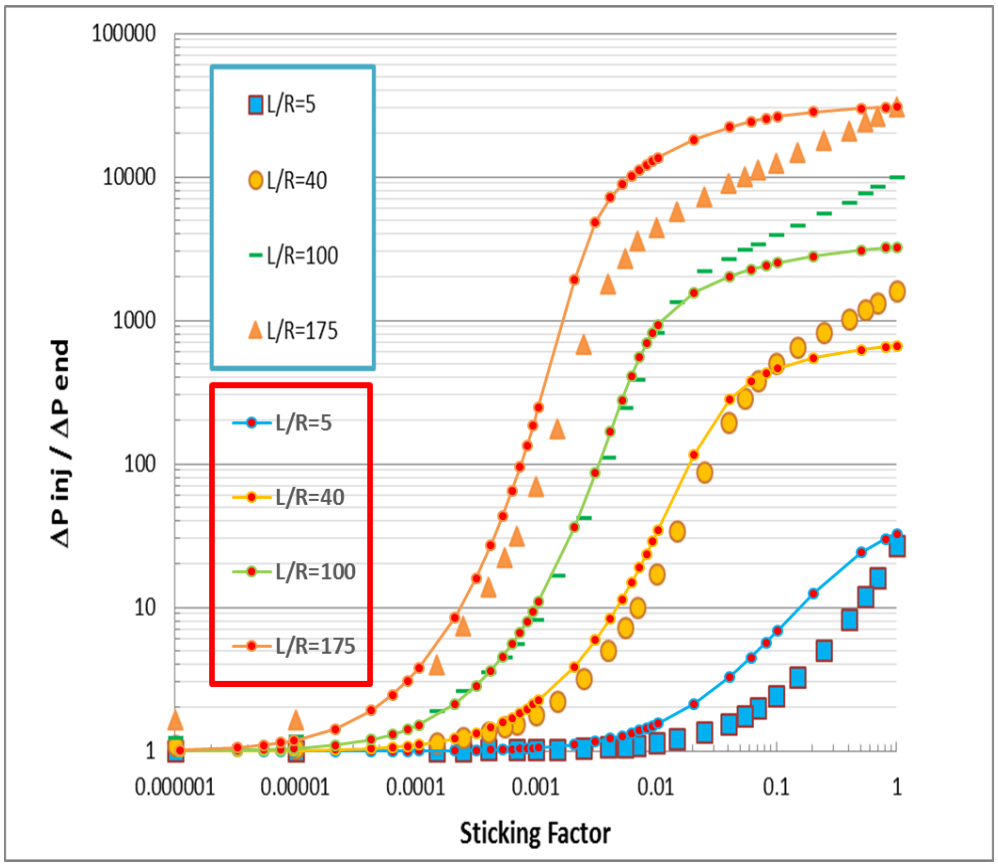

Figure 70: Comparison between new (filled lines) and old (only dots) selected trends in the TR ratio

These limits need to be addressed in order to exploit as much as possible the transmission method system.

5.3 Fast injection acceptance tests: a new tool proposal

To avoid the saturation of the NEG coating during the measurement of the transmission ratio it is necessary to reduce the quantity of gas injected – but reaching the same pressure levels of the standard performance tests.

The experience acquired with the fast injection system for H_2O and the know-how gained using the piezoelectric fast valve, brought us to implement this solution to the transmission method system for NEG coated beam pipes.

Since:

$$Q_{inj} = Q\ [\frac{mbar\ l}{s}] \cdot t[s] \qquad \text{Eq. 75}$$

One solution is to get the same pressure levels, but for a very short time, non-feasible with manual leak valves. For this reason, using the same test bench used for the first experiments, there was installed a new 2200[mm] NEG chamber and changed the injection line layout.

Figure 71 shows the layout used for this tests: it was decided to keep the manual valve and to install the new piezo valve allowing to inject with both of them.

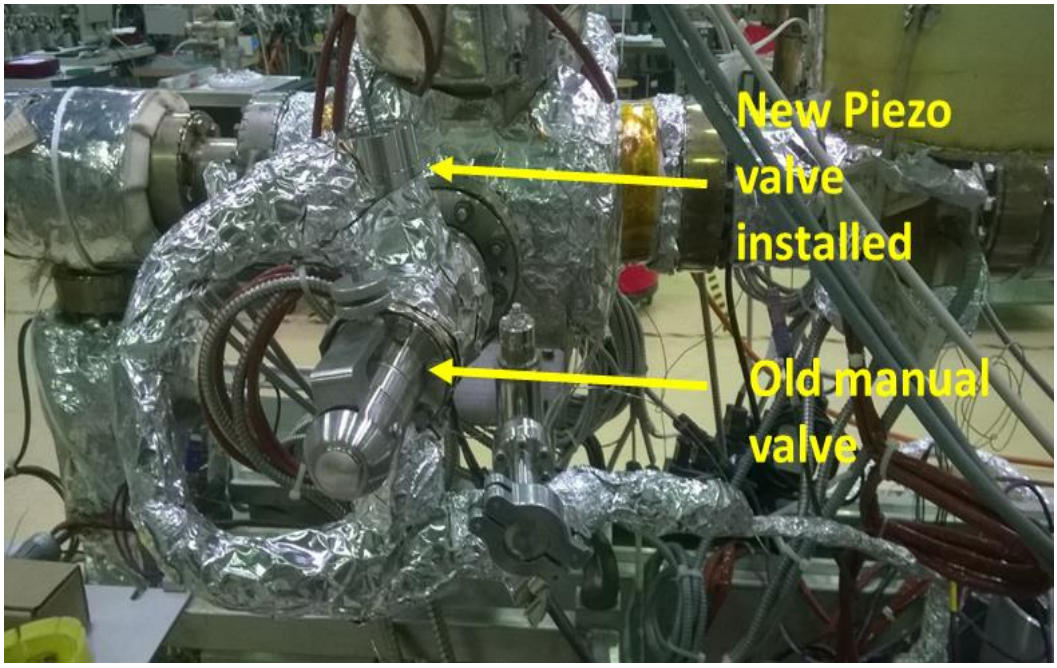

Figure 71: New injection layout mounted on the NEG test bench

To limit measurement errors both the RGAs were calibrated for each gases, allowing performing all the injections with just the RGAs filaments switched on. The transmission ratios are calculated using the partial pressure measured by the RGA. The RGA calibration consists on the injection of a gas recorded with the RGA and the Ionization gauge, before activating the NEG. In this way is possible to extract $p\ vs\ I_{ion}$ trends for the RGAs.

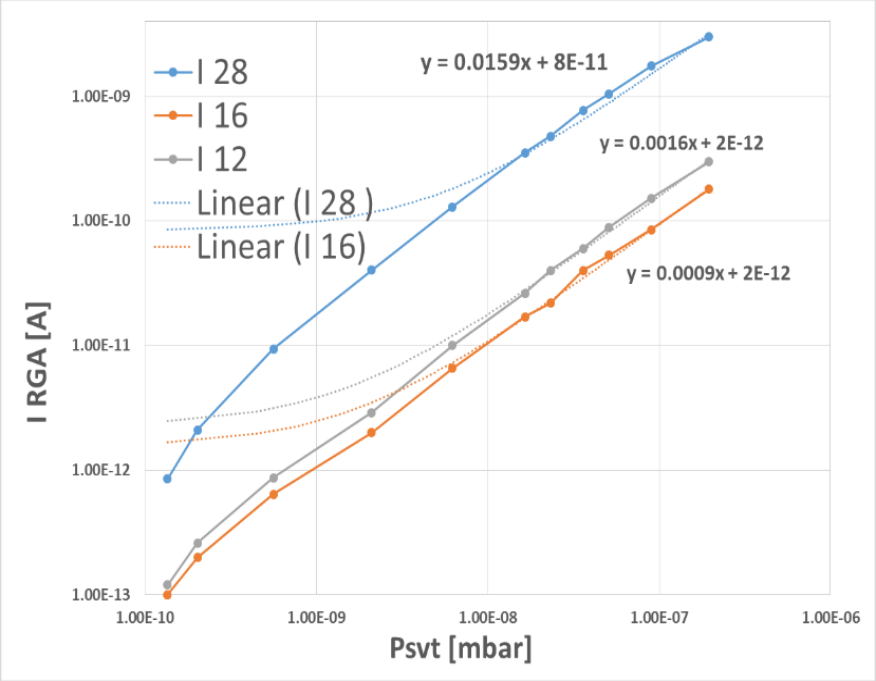

Figure 72: RGA1 calibration. The graph shows the conversion between ionisation currents and partial pressures of the gasses.

In Figure 72 is showed an example of calibration of one of the two mounted RGAs in respect of the nitrogen. For each gas was recorded the partial pressure of the dominant mass and also of his cracking pattern.

First, H_2 injections (which not saturate the NEG) were performed with the manual leak valve (Figure 73).

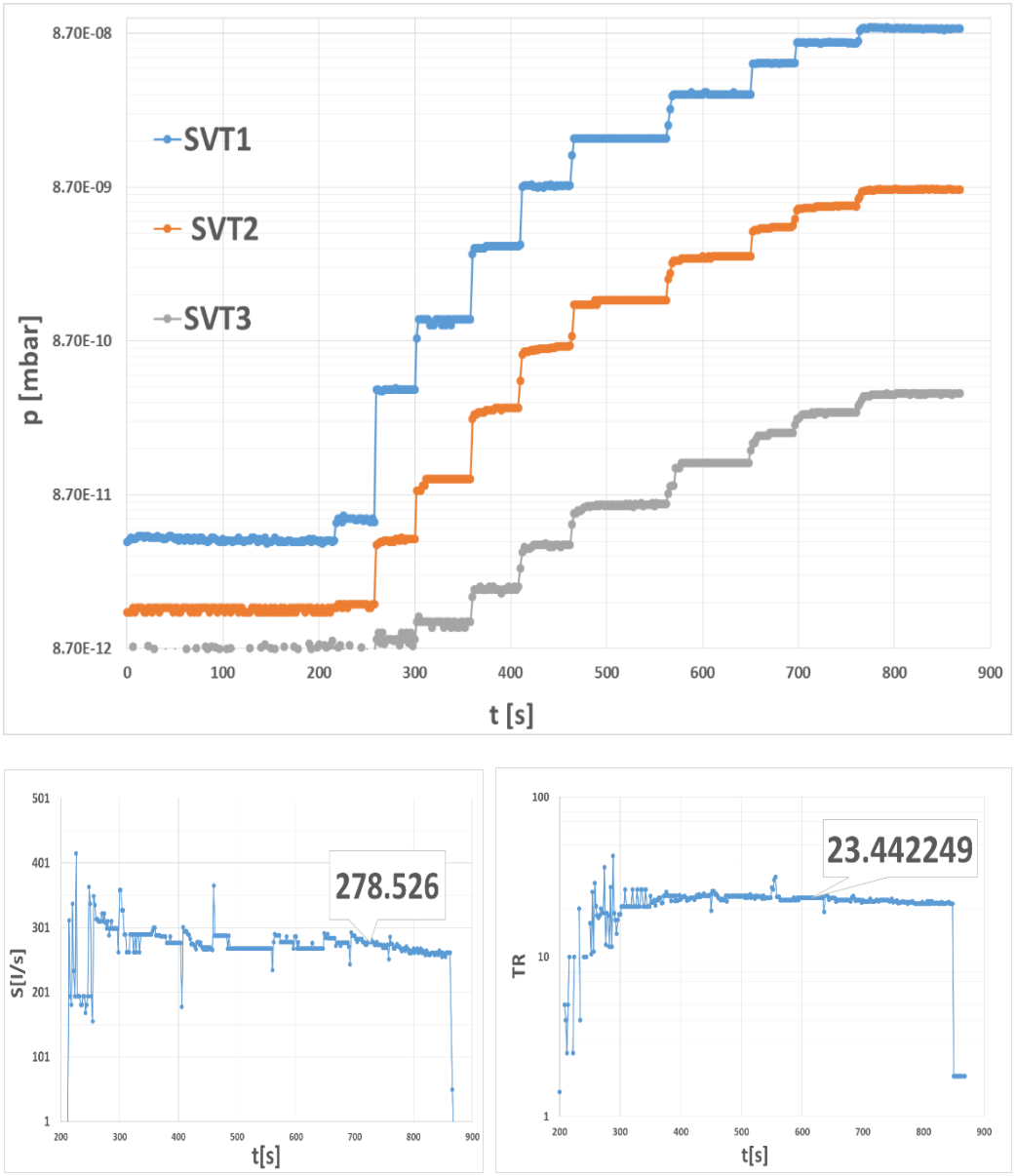

Figure 73: Hydrogen manual injection pressure steps and final outputs: on the left S[l/s] vs. t[s] and on the right the TR vs. t[s]

Then, there the same injections were repeated but in this case the fast valve was used, electronically controlled with the same controller and pulse generator seen in section 4.1 .

Different pulse lengths were tested, starting from 30 [s] going down to five seconds pulses. Figure 74 shows how, by tuning the Q was then possible to raise the injected quantity of molecules and to analyse the peak to peak data evaluating the TR and the S_{NEG}.

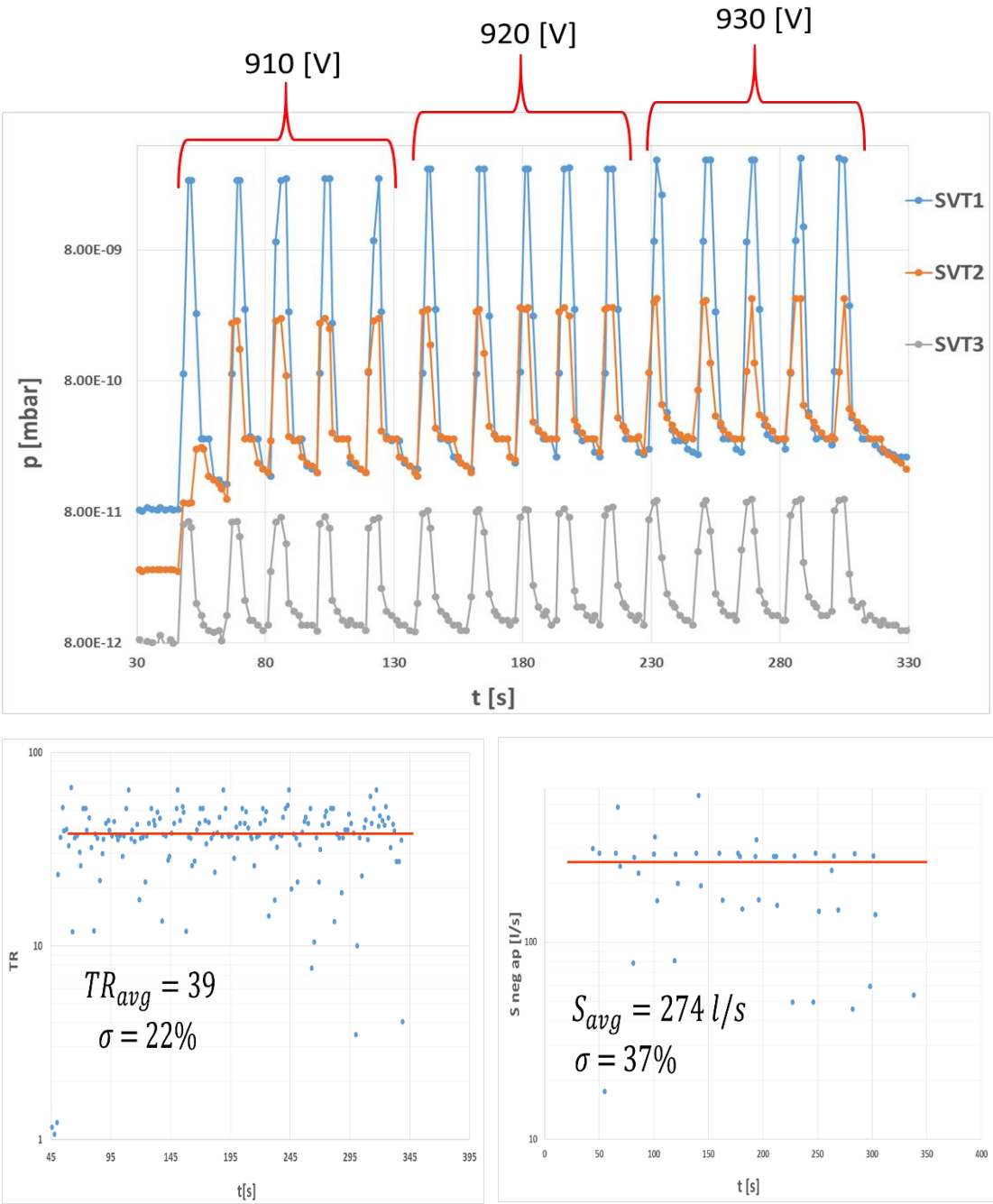

Figure 74: Hydrogen piezo fast injection steps and final outputs

It is clear from this first injection that the TR and S results are approximately the same of the manual injection ones and how is quite easy to reach nominal p_{end} in a single pressure spike for the H2 injection. The limit of the pulse injection was fixed to 5 [s] because for shorter pulse it was difficult to obtain reproducible data.

Trying to reach even smaller injection times, the subsequent idea was to record data through the same 0-10 V DAQ acquisition system used for the water injections. Figure 75 shows an example of 2-seconds CO injections.

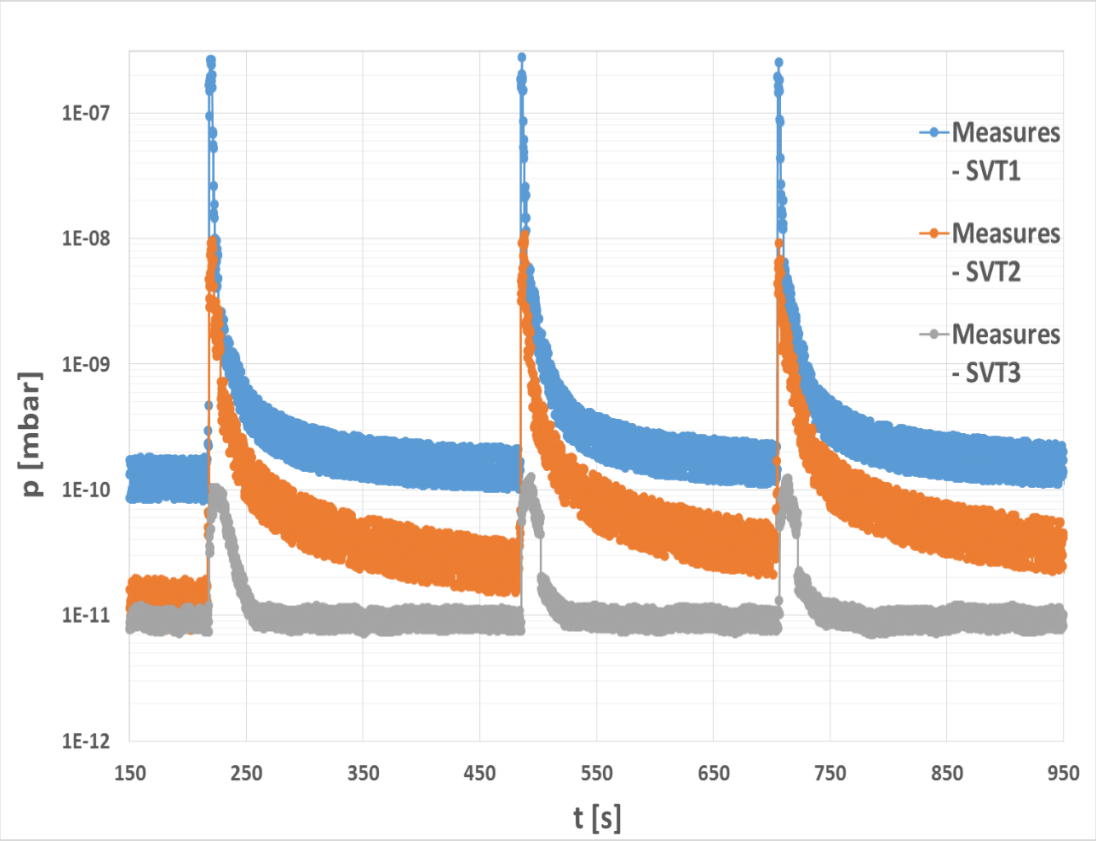

Figure 75: CO piezo-fast injection two-second pulses

As is possible to notice, the lower pressures than the water injection case stretched the acquisition limits, giving often a low signal to noise ratio and delays in the integration of the signal. Figure 76 shows a single 2 second CO injection, where is possible to appreciate these limits.

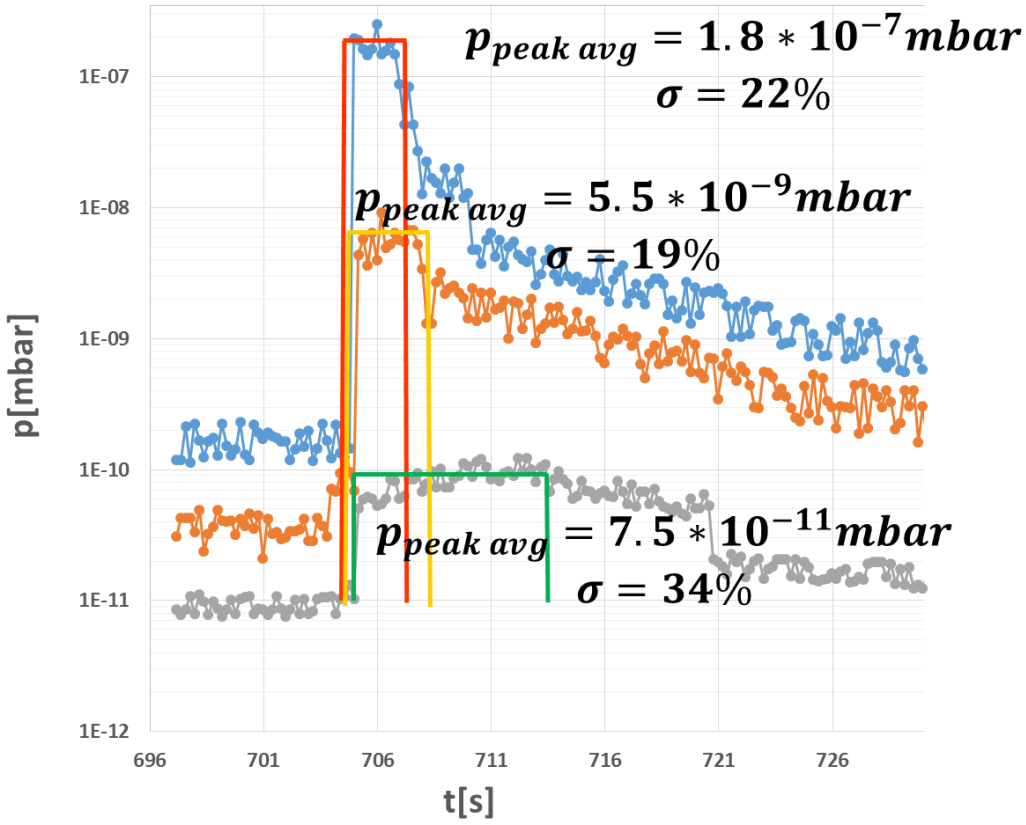

Figure 76: CO piezo-fast injection two-seconds single pulse focusing. The blue points refer to the pressure record with SVT1, the orange with SVT2 and the grey ones with SVT3.

The standard deviation values showed start to be higher going to the one second-pulses, which were indeed the final limit in terms of time of this measurements. Table 5.3 shows the pumping speed and the transmission ratio calculated through this last 0-10 [V] data acquisitions for two-seconds CO injections: the average values stands in line with the manual injection ones but still the σ remains high.

Injection t[s]	Sneg ap [l/s]	TR
705.361	3.08E+02	1.26E+01
705.561	2.24E+02	2.49E+02
705.761	2.98E+02	4.85E+02
705.961	1.51E+02	4.56E+02
706.161	2.71E+02	3.78E+02
706.361	1.87E+02	2.84E+02
706.561	1.96E+02	4.46E+02
706.761	2.03E+02	4.34E+02
706.961	1.89E+02	3.26E+02
707.161	1.74E+02	4.08E+02
Avg:	**2.20E+02**	**3.48E+02**
σ	**23%**	**38%**

Table 5.3: Pumping speed and transmission ratio output from two-seconds CO injections with 0-10[V] acquisition

Performing these injections is possible to appreciate how less portions of NEG surfaces are saturated, agreeing with the original idea of "NEG clean performances evaluation ". Under this point of view, Table **5.4** shows a clear reduction of the saturated area for CO injections, from the over 30 minutes manual (with variable Q_{pv} injected) to 3-pulses series of 2[s] or 1[s] ones, in which the saturation is practically negligible.

Gas injected mode	Quantity of gas injected [mbar l]	NEG surface saturated [cm^2]
Manual injection	2.18E-02	531.2527
7[s] injection	1.03E-04	2.507746
5[s] injection	5.06E-05	1.231961
2[s] injection	1.17E-05	0.284225
1[s] injection	8.20E-06	0.199662

Table 5.4: Comparison between quantity of gas injected and NEG saturated areas between different injection methods.

Thinking about an improvement of the signal to noise ratios should lead in principle to even lower acquisition times, which will lead to real “clean” NEG coated beam pipes performance tests.

5.4 Future possible applications

One of the advantages of the setup used for these measurements is the possibility to measure sticking factor and transmission ratio without saturation, even when the measurement is carried out at high pressure (for very short time) or using high sticking factor gases as CO.

The use of 3D modelling software like COMSOL® allows the calculation of sticking factor on NEG coated chambers with complex geometries. Optimizing the sticking factor to fit the measured pressure values.

CHAPTER 6
CONCLUSIONS

Different aspects of the molecular sticking on different surfaces used in vacuum technology has been studied throughout this thesis project.

A water injection set-up was built to carry out sticking factor measurements from the pressure evolution after fast injections. The behaviour of an untreated 316L stainless steel in respect of the water adsorption has been evaluated for the subsequent experiments: constant temperature injections up to saturation (at 25°C, 40°C, 50°C, 60°C, 70°C, 100°C), then pump-down and bake-outs at 150°C. Water adsorption isotherms have been therefore carried out, showing a similar behaviour for each temperature. From this curves, sticking factor values have been extrapolated.

The behaviour of the saturation of NEG coated pipes during acceptance tests has been measured and confirmed by simulations, identifying the limits of the test procedures and proposing new possible improvements. Therefore, a new fast-injection gas system has been developed, providing the same results levels for CO injections achieved with traditional injections but with less than three order of magnitude of gas injected hence not saturating the chamber. The comparable outputs in terms of transmission ratio and pumping speed allow thinking also to in situ applications, where the performance of NEG vacuum chambers could be checked directly with a portable fast-injection system.

Table of Contents

List of Figures

List of Tables

BIBLIOGRAPHY

[1] Stanford, S. L., & Berkeley, L. B. (1976). *PEP conceptual design report.* Berkeley, CA : Lawrence Berkeley Nat. Lab.

[2] Benvenuti, C. (1983). *Nucl. Instrum. Methods*, 205-391.

[3] Garion, C. (March 2014). *On bake-out related design costs for LHC accelerator.* Geneve.

[4] Lafferty, J. M. (1998). *Foundations of Vacuum Science and Technology.*

[5] P.Chiggiato. (2010). *Vacuum Technology for particle accelerators.* Geneve.

[6] Harris, N. (2011, February 02). *Vacuum pump*. Retrieved from www.thermopedia.com.

[7] emandpplabs.nscee.edu. (n.d.). *Turbo Pumps*. Retrieved from emandpplabs.nscee.edu.

[8] A.Morris. (2003). *Gas Sources and Attainable Pressure in Vacuum Systems*. Retrieved from www.globalspec.com.

[9] J.K. Gorman, W.R. Nardella (1962). *Hydrogen permeation through metals.* Vacuum, Volume 12, Issue 1,

[10] Marquardt, N. (n.d.). Introduction to the principles of vacuum physics. Dortmund, Germany.

[11] H.F.Dylla. (2006). The Problem of Water in Vacuum Systems.

[12] O'Hanlon, J. F. (1989). *A User's Guide to Vacuum Technology.* John Wiley & Sons.

[13] Danielson, P. (2000). Sources of water vapor in vacuum systems. *The Vacuum Lab*.

[14] Jousten, K. (n.d.). Thermal Outgassing. Berlin.

[15] H.F. Dylla, D. M. (1993). Correlation of outgassing of stainless steel and aluminium withy various surfaces treatments. *JVSTA*.

[16] Wutz, A. W. (1989). *Theory and Practice of Vacuum Technology.* Vieweg.

[17] P.A.Redhead. (1995). Modeling the pumpdown reversibly adsorbed phase. i. monolayer and submonolayer initial coverage. *JVSTA*.

[18] K.Kanazawa. (1989). Analysis of pumping down process. *JVSTB*.

[19] Stolley, D. (2014). Retrieved from daniellestolleyopennotebook.wordpress.com.

[20] R.Kersevan, J. (2009). Introduction to MOLFLOW+: new graphical processing unit-based monte carlo code for simulating molecular flows and for calculating angular coefficients in the compute unified device architecture environment. *JVST*, 1017-1023.

[21] Herman, M. A., Richter, W., & Sitter, H. (2004). *Epitaxy: Physical Principles and Technical Implementation.* Springer.

[22] Horikoshi, G. (1987). Physical understanding of gas desorption mechanisms. *Journal of Vacuum Science & Technology A*.

[23] Foo, K., & Hameed, B. (2010). Insights into the modeling of adsorption isotherm systems. *Chemical Engineering Journal*.

[24] Minassian-Saraga, L. T. (January 1994). Thin films including layers: terminology in relation to their preparation and characterization. *Pure and Applied Chemistry*, 66(8).

[25] Langmuir, I. (September 1918). THE ADSORPTION OF GASES ON PLANE SURFACES OF GLASS,MICA AND PLATINUM. *J.Am.Chem. Soc*, 1361-1403.

[26] Temkin, M. I., & Pyzhev, V. (1940). The Arrhenius equation and the active complex method. *Acta Physicochimica*, 13 733.

[27] Sips, R. (January 1948). On the structure of a catalyst surface. *The Journal of Chemical Physics*, 16(5):490-495.

[28] Sips, R. (March 1950). On the structure of a catalyst surface II. *The Journal of Chemical Physics*, 18(8): 105-114.

[29] P.Chiggiato, P. P. (2006). Ti–Zr–V non-evaporable getter films: From development to large scale production for the Large Hadron Collider. *Thin Solid Films*

[30] VB Vykhodets, SM Klostman, TY Kurennyk, AD Levin, VA Pavlov (1989) Phys. Met. Metallography

[31] C. Benvenuti, J. C. (1999). *Vacuum*, 53-219.

[32] C.Benvenuti. (1997). *Non-evaporable getters: from pumping strips to thin film coatings.* Geneva, CERN.

[33] C. Benvenuti, N. C. (1984). *Applied Physics Letters*.

[34] C. Benvenuti, S. C.-M. (2001). *Physica C*, 351-421.

[35] McGraw-Hill, E. (2003). *McGraw-Hill Dictionary of Scientific & Technical Terms.* The McGraw-Hill Companies, Inc.

[36] E.Fischer, H.Mommsen(1966). *Monte Carlo computations on molecular flow in pumping speed test domes.* ISR-VAC/66-11

[37] Bregliozzi, G. (2011). *Vaccum acceptance test of the NEG Beam Pipes.* Geneve

[38] C.Benvenuti et al. (2003). *Vacuum*

[39] M.Jimenez, B.Versolatto (2004). Outgassing measurements made on the prototype of BN module for the injection collimator (TDI).Vacuum Technical note, Geneve